::: 11. 1, 4 .;:: . . . . . ::::: 100 ·. Ξ, 

:: ::

14.

.,.

#

#### ABSTRACT

# HIGH-FIELD MAGNETORESISTANCE OF AuGa, AuPb<sub>2</sub> AND Au<sub>2</sub>Pb

By.

### Robert Bass

High-field magnetoresistance (HFMR) measurements have been made on three intermetallic compounds, AuGa, AuPb<sub>2</sub>, and Au<sub>2</sub>Pb, which belong to structural types not previously investigated by HFMR techniques. The connectivity of the Fermi surface (FS) of AuPb<sub>2</sub> and AuGa has been determined while the FS topology of Au<sub>2</sub>Pb is still unresolved.

All three compounds studied are compensated compounds in accordance with their even number of electrons per unit cell as calculated by assuming that Au contributes 1 electron/atom, Ga 3 electrons/atom, and Pb 4 electrons/atom to the conduction band. All three compounds have a FS which supports Open orbits.

The topology of the AuPb<sub>2</sub> FS can be explained by open orbit producing cylinders running in the <110> and <101> directions in k-space. This model of the open FS is consistent with the experimentally determined open orbit directions, <100>, <110>, <101>, <112> and <211>. Higher order open orbits are also observed. The [001] could not be

. . . ا سو : -• ... :: ÷ : .

Robert Bass

investigated for open orbits due to experimental limitations.

The topology of the open AuGa FS consists of a cylinder running in the [001]. Experimentally open orbits are observed in the [001] but not in the [100]. The [010] direction could not be investigated for open orbits.

The topology of the Au<sub>2</sub>Pb FS deviates from that expected of a cubic system since the open orbit directions do not seem to lie along symmetry directions. More experimental results are needed before the FS topology can be derived.

The FS topology of AuGa cannot be explained by the nearly-free-electron (NFE) model constructed by the Harrison method. The NFE model for AuPb<sub>2</sub> constructed for a few magnetic field directions gives results which are in agreement with the experimentally determined open orbit directions.

The relatively high degree of crystalline perfection attained in the samples grown, as indicated by residual resistance ratios ranging from  $\approx$  300 to  $\approx$  600, should spur other experimenters to investigate the FS of Au<sub>2</sub>Pb and AuPb<sub>2</sub> by means of the de Haas van Alphen effect.

# HIGH-FIELD MAGNETORESISTANCE OF AuGa, AuPb<sub>2</sub> AND Au<sub>2</sub>Pb

Ву

Robert Bass

## A THESIS

Submitted to
Michigan State University
in partial fulfillment of the requirements
for the degree of

DOCTOR OF PHILOSOPHY

Department of Physics

1972

		-
		3:
		<u>:</u>
		<u>:</u>
		:
_		



#### ACKNOWLEDGMENTS

I would like to thank Professor P. A. Schroeder for his advice, encouragement, and good nature during the course of this research. His constructive criticism of the first draft of this thesis is sincerely appreciated. I wish to thank Mr. Nick Rutter for skillfully machining the sample holder and Mr. Boyd Shumaker for his assistance in growing the AuPb, samples. I am indebted to Dr. Gordon J. Edwards for the fine job he did in constructing the auxiliary equipment and housing needed to operate the superconducting mag-I also appreciate the guidance and knowledge he unselfishly gave during his stay in the laboratory. Last, but certainly not least, I would like to acknowledge the support and friendship of all the fine people who made my stay here a rewarding experience, the men of the machine and electric shops, the secretaries, the professors in the solid state group and my fellow graduate students, especially Mr. Joseph Pernicone who was able to evoke a smile from me even when this research was going slowly and there was little joy in my heart.

The financial support of the National Science Foundation is gratefully acknowledged.

# TABLE OF CONTENTS

		Page
I.	INTRODUCTION	1
II.	CRYSTAL GROWTH	13
III.	THEORY OF HFMR Orbits Formal Transport Theory Compensation of Intermetallic Compounds The High Field Conductivity Tensor Open Orbits Physical Explanation of HFMR	21 24 26 32 33 35 39
IV.	SAMPLE PREPARATION Crystal Growth AuGa NiGe and Others Au <sub>2</sub> Pb and Au <sub>2</sub> Pb <sub>2</sub> RRR Measurements X-Ray Procedure	42 42 45 48 52 53
v.	EXPERIMENTAL PROCEDURE Cryostat and Sample Holder Voltage Measurements Analyses of Tipping Arrangement	59 59 62 67
VI.	RESULTS AuGa AuPb <sub>2</sub> Au <sub>2</sub> P5	74 74 91 114
CON	NCLUSIONS	139
LIS	ST OF REFERENCES	142
API	PENDIX A The Relaxation Approximation	146
API	PENDIX B The Superconducting Magnet	148

			-
			12
			:
			•• •

# LIST OF TABLES

Table		Page	
ı.	Metallic Intermetallic Compounds Previously Investigated	2	
II.	Nearly Free Electron Model Applied to Intermetallic Compounds	5	
III.	Band Structure Calculations	6	
IV.	Some CsCl Type Intermetallic Compounds	8	
v.	Some CaF <sub>2</sub> Type Intermetallic Compounds	8	
VI.	Some CuAl <sub>2</sub> Type Intermetallic Compounds	11	
VII.	Some MnP Type Intermetallic Compounds	11	
VIII.	Summary of High-Field Galvanomagnetic Properties of Metals	38	
IX.	RRR and Orientation of Samples	55	
х.	AuGa Lattice Constants	77	
XI.	FS Parameters for AuGa		
XII.	Open Orbit Directions in AuPb	105	

# LIST OF FIGURES

Figure		Page
1.	Phase diagram of Mg-Ag (From Hansen, Ref. 31)	14
2.	Phase diagram showing a compound having a maximum melting temperature at a non-stoichiometric concentration	16
3.	Phase diagram with excellent characteristics	18
4.	Various types of closed and open orbits (From Fawcett, Ref. 41)	25
5.	Model of open FS	27
6.	Phase diagram of Au-Ga (From Hansen, Ref. 31)	43
7.	Phase diagram of Au-Pb (From Hansen, Ref. 31)	49
8.	V(B) vs. B for (a) AuPb <sub>2</sub> and (b) Au <sub>2</sub> Pb samples	54
9.	Sample Holder	60
10.	V(B) vs. B for Au <sub>2</sub> PbI	65
11.	<ul><li>(a) Rotation and tipping geometry and</li><li>(b) stereographic projection of motion of B</li></ul>	68
12.	Non-transverse geometry	70
13.	Comparison of NiAs and AuGa structures. The lower diagrams are projections taken along the c axis in NiAs while the upper diagrams are taken along the a axis. The height of the atoms above the projection plane is given by the numbers beside the atoms. Dark spheres represent Ni(Au) atoms while light spheres represent As(Ga) atoms.	76
14.	V(B) vs. ψ for AuGaI	78
15.	V(B) vs. B for AuGaI	79
16.	Δρ/ρ vs. ψ for AuGaI	80
17.	Stereographic projection of AuGaI	82

Figure		Page
18.	Stereographic projection of AuGaII. X's designate position of sharp peaks.	82
19.	Δρ/ρ <sub>o</sub> vs. ψ for AuGaII	83
20.	$\textbf{V(B)}$ vs. $\psi$ for different values of $\phi$ for AuGaII	84
21.	Conventional cell of AuPb <sub>2</sub>	92
22.	$V(B)$ vs. $\psi$ for various values of B for $AuPb_2^I$	93
23.	Δρ/ρ <sub>o</sub> vs. ψ for AuPb <sub>2</sub> I	94
24.	Δρ/ρ <sub>o</sub> vs. ψ for AuPb <sub>2</sub> II	95
25.	Δρ/ρ <sub>o</sub> vs. ψ for AuPb <sub>2</sub> IV	96
26.	Δρ/ρ vs. ψ for AuPb <sub>2</sub> V	97
27.	Δρ/ρ <sub>O</sub> vs. ψ for AuPb <sub>2</sub> VI	98
28.	$V(B)$ vs. $\psi$ for various values of $\phi$ for $AuPb_2I$	100
29.	Stereographic projection showing minima for AuPb <sub>2</sub> I	101
30.	Stereographic projection of HFMR results for (a) AuPb <sub>2</sub> II and (b) AuPb <sub>2</sub> IV	102
31.	Stereographic projection of HFMR results for (a) AuPb <sub>2</sub> V and (b) AuPb <sub>2</sub> VI	103
32.	Stereogram showing (a) open orbit directions (b) current directions, J, of samples and (c) planes corresponding to open orbit	
	directions	107
33.	Real and reciprocal lattice cells of AuPb <sub>2</sub>	109
34.	Brillouin zone of AuPb <sub>2</sub> . Vectors correspond to directions in k-space	110
35.	<110> cylinders generating <100> open orbits	112
36.	Conventional cell of Au <sub>2</sub> Pb	115
37.	$V(B)$ vs. $\psi$ for various values of B for Au <sub>2</sub> PbI	116

Egur

35.

33.

41.

£.

43

44

,

.

Figure		Page
38.	$V(B)$ vs. $\psi$ for various values of B for AuPbII	116
39.	Δρ/ρ <sub>o</sub> vs. ψ for Au <sub>2</sub> PbI	117
40.	Δρ/ρ <sub>o</sub> vs. ψ for Au <sub>2</sub> PbIIb	118
41.	$\Delta \rho / \rho_0$ vs. $\psi$ for (a) $Au_2$ PbIII and (b) $Au_2$ PbV	119
42.	Δρ/ρ <sub>o</sub> vs. ψ for Au <sub>2</sub> PbVI	120
43.	Δρ/ρ <sub>o</sub> vs. ψ for Au <sub>2</sub> PbVII	120
44.	V(B) vs. $\psi$ for tip angles $\phi^{\leq} 16.5^{\circ} $	122
45.	V(B) vs. $\psi$ for tip angles $\phi^{\leq} 33^{\circ} $	123
46.	V(B) vs. $\psi$ for tip angles $\phi^{\leq} 66^{\circ} $	124
47.	V(B) vs. $\psi$ for various values of $\phi$ for (a) Au <sub>2</sub> PbIII and (b) Au <sub>2</sub> PbIb	125
48.	Stereographic projections of HFMR results for (a) Au <sub>2</sub> PbIb and (b) Au <sub>2</sub> PbIIb	126
49.	Stereographic projections of HFMR results for (a) Au <sub>2</sub> PbVI and (b) Au <sub>2</sub> PbVII	127
50.	V(B) vs. $\psi$ for Au <sub>2</sub> PbIIb for (a) $\phi$ = 0°, 11° and (b) $\phi$ = 22°, 37.5°	131
51.	Open orbit directions for four different cubic FS topologies (From Lifshitz and Perschanski, Ref. 40)	133

#### INTRODUCTION

The study of the Fermi surface (FS) of metallic intermetallic compounds began in 1961 with a paper by Thoren and Berlincourt on the de Haas-van Alphen effect (dHvA) in InBi. (1) Since that time many compounds of various crystal structure have been investigated and Table I gives a listing of many of these compounds. The dHvA effect and high field magnetoresistance (HFMR) are the most widely used experiments for studying the FS. The dHvA effect measures extremal areas of FS enclosed by the conduction electrons as they undergo periodic closed trajectories on the FS. If the electrons do not make closed orbits, that is, the electron does not return to its initial position on the FS, then the FS supports open orbits which can be investigated by HFMR. Thus the topology of the FS is determined by HFMR.

The growth and preparation of samples to be used in dHvA and HFMR experiments is of crucial importance. First, single crystals must be grown and second, the crystals must be of sufficient perfection, as determined by the residual resistance ratio (RRR). The necessity of using single crystal specimens is obvious since the dHvA and HFMR effects measure the anisotropy of the FS and depend on the specific direction of the magnetic field with respect to the crystallographic axes. A polycrystalline sample would produce an averaging effect

Table I. Metallic Intermetallic Compounds Previously Investigated

Compound	Crystal Structure	Crystal System	Reference
β <b>'CuZn</b>	B2 (CsCl)	Cubic	2,3
β'AuZn			2
β'AgZn			4
β'PdIn			4
AuAl <sub>2</sub>	Cl (CaF <sub>2</sub> )	Cubic	5,6
AuGa <sub>2</sub>			5,6
AuIn <sub>2</sub>			5,6
AuSb <sub>2</sub>	C2 (FeS <sub>2</sub> , pyrites)	Cubic	7
SiP <sub>2</sub>			8
MgCu <sub>2</sub>	C15	Cubic	9
InBi	B10 (PbO)	Tetragonal	1
MgZn <sub>2</sub>	C14	Hexagonal	10
PtSn	B8 (NiAs)	Hexagonal	11
AuSn			12,13
PbSb			14
PdTe			14
AuGa	B31 (MnP)	Orthorhombic	15

which could easily obscure the anisotropy. The RRR, which is the ratio of the room temperature resistance divided by the resistance at 4.2°K, is a measure of the scattering of the conduction electrons by non-thermal processes at 4.2°K. If the electrons are scattered before they make one complete orbit on the FS then little information is obtained about the FS. A high value of the RRR ensures that the electrons make many orbits if the FS is closed or pass through many cells if the FS is open before colliding with scattering centers.

Samples with a RRR of only 25 can be used for dHvA measurements (2) while a value of about 100 is generally needed for HFMR experiments if a field of 100 kilogauss (kG) is available. The need for more perfect specimens in HFMR experiments is due to the requirement that all the conduction electrons must be in the high field region, i.e., all the conduction electrons must complete many orbits before being scattered while dHvA measurements can be made on small pieces of FS which contain a small fraction of the total number of conduction electrons.

The Nearly Free Electron model (NFE) is the first reasonable approximation used in interpreting the results of FS measurements. The success of the Pseudopotential Theory of W. A. Harrison (16), and others in explaining the experimental results of FS studies of the simple metals supports the use of the NFE model for such metals. The NFE model has also

been used to interpret the results for intermetallic compounds; such attempts have given mixed results. Table II gives a summary of the success or failure of the NFE model applied to all intermetallic compounds studied by both dHvA and HFMR.

From the theoretical standpoint, the most authoritative results obtained on the FS come from band structure calcula-Such calculations have been done for most metallic, semi-metallic, and semiconducting elements. There have also been many calculations on semiconducting intermetallic compounds and a few calculations on metallic intermetallic compounds. Table III gives a partial list of the metallic compounds which have been done to date. The theorists are now able to attack crystal structures with as many as 8 atoms per primitive cell by first-principles methods such as the APW calculation done for the  $\beta$ -wolfram structure compound  $V_3\text{Ga}^{(24)}$ . Pseudopotential calculations, using derived values, have been done on structures with as many as 12 atoms per unit cell (MgZn<sub>2</sub>) (24). Thus, the more complicated crystal structures which contain many atoms per unit cell are now theoretically tractable and the experimentalists should provide the data necessary to check the theoretical results.

Intermetallic compounds composed of the well understood metals, semimetals, and semiconductors, have been the first to be investigated. The elements which form this group are Al, Mg, Zn, Ga, Cd, In, Sn, Hg, Tl, Pb, Cu, Ag, Au, Ge, Si, Sb, Bi, Mn, Fe, Co, Ni, Pd, and Pt. The most common structures

Table II. Nearly Free Electron Model Applied to Intermetallic Compounds

Crystal Structure	Successful*	
Cl (CaF <sub>2</sub> )	Yes	
Cl (CaF <sub>2</sub> )	Yes	
B8 (NiAs)	Yes	
B2 (CsCl)	Yes	
C2 (FeS <sub>2</sub> )	No	
-	C1 (CaF <sub>2</sub> ) C1 (CaF <sub>2</sub> ) B8 (NiAs) B2 (CsC1)	C1 (CaF <sub>2</sub> ) Yes C1 (CaF <sub>2</sub> ) Yes B8 (NiAs) Yes B2 (CsC1) Yes

<sup>\*</sup>As a first qualitative explanation

:i:

Table III. Band Structure Calculations

Compound	Type of Calculation*	Reference
β'CuZn	K-R, APW, NLPP	17,18,19
β'AgZn	K-R	17
β'PdIn	LNPP, APW	19,20
β'NiAl	APW	21
β 'AuZn	KKR	21
AuAl <sub>2</sub>	APW	22
AuGa <sub>2</sub>	APW	22
AuIn <sub>2</sub>	APW	22
AuSn	APW	23
MgZn <sub>2</sub>	LPP	24
V <sub>3</sub> X(X=Si, Co,	APW	25
Ga, Ge, As)		

# \*Abbreviations

APW - Augmented Plane Wave

KKR - Korringa-Kohn-Rostoker

K-R - Kohn-Rostoker
LPP - Local Pseudopotential
NLPP- Non-Local Pseudopotential

formed by these metals will be discussed next.

The B2(CsCl) structure is a very simple structure containing 2 atoms per unit cell. The space group is cubic  $O_h^1$  - Pm3m. Table IV is a list of some B2 compounds. Compounds with this structure are attractive for theoretical study due to the small number of atoms per unit cell. As noted in Table III,  $\beta$ 'CuZn,  $\beta$ 'NiAl,  $\beta$ 'PdIn, and  $\beta$ 'AgZn have been investigated by theoretical methods while only  $\beta$ 'CuZn has been completely investigated experimentally. The HFMR work on CsCl structure compounds has not been done, with the exception of  $\beta$ 'CuZn, since crystals with sufficiently high values of RRR are very difficult to grow. The reason for this difficulty will be discussed in the next chapter.

The B3 (ZnS, zincblende) structure is also cubic with space group  $T_d^2$  - F43m and with 2 atoms per unit cell. Intermetallic compounds like XSb, (X = In, Ga, Al), which have this structure are semiconductors and have been studied quite thoroughly both experimentally and theoretically. The FS of semiconducting compounds consists of small closed regions and HFMR would not give any new information about the FS.

Intermetallic compounds which form the  $Cl(CaF_2)$  structure have been rather extensively studied as can be seen in Tables II and III. The Cl structure is cubic with full cubic symmetry  $O_h^5$  - Fm3m and 3 atoms per unit cell. Table V is a list of some compounds which have the  $CaF_2$  structure. The compounds AuIn<sub>2</sub> and Mg<sub>2</sub>Pb have been studied by dHvA but not HFMR

=

-

:

Table IV. Some CsCl Type Intermetallic Compounds\*

			<del></del>
LiAg	AgCd	NiAl	DyRh
LiHg	AuMg	TlBi	DyAu
CuPd	AuZn	PdIn	HoCu
CuZn	AuCd	NiGa	GdZn
MgAg	MgHg	AgCe	YZn
AgZn	MgT1	ErIn	GdMg
MgAg	МдНд	AgCe	YZn

<sup>\*</sup>A. E. Dwight (26) reports that there are 169 intermetallic compounds with the CsCl structure, making this structure the second largest family of compounds.

Table V. Some CaF<sub>2</sub> Type Intermetallic Compounds

AuG	<sup>a</sup> 2	Mg <sub>2</sub> Si*
AuA	12	Mg <sub>2</sub> Ge*
AuI	n <sub>2</sub>	Mg <sub>2</sub> Sn*
PtA	12	Mg <sub>2</sub> Pb <sup>+</sup>
PtS	n <sub>2</sub>	PtIn <sub>2</sub>
ScC	u <sub>2</sub>	Ir <sub>2</sub> P

<sup>\*</sup>semiconducting compound

<sup>†</sup>semimetallic compound

due to low values of RRR. PtAl<sub>2</sub> seems to be a good candidate for study as its phase diagram indicates that the compound should be growable.

The remaining structures all have at least 4 atoms per unit cell. Of these, the B8(NiAs) structure with space group D<sub>6</sub><sup>4</sup>h - P6<sub>3</sub>/mmc frequently occurs and is generally formed by the transition metals Cr, Mn, Fe, Co, and Ni alloyed with the metalloids S, Se, Te, As, Sb, Bi and sometimes also Ge and Sn. One notable exception is AuSn. Pearson's (27) article on NiAs compounds and related structures is an excellent reference for these interesting compounds. Four compounds have given dHvA oscillations: PbSb, PdTe, PtSn, and AuSn. (14) PtSn and AuSn have been rather thoroughly studied by dHvA while there is little information on the FS of PbSb and PdTe. Only AuSn has been studied by HFMR. Other compounds which seem promising for further study are NiSb, BiPt, PdSb, and PtSn.

Compounds forming superlattices have been the source of much experimental and theoretical work. The  $Ll_2(Cu_3Au)$  structure with cubic space group  $O_h^1$  - Pm3m and  $L_O^1(CuAu)$ , tetragonal with space group  $D_{4h}^1$  - P4/mmm both have 4 atoms per unit cell. The FS of these structures has not been adequately experimentally investigated due to the lack of useable crystals, i.e., the RRR has not been higher than about 10.

The Laves phases constitute the largest group of binary

compounds. There are three prototype structures based on magnesium: MgCu<sub>2</sub> (Cl5), which is cubic and has space group O<sub>h</sub><sup>7</sup> - Fd3m, MgZn<sub>2</sub>(Cl4) which is hexagonal and belongs to space group D<sub>6h</sub><sup>4</sup> - P6<sub>3</sub>/mmc and MgNi<sub>2</sub> (C36) which is hexagonal and has space group D<sub>6h</sub><sup>4</sup> - P6<sub>3</sub>/mmc. Only the MgCu<sub>2</sub> structure contains 6 atoms per unit cell, the MgZn<sub>2</sub> and MgNi<sub>2</sub> structures contain 12 atoms per unit cell. According to Nevitt<sup>(28)</sup>, there are 223 binary Laves phases, 210 have a transition metal for at least one of the constituents, 152 have the MgCu<sub>2</sub> type structure, 67 the MgZn<sub>2</sub> type structure and only 4 the MgNi<sub>2</sub> structures. Only MgCu<sub>2</sub> and MgZn<sub>2</sub> have been studied by dHvA and these compounds would be interesting to study by HFMR, provided of course that suitable crystals could be grown.

The C16 (CuAl<sub>2</sub>) structure has 6 atoms per unit cell and its space group is tetragonal  $D_{4h}^{18}$  I4/mcm. There has been little experimental work done on these compounds aside from determining their superconducting properties. (29) Table VI gives some compounds which have the CuAl<sub>2</sub> structure. Phase diagrams of PdPb<sub>2</sub> and CuAl<sub>2</sub> indicate that these compounds might be easy to grow (see Chapter II).

The B31(MnP) structure has 8 atoms per unit cell and is orthorhombic with space group P-nma. The structure is a derivative of the B8(NiAs) structure. The dHvA work of Jan et al (15) on AuGa prompted us to study its HFMR. A list of compounds which have this structure is given in Table VII.

Table VI. Some CuAl<sub>2</sub> Type Intermetallic Compounds

CuAl <sub>2</sub>	AlHf <sub>2</sub>	AgIn <sub>2</sub>	
BFe <sub>2</sub>	GeHf <sub>2</sub>	AgTh 2	
SiZr <sub>2</sub>	${\tt RhPb}_2$	CoZr <sub>2</sub>	
GaZr <sub>2</sub>	PdPb <sub>2</sub>	CuSn <sub>2</sub>	
MnSn <sub>2</sub>	AuPb <sub>2</sub>	CuTh <sub>2</sub>	

Table VII. Some MnP Type Intermetallic Compounds

			_
AuGa	PdGe	CrAs	
PdSi	PdSn	MnAs	
PtSi	CrP	FeAs	
NiGe	MnP	CoAs	
IrGe	FeP	RhSb	
PtGe	СоР	WP	

Most of these compounds have suitable phase diagrams, especially NiGe and PdSi.

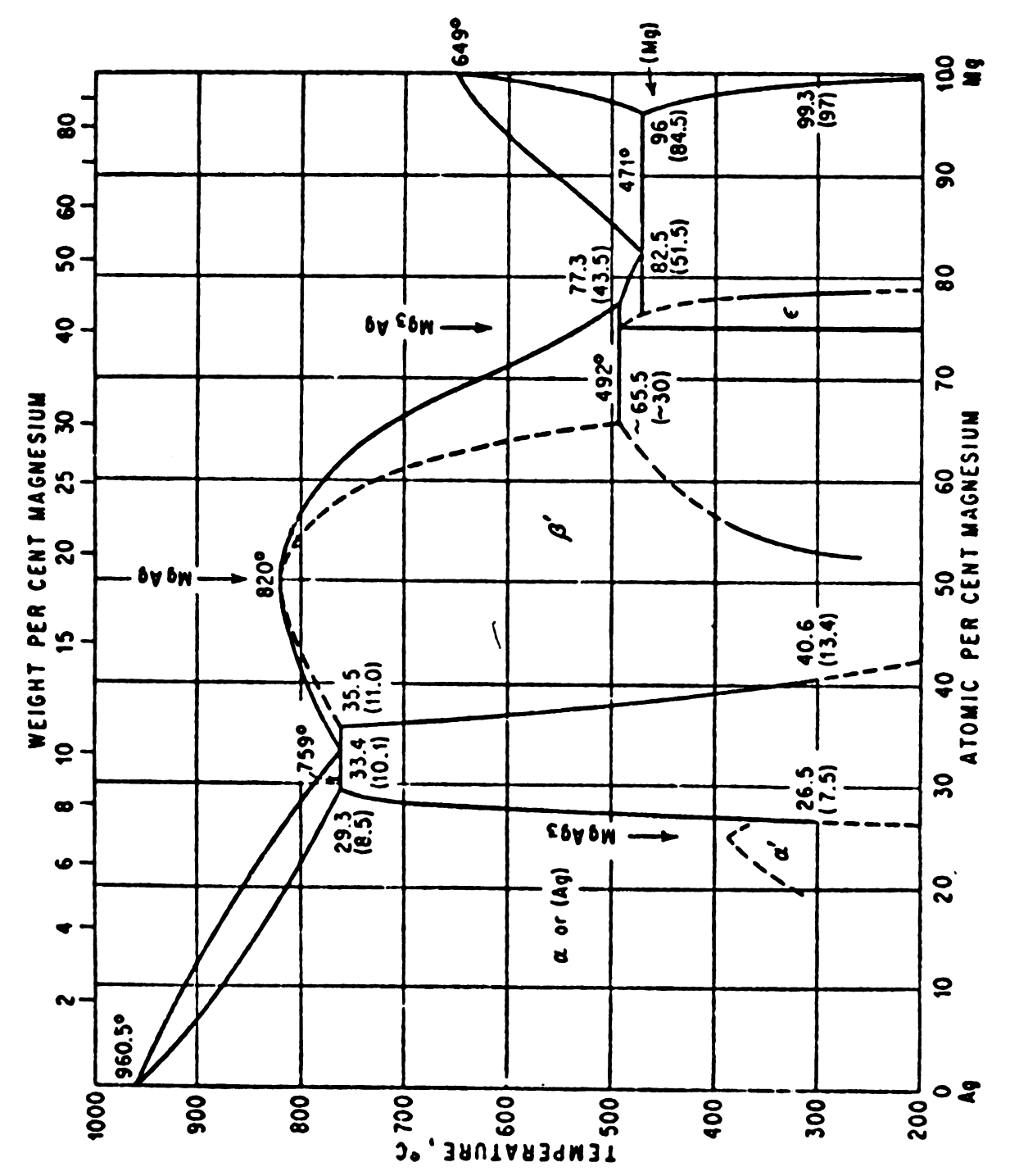
#### II. CRYSTAL GROWTH

The most important consideration in crystal growth is the phase diagram. The phase diagram indicates the feasibility of producing single crystals with high value of RRR. However, phase diagrams given in the literature are not always correct and errors in the diagrams can cause much difficulty. It is not possible to tell if the cause of crystal growing failures is due to poor technique or incorrect phase diagram information.

Figure 1 is the phase diagram of a typical B2(CsCl) structure, MgAg. The most important feature of this diagram is the large solubility of both Ag and Mg in MgAg as indicated by the width of the  $\beta$ ' region. If MgAg is grown from a melt which is not of exact stoichiometry, then the solid formed is a solution of either Ag or Mg in MgAg.

The excess Mg or Ag will act as an "impurity" scattering center in a crystal of MgAg. Sellmyer (30) developed an empirical formula to relate the RRR to the amount of impurities in a sample. The formula was derived from data on AuSn but it should provide an order of magnitude estimate for other systems.

RRR 
$$\sim \frac{10^4}{T}$$
 ,  $1 \le I \le 10^4$  (1)



Phase diagram of Mg-Ag (From Hansen, Ref. 31) Figure 1.

where I is the amount of impurity in parts per million. If a sample is made with 49.90 at .% Ag and 50.10 at .% Mg, then there would be .1 at .% excess Mg and I =  $10^3$  which would make RRR  $\approx$  10. The importance of getting as close to exact stoichiometry is evident.

The likelihood of growing B2 type intermetallic compounds with sufficiently high values of RRR is small. First, if the sample has an initial composition far from exact stoichiometry, say -5 at .% off, then the crystal grown will have a composition differing from the stoichiometric composition and the RRR will probably be low due to the "impurity" scattering mentioned above. Also, the rather large solid solubility of the constituents in the stoichiometric compound indicates that even compounds grown from stoichiometric concentrations may not be ordered enough to produce samples with sufficiently high values of RRR. However, in spite of these considerations,  $\beta$ 'CuZn has been grown with RRR  $\approx$  400. (3)

The necessity of having correct phase diagram information is seen in Figure 2, which is a phase diagram of a compound which has a maximum melting point which does not correspond with the stoichiometric compound composition. If a sample with composition 1 is grown, it would not form the solid AB upon solidification. If the sample had composition 2, the initially precipitated material would be AB but as the temperature dropped the crystal would become richer in B.



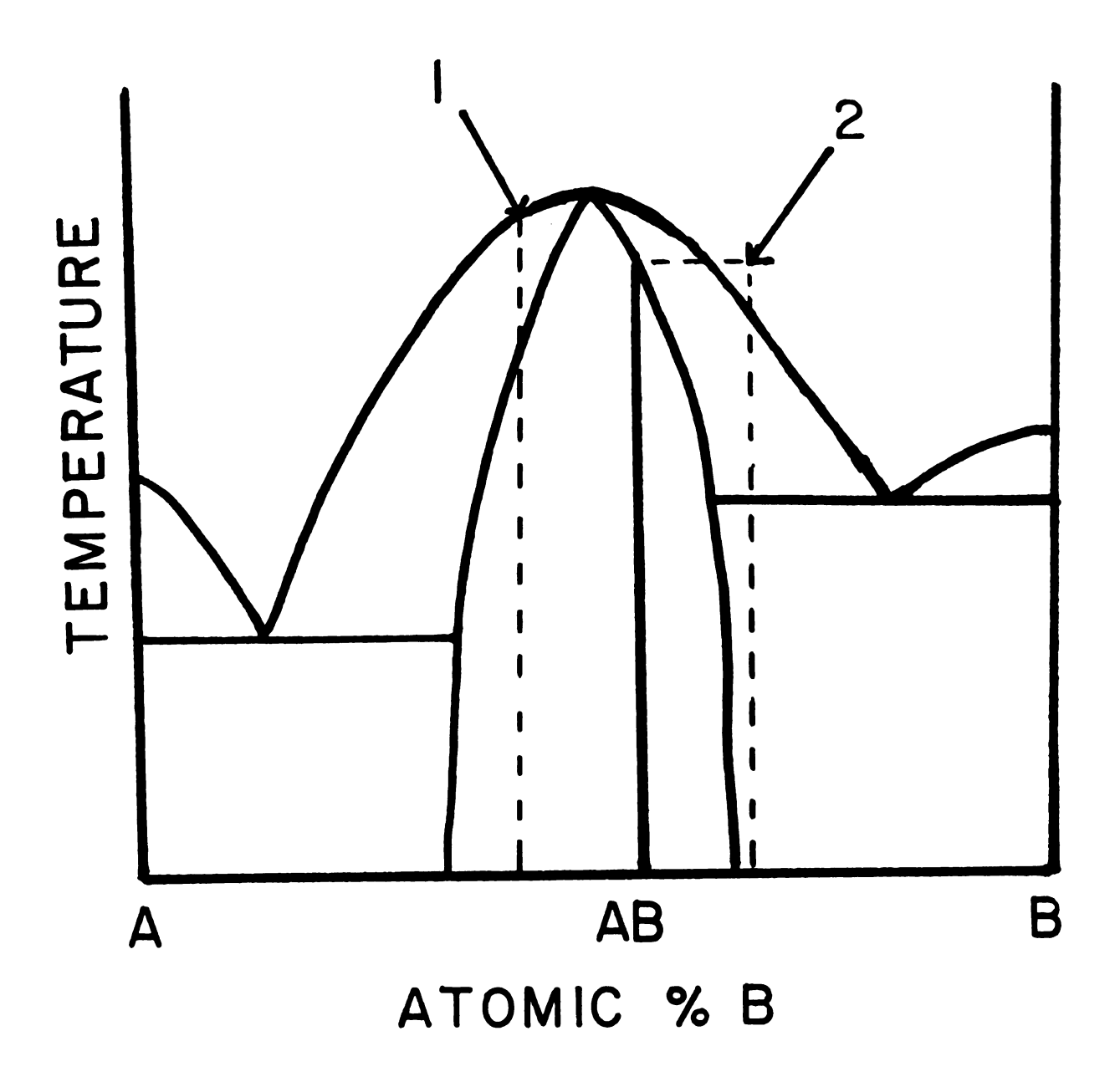


Figure 2. Phase diagram showing a compound having a maximum melting temperature at a non-stoichiometric concentration.

Two methods can be used to grow the stoichiometric compound AB. The melt's composition could contain a large excess of B and a pulling technique such as the Czochralski method could be used. Alternatively, a non-conservative method could be used if more precise stoichiometric control is desired.

The compound whose phase diagram is shown in Figure 3 has the best possibility of yielding single crystal samples with good RRR. The important feature of this diagram is the vertical line at composition AB. Such a compound is congruently melting, i.e., the liquid and solid phase are in equilibrium at the stoichiometric composition AB at temperature  $T_m$ . Also, if the width of the line is small, say less than  $10^{-3}$  at .%, then the RRR will not be limited by the solid solubility of A or B in AB.

The initial metal which is used must be of high purity in order to produce crystals with high RRR. Using Equation 1, it is evident that "59" purity metal, i.e., 99,999 at .% pure, could produce RRR of about 10<sup>3</sup> if the RRR only depended on impurity scattering. Thus, to begin with, the material must be at least "49" purity and usually "59" or "69" material is used if it is available. The cost of such high purity metal is an important boundary condition, especially in the case of Au, Pt, and Pd.

Usually the sample must be melted and grown in a crucible. Both components of a binary alloy must not react

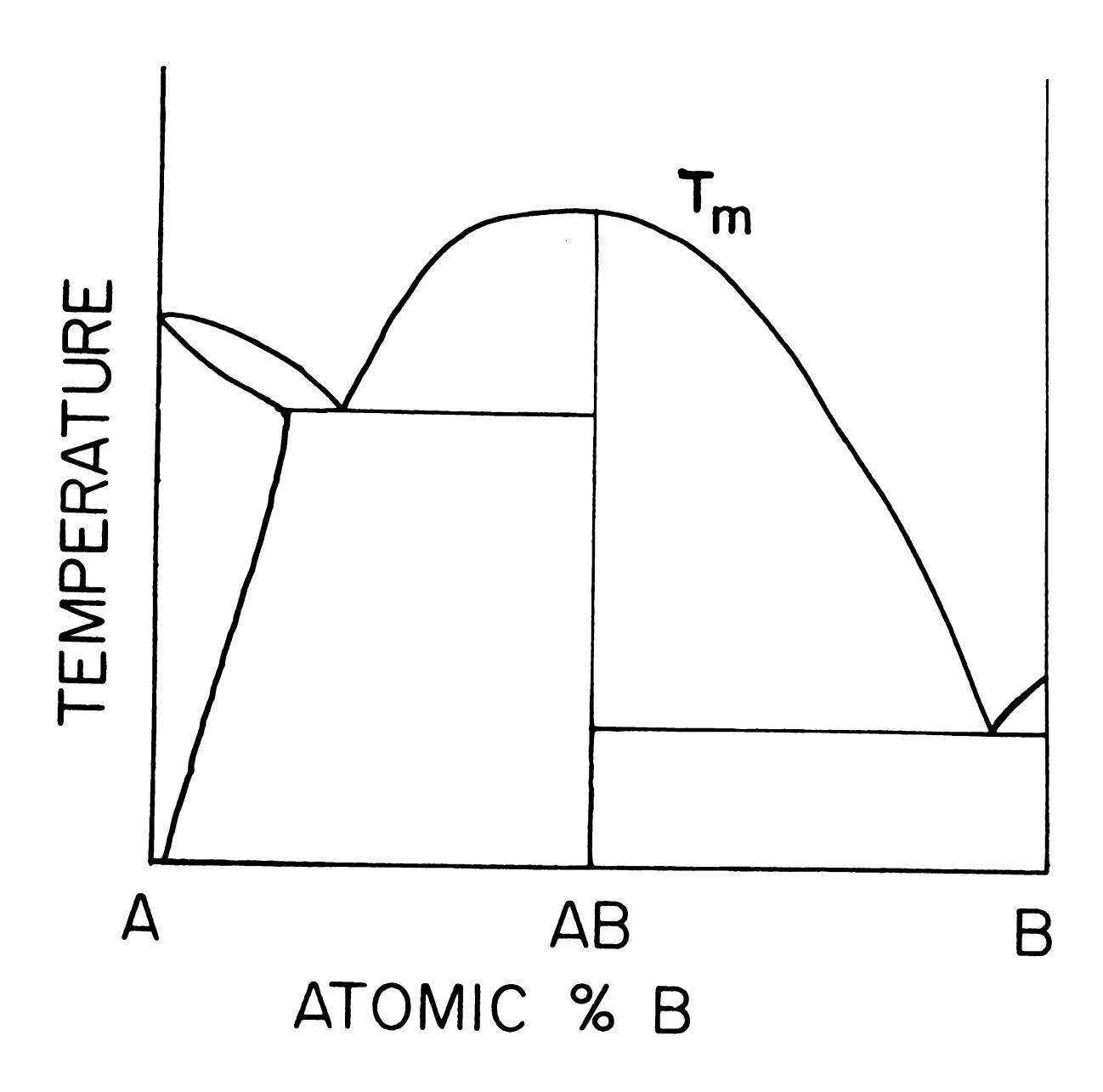


Figure 3. Phase diagram with excellent characteristics.

not be used since their vapor pressure is too high. (33) Of course, a protective atmosphere of argon or some other non-reactive gas can be used to cut down the loss of material. However, even one atmosphere of pressure is not sufficient in some cases and the use of gases could introduce additional impurities.

The growth of good single crystals, even the pure metals, is always an art. The problems involved are numerous.

First, the temperature of the sample must be measured and controlled. Parameters such as growth rate and temperature gradient are instrumental in the process of growing good single crystals. There have been many books and papers written on crystal growth techniques, yet it still remains an art and each compound requires ingenuity.

The ultimate test of the single crystal is its RRR. As the crystal is cooled to 4.2°K, it may undergo a martensitic phase transformation as happens in β'AuZn<sup>(34)</sup>. Such a phase change is thought to occur when the free energy of the crystal can be lowered by assuming a different structure. It is difficult to predict such a phase change and the direct observation of the phase change requires a low temperature x-ray diffraction unit.

ris

; lai: Vas (

?aga:

Payce

æd e

retic

Well a

iions

of the

Mined

ive to st.ape

; deo

ī:igne ;6;Je

teing

dveelect

ticul

#### III. THEORY OF HFMR

Justi and Sheffers (35) in 1936 observed complicated anisotropy of the HFMR of several metals which was not explained until the mid-fifties. Fundamental theoretical work was done by Kohler (36), Chambers (37), Lifshitz, Azbel, and Kaganov (138) (LAK) and Lifshitz and Peschanskie (39,40).

Fawcett (41) gives a comprehensive review of the theoretical and experimental work done on pure metals. Since the theoretical derivations appear in the references just cited as well as in other sources, only a brief review of the assumptions and derivations will be given.

In the absence of an external electric field the motion of the conduction electrons in a metallic crystal is determined by the applied magnetic and the periodic electric field due to the lattice. The periodic potential determines the shape of the FS and produces effects such as Bragg reflection. A geometric description of the motion of an electron in a magnetic field can be obtained by assuming the electron is reflected by the Bragg planes just as in the case of x-rays being "reflected" by the planes of atoms.

Suppose that an electronic state is characterized by a wave-number  $\bar{k}$  and a band index n. Also, assume that the electron can be thought of as a wavepacket centered at a particular value of k and that the electrons obey Fermi-Dirac

statistics. These quasi-particles experience a force  $\bar{F}$  given by

$$\bar{F} = \hbar \frac{d\bar{k}}{dt} = \frac{d\bar{p}}{dt} \tag{2}$$

and have a velocity  $\bar{v}$  given by

$$\bar{\mathbf{v}} = \frac{1}{\bar{\mathbf{h}}} \, \bar{\nabla}_{\mathbf{k}} \mathbf{E}(\mathbf{k}) \tag{3}$$

where E(k) is the energy of the electron.

The quantity  $\hbar \bar{k}$ , based upon reduced wavenumber, is labeled  $\bar{p}$ , the crystal momentum and plays the role of the momentum of the electron in a classical sense. This correspondence is due to the classical mechanical result which states that the velocity of a particle is equal to the derivative of the Hamiltonian with respect to the momentum.

In the case of an external magnetic field  $\bar{\mathbf{F}}$  is given by

$$\bar{\mathbf{F}} = -\frac{|\mathbf{e}|}{\mathbf{c}} \quad \bar{\mathbf{v}} \times \bar{\mathbf{B}} \tag{4}$$

where e is the electron charge in e.s.u. and c is the velocity of light. The wavenumber  $\bar{k}$  and hence the electronic state undergo equations of motion given by

$$\frac{d\vec{k}}{dt} = -\frac{|e|}{\hbar c} \vec{v} \times \vec{B}$$
 (5)

For electrons on the FS  $\bar{v}$  is normal to the surface and thus the electron state moves along a tangent to the FS in a plane perpendicular to  $\bar{B}$ . The motion of all the electrons on the FS can thus be geometrically constructed by taking planes perpendicular to B for various heights along its direction.

The perimeter of each section defines an orbit in wavenumber space (k space).

To obtain the motion of the electron in position space where  $\bar{v} = \frac{d\bar{r}}{dt}$ , one merely substitutes this value in Equation (5) to get

$$\frac{d\vec{k}}{dt} = -\frac{|e|}{ch} \frac{d\vec{r}}{dt} \times \vec{B}$$
 (6)

Therefore the motion of the electron in position space projected onto a plane perpendicular to B is an orbit which has the same shape as the orbit in k-space but is rotated through  $\pi/2$  about the field direction and scaled by a factor of  $\hbar c/eB$ . The velocity of the electron parallel to  $\bar{B}$  varied periodically as the k vector makes its orbit in the plane  $\bot B$  in k-space. In general the velocity parallel to B does not average to zero and the net motion in position space is a helix with axis in the direction parallel to B.

If the FS is closed, the electron wavenumber will execute a periodic motion in wavenumber space. The frequency of this motion is called the cyclotron frequency and is given by

$$\omega_{\mathbf{C}} = \frac{2\pi e \mathbf{B}}{\Delta^2 \mathbf{C}} \left(\frac{\partial \mathbf{A}}{\partial \mathbf{E}}\right)^{-1} \tag{7}$$

where  $\frac{\partial A}{\partial E}$  is the derivative of the orbit area (in k-space) with respect to energy with the component of k parallel to  $\bar{B}$  being held constant. For a spherical FS,

$$\omega_{\mathbf{C}} = \frac{\mathbf{e}\mathbf{B}}{\mathbf{m}_{\mathbf{O}}\mathbf{C}}$$

where m is the rest mass of an electron. In the general case

an effective mass, called the cyclotron mass, is defined as

$$m_{H} = \frac{\hbar^{2}}{2\pi} \frac{\partial A}{\partial E}$$

which allows the cyclotron frequency to be written in the same form as that for free electrons, namely

$$\omega_{\mathbf{C}} = \frac{\mathbf{e}\mathbf{B}}{\mathbf{m}_{\mathbf{H}}\mathbf{C}}$$

The high field region is defined by the condition

$$\omega_{\mathbf{C}}^{\phantom{\dagger}} \bar{\tau} >> 1$$

where  $\bar{\tau}$  is the average time between collisions of the electrons with scattering sites such as impurity atoms, lattice imperfections, or phonons. This condition must be satisfied for all the conduction electrons.

# Orbits

Figure 4 shows some of the possible orbits for a hypothetical sample cubic lattice. This representation of the FS is called the periodically extended zone scheme. In this scheme the FS is repeated throughout k-space and the Brillouin zone boundaries are omitted. Figure 4a shows closed electron and hole orbits for B|| to [100], a high symmetry axis. Figure 4b shows a band of periodic open orbits - orbits in which the electron moves from zone to zone in the general direction X and never returns to its original position. Although this periodic motion in k-space is mathematically equivalent to repetitions of the same arc in a single zone, the motion of

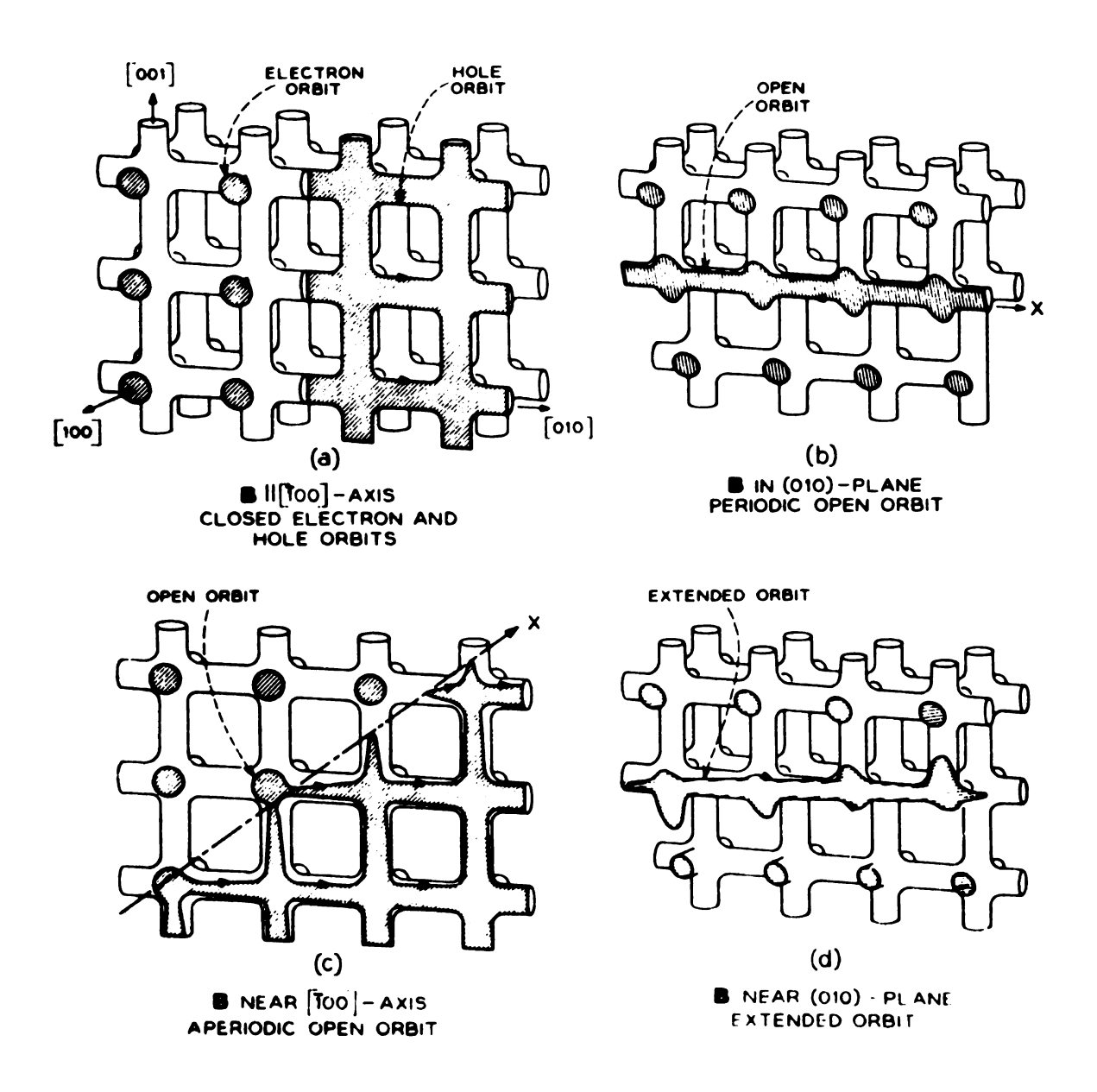


Figure 4. Various types of closed and open orbits. (From Fawcett, Ref. 41)

the electron in position space in the plane perpendicular to B is truly unbounded, neglecting collisions. Figure 4c shows an aperiodic open orbit in the general direction X. Such an open orbit is produced when B lies near a high symmetry axis in a non-symmetry plane. Aperiodic open orbits appear as two dimensional areas on a stereogram while periodic open orbits are one-dimensional, being lines on a stereogram. Figure 4d shows an extended orbit - an orbit which is closed but not contained within a single Brillouin zone, no matter where the center of the zone is located.

Topologically open orbits are equivalent to cylinders. In Figure 5, if B is in the  $K_{\underline{Y}}K_{\underline{Z}}$  plane and thus perpendicular to the cylinder axis, open orbits are found in the  $K_{\underline{X}}$  direction. If B is tipped out of the  $K_{\underline{Y}}K_{\underline{Z}}$  plane, extended orbits form and with further tipping, simple closed orbits result.

# Formal Transport Theory

The most convenient method of treating the collective motion of electrons in metals is the kinetic method. It is assumed that there exists a distribution function  $f(\bar{p},\bar{r},t)$  which gives the probability of finding an electron in a state in six dimensional phase space with momentum between  $\bar{p}$  and  $\bar{p} + d\bar{p}$ , position between  $\bar{r}$  and  $\bar{r} + d\bar{r}$ , and in the time interval between t and t + dt. If a state is occupied f = 1 while f = 0 if the state is unoccupied.

Using the semiclassical results of the previous section, the trajectory of a particular electron in phase space can be

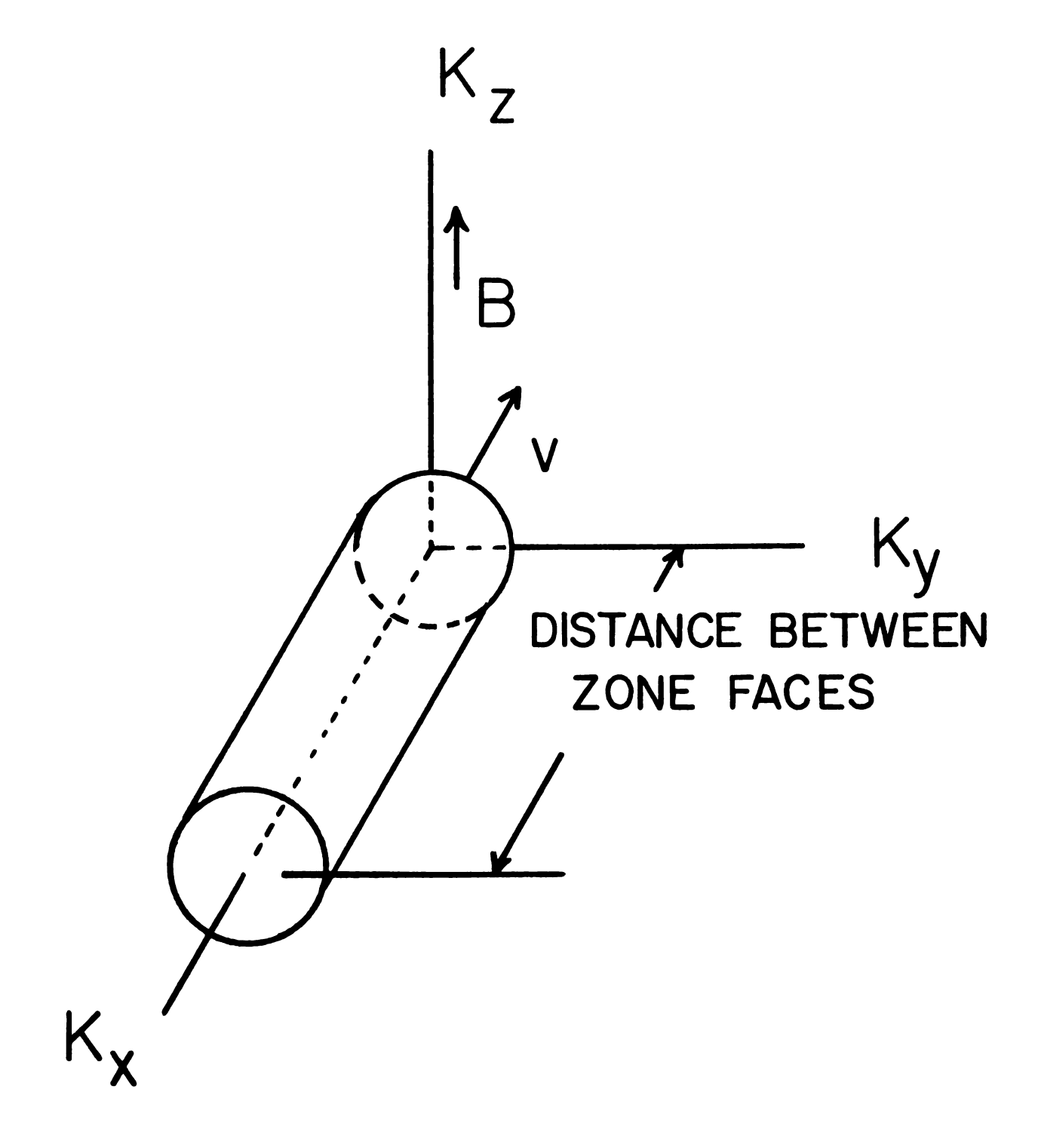


Figure 5. Model of open FS.

		•••
		:
		<b>.</b>
		:
		:
		7
		ï
		<del>,</del>

traced. If one particular electron is followed, the value of fremains constant. However, assuming that the electron can be scattered by mechanisms which are not the result of external fields, the electron will undergo discontinuous motion in phase space. The equation of motion is

$$\frac{df}{dt} = \frac{\partial f}{\partial t} + \frac{\partial f}{\partial \bar{p}} \frac{\partial \bar{p}}{\partial t} + \frac{\partial f}{\partial \bar{r}} \frac{\partial \bar{r}}{\partial t} = \frac{\partial f}{\partial t} \mid \text{Collision}$$
 (8)

which is the Boltzman transport equation in the notation of W. A. Harrison. (42)

Now  $\frac{\partial \bar{p}}{\partial t}$  is equal to the applied force while  $\frac{\partial \bar{r}}{\partial t}$  is the velocity. Equation (8) can be rewritten

$$\frac{\partial \mathbf{f}}{\partial \mathbf{t}} + \frac{\partial \mathbf{f}}{\partial \mathbf{p}} \cdot \mathbf{F} + \frac{\partial \mathbf{f}}{\partial \mathbf{r}} \cdot \mathbf{v} = \frac{\partial \mathbf{f}}{\partial \mathbf{t}} \mid \text{Collision}$$

Under steady state conditions  $\frac{\partial f}{\partial t} = 0$  and in an isothermal metal  $\frac{\partial f}{\partial r} = 0$ . In the presence of an applied electric and magnetic field  $\vec{F}$  is given by

$$\vec{F} = - |e| \vec{v} \times \vec{B} - |e| \vec{E}$$
 (9)

Thus the Boltzman equation becomes

$$(- |e| \bar{E} - \frac{|e|}{c} \bar{B} \times \bar{v}) \cdot \frac{\partial f}{\partial \bar{p}} = \frac{\partial f}{\partial t} | Collision$$
 (10)

Assuming a magnetic field in the z direction and a small electric field  $\vec{E} = E_x \hat{x} + E_y \hat{y} + E_z \hat{z}$ , the time dependence of the momenta is given by

$$\dot{p}_{x} = -|e| Bv_{y} - |e| E_{x}$$

$$\dot{p}_{y} = -|e| Bv_{x} - |e| E_{y}$$

$$\dot{p}_{z} = -|e| E_{z}$$

It is convenient to make a change of variables from  $p_{x}$ ,  $p_{y}$ ,  $p_{z}$  to  $p_{z}$ ,  $\epsilon$ , and  $\mu(\theta)$  where  $\epsilon$  is the energy of the electron and  $\mu(\theta)$  specifies the time of rotation of the electron along its trajectory in momentum space.

$$\mu(\varepsilon) = \frac{t}{T_{O}}$$

where

$$t = \frac{c}{|e|B} \int \frac{dp}{v_1} tang, \quad v_1 = (v_x^2 + v_y^2)^{1/2}$$

and

$$T_O = \frac{2\pi cm_O}{eB}$$

For closed orbits T<sub>O</sub> is the period of the orbit, and for open orbits T<sub>O</sub> can be defined as the time required for the electrons to travel from one face of the Brillouin zone to the opposite face along the open orbit direction.

The time dependencies of  $\mu(\theta)$  and  $\epsilon$  are given by

$$\dot{\mu}(\theta) = \frac{1}{T_{O}} \left( 1 - \frac{c}{v_{\perp}^{2}B} \left[ v_{x}E_{y} - v_{y}E_{x} \right] \right)$$

$$\dot{\varepsilon} = -|e| \ \bar{v} \cdot \bar{E}$$

The Boltzman equation becomes

$$-|\mathbf{e}| \frac{\partial \mathbf{f}}{\partial \mathbf{p}_{\mathbf{z}}} \mathbf{E}_{\mathbf{z}} + \frac{1}{\mathbf{T}_{\mathbf{0}}} \left(1 - \frac{\mathbf{c}}{\mathbf{v_{\mathbf{L}}}^{2} \mathbf{B}} \left(\mathbf{v_{\mathbf{x}}} \mathbf{E}_{\mathbf{y}} - \mathbf{v_{\mathbf{y}}} \mathbf{E}_{\mathbf{x}}\right)\right) \frac{\partial \mathbf{f}}{\partial \mu}$$

$$-|\mathbf{e}| \mathbf{v} \cdot \mathbf{E} \frac{\partial \mathbf{f}}{\partial \epsilon} = \frac{\partial \mathbf{f}}{\partial \mathbf{t}} | \text{Collision}$$
(11)

Assuming that the energy acquired by an electron between collisions is very small compared to the Fermi energy as well as the thermal energy kT, the Boltzman equation can be linearized with respect to E and f can be written

$$f = f_{O} - |e|t_{O}\overline{\psi} \cdot \overline{E}$$
 (12)

where  $f_0$  is the equilibrium Fermi distribution, and  $t_0$  is a relaxation time.  $\bar{\psi}$  is independent of the magnitude of the electric field, i.e.

$$\bar{\psi} = \bar{\psi}(p_z, \varepsilon, \mu)$$

The collision term can be written

$$(\frac{\partial f}{\partial t})_{\text{Collision}} = \frac{1}{t_0} (\frac{\partial f}{\partial \overline{\psi}}) (\frac{\partial \overline{\psi}}{\partial t})_{\text{Collision}}$$

Substituting for f and  $(\frac{\partial f}{\partial t})_{Collision}$  in Equation 11 and neglecting terms quadratic in E, one gets the following equation

$$\frac{\mathbf{t_0}}{\mathbf{T_0}} \frac{\partial \psi_i}{\partial \mu} + \mathbf{v_i} \frac{\partial f_0}{\partial \varepsilon} = \left(\frac{\partial \overline{\psi}}{\partial \mathbf{t}}\right)_{\text{Collision}} \tag{13}$$

LAK  $^{(37)}$  solved Equation (13) for  $\psi_i$  by a power series method. The quantitative results depend on the form of the collision operator. However, the field dependence of the magnetoresistance and the Hall coefficient for uncompensated metals can be obtained without explicit calculation. Table VIII, page 38, shows the results which are independent of the form of the

collision operator.

Once Equation (13) is solved for  $\psi$  and f determined, the current density  $\overline{J}$  is given by

$$\bar{J} = \frac{-2|e|}{h^3} \int \bar{v} f d\bar{p} = \bar{\sigma} \cdot \bar{E}$$
 (14)

The conductivity tensor  $\sigma$  is thus given by

$$\sigma_{ij} = \frac{-2e^2t_0}{h^3} \int v_i \psi_j d\bar{p}$$
 (15)

The relaxation approximation is the easiest method for obtaining quantitative results for the Boltzman equation. For such calculations, a detailed knowledge of the FS is needed. Since this information is not available on the compounds investigated in this research and in addition, the relaxation approximation is of limited usefulness in multi-banded compounds, it was not attempted. However, a brief summary of the formula obtained from the relaxation approximation will be found in the appendix.

# Compensation of Intermetallic Compounds

Before the form of the conductivity tensor is given it is necessary to define the state of compensation of a metal. A metal is said to be compensated if the total number of electrons per unit cell of the Bravais lattice summed over the electron sheets equals the total number of holes summed over the hole sheets. Fawcett (41) defines the electron/hole character of a sheet in the following manner: "the sheet has an electron/hole character if, for a non-symmetry direction giving rise to no open orbits, every cyclotron orbit is an electron/hole orbit, with the exception that, when an orbit is enclosed by one or more orbits on the same sheet of alternating electron and hole nature, the character of the sheet is determined by the outermost orbit".

Consider an intermetallic compound with  $S_1$  atoms of metal A and  $S_2$  atoms of metal B per unit cell. The capacity of each Brillouin zone is two electrons per unit cell (real space), assuming a degenerate non-magnetic metal or compound. If metal A contributes  $V_1$  electrons per atom to the conduction band while metal B contributes  $V_2$  then

$$S_1 V_1 + S_2 V_2 = 2F + (2J - n_h) + n_e$$
 (16)

where F is the number of full Brillouin zones, J is the number of hole zones,  $n_e$  the density of electrons per unit cell and  $n_h$  the density of holes. Rearranging the above equation

$$-n_A = (n_e - n_h) = S_1 V_1 + S_2 V_2 - 2(F + J)$$
 (17)

where  $n_A$  represents the net number of carriers per unit cell. If  $n_A = 0$ , the compound is compensated while if  $n_A \neq 0$ , it is uncompensated. The quantity  $V_i$  need not be an integer. However, for all metals which are nearly free electron like,  $V_i$  is assumed equal to the valence of the metal. From Equation (17) it follows that an intermetallic compound cannot be compensated if there are an odd number of conduction electrons per unit cell where as the compound may or may not be compensated if there are an even number of electrons per unit cell. However, all non-magnetic metals as well as intermetallic compounds whose galvanomagnetic properties have been studied in high magnetic fields have been compensated if they had an even number of electrons per unit cell.

The High Field Conductivity Tensor

In the high-field limit ( $\omega_{\text{C}}^{\text{T}} >> 1$ ), the electrons make many orbits before being scattered. In calculating the conductivity, the average value of the velocity taken around the orbit is used. Assuming B is in the Z direction, it can be demonstrated that the conductivity in the xy plane goes to zero as B  $\rightarrow \infty$  for closed orbits. The form of the conductivity tensor in the case of closed orbits, assuming  $a_{12} \neq 0$ , is given by

$$\sigma = \begin{pmatrix} a_{11} \frac{1}{B^2} & a_{12} \frac{1}{B} & a_{13} \frac{1}{B} \\ -a_{12} \frac{1}{B} & a_{22} \frac{1}{B^2} & a_{23} \frac{1}{B} \\ -a_{13} \frac{1}{B} & -a_{23} \frac{1}{B} & a_{33} \end{pmatrix}$$
(18)

where the Onsager relationship

$$\sigma_{ij}(B) = \sigma_{ji}(-B)$$

has been used and only the leading term in  $(\frac{1}{B})^n$  has been retained. The  $a_{ij}$ 's are independent of the magnitude of B.

The resistivity tensor, which is the experimentally measured quantity, is obtained by inverting the conductivity tensor

$$\rho_{ij} = \text{co-factor } \sigma_{ji}/|\sigma|$$

Only the leading terms of lowest order in  $\frac{1}{B}$  in each co-factor of  $\sigma_{ij}$  and  $|\sigma|$  are retained in calculating the  $\rho_{ij}$ 's.

Case 1: Closed orbits  $n_A \neq 0$ : uncompensated

$$\rho = \begin{pmatrix} b_{11} & -\frac{B\Omega}{ecn_{A}} & b_{13} \\ \frac{B\Omega}{ecn_{A}} & b_{22} & b_{23} \\ b_{13} & b_{23} & b_{33} \end{pmatrix}$$
(19)

where  $\Omega$  is the volume of a unit cell. The  $\rho_{XY}$  term gives direct information concerning  $n_A$ . The Hall coefficient  $R_H(\infty)$  is defined as

$$R_{H}(\infty) = \lim_{B \to \infty} \frac{\rho_{xy}(B) - \rho_{xy}(-B)}{2B} = \frac{\Omega}{(n_{e} - n_{h}) ec}$$
 (20)

and is independent of the direction and magnitude of B. The other coefficients of the resistivity tensor cannot be evaluated without a detailed knowledge of the shape of the FS and the collision operator.

Case 2: Closed orbits  $n_A = 0$ : compensated

In a compensated compound, since  $n_A=0$ , the coefficient of the  $\frac{1}{B}$  term in  $\sigma_{xy}$  is zero and  $\sigma_{xy} \approx \frac{1}{B^2}$  while the other terms remain the same. Thus

$$\rho = \begin{pmatrix} b_{11}B^2 & b_{12}B^2 & b_{13}B \\ b_{12}B^2 & b_{22}B^2 & b_{23}B \\ -b_{13}B & -b_{23}B & b_{33} \end{pmatrix}$$
(21)

For a compensated metal,  $\rho_{\mathbf{x}\mathbf{y}}$  does not give any direct information about the number of carriers.

# Open Orbits

Suppose that one band of open orbits is present and that they run in the general direction of the x axis in k-space. The open orbit cannot be considered to be either electron or hole-like and thus a compensated metal no longer behaves as it does in the absence of open orbits. The  $\sigma_{xy}$  component of the conductivity tensor will now contain a linear term in  $\rm B^{-1}$ . Since an uncompensated metal already has a term linear in  $\rm B^{-1}$ , the presence of open orbits only changes the coefficient of  $\sigma_{xy}$  and thus invalidates Equation (20) for  $\rm R_H(^{\infty})$ . Open orbits also produce constant field-independent terms in  $\sigma_{yy}$ ,  $\sigma_{yz}$ , and  $\sigma_{zy}$ . The conductivity tensor becomes

lase 3

Ĭ:

Case 4:

In

ispende

Case 5:

of higher

abits r

of oppos

Sign a s

: Xy

$$\sigma = \begin{pmatrix} \frac{a_{11}}{B^2} & \frac{a_{12}}{B} & \frac{a_{13}}{B} \\ -\frac{a_{12}}{B} & a_{22} & a_{23} \\ -\frac{a_{13}}{B} & a_{32} & a_{33} \end{pmatrix}$$
 (22)

Case 3: One set of open orbits.

Inverting Equation (22),  $\rho$  is given by

$$\rho = \begin{pmatrix} b_{11}^{B2} & b_{12}^{B} & b_{13}^{B} \\ -b_{12}^{B} & b_{22} & b_{23} \\ -b_{13}^{B} & b_{32} & b_{33} \end{pmatrix}$$
 (23)

Case 4: Two bands of non-intersecting open orbits in different directions.

In this case all components of  $\rho_{ij}$  tend to a limit independent of the magnitude of B since all elements of  $\sigma_{ij}$  tend to limits independent of B.

Case 5: Singular field directions at symmetry axes.

A singular field direction is defined as a crystal axis of higher than two-fold symmetry which is at the center of a region of aperiodic open orbits. The several bands of open orbits required by symmetry intersect to form closed orbits of opposite character to that of the surface. If B is along such a singular field direction

$$\sigma_{xy} = \frac{\pm ec2}{Bh^3} \left( V - \int_{-\delta/2}^{\delta/2} A(p_z) dp_z \right)$$
 (24)

ints of is the sample sample title

viere i

±0 - {

ipen Erri

: 19

iene:

ie g

- C.

147

375

where  $\delta$  is the minimum thickness along B supporting open orbits of opposite character to that of the sheet, and  $A(p_z)$  is the area of the section of the Brillouin zone for constant  $p_z$ . Since there are no open orbits when B is parallel to a singular field direction, in both compensated and uncompensated metals the resistivity tensor is given by Equation (19) but the coefficient of the  $\rho_{xy}$  term is changed from  $-\frac{\Omega}{\mathrm{ecn}_A}$  to  $-\frac{\Omega}{\mathrm{ec}(n_A\pm\Delta n)}$  where  $\Delta n$  equals the second term in Equation (24).

The magnetoresistance is defined as

$$\frac{\Delta \rho (B)}{\rho (0)} = \frac{\rho_{ii}(B) - \rho_{ii}(0)}{\rho_{ii}(0)}$$
 (25)

In Equation (22), the x-axis was deliberately chosen as the open orbit direction. Experimentally, one does not know a priori where the open orbits lie and thus they will in general make an angle  $\alpha$  with the x axis which is taken as the sample axis. In such a case the magnetoresistance would be given by

$$\frac{\Delta \rho \, \text{trans}}{\rho \, (0)} \approx C + AB^2 \cos^2 \alpha \tag{26}$$

where  $\alpha$  is the angle between the open orbit direction in k-space and the current direction J. The subscript trans means that J  $\perp$  B. C and A are constants independent of the magnitude of B.

Table VIII summarizes the important relationships which have been discussed in this section.

Table VIII. Summary of High-Field Galvanomagnetic Properties of Metals.

Transverse-even field	~ Bo	$\sim B^2$	$\sim B^2 \sin \alpha \cos \alpha$	$\sim B^o$	$\sim B^{0}$
Hall field† (transverse- odd)	$\frac{\Omega}{n_{\rm e}-n_{\rm h}}\frac{B}{ec}$	~ B	$\sim B$	$\sim B^{-1}$	$\frac{-\Omega}{n_{\rm A}\pm\Delta n}\frac{B}{ec}$
Magnetoresistance	$\sim B^0$ (saturates)	$\sim B^2$ (quadratic)	$\sim B^2 \cos^2 \alpha$	$\sim B^0$ (saturates)	$\sim B^0$ (saturates)
Type of orbit and state of compensation	I. All closed and uncompensated	II. All closed and compensated	$(n_e = n_h)$ III. Open in one direction $\ddagger$	IV. Open in two directions	V. Singular field-direction

i.e., electric field per unit current density.

 $ar{\mathtt{J}}$  is in the plane  $oldsymbol{\perp}$  B making an angle lpha with open orbit direction in k-space.

#### Physical Explanation of HFMR

Consider a metallic sample placed in a magnetic field B which is directed along the Z axis. Suppose the current axis, taken to be in the x-direction, is  $\bot$  B. Assuming that the current  $J_x$  is kept constant, the boundary conditions are  $J_y=0$  and  $J_z=0$ . Assuming  $E_z=0$ ,  $J_x$  is given by

$$J_{x} = \sigma_{xx} E_{x} + \sigma_{xy} E_{y}$$
 (27)

where  $E_{x}$  and  $E_{y}$  are related by

$$O = \sigma_{\mathbf{y}\mathbf{x}}^{\mathbf{E}} \mathbf{x} + \sigma_{\mathbf{y}\mathbf{y}}^{\mathbf{E}} \mathbf{y}$$
 (28)

For an uncompensated compound which has a FS supporting no open orbits, the conductivity tensor elements are given by

$$\sigma_{xx} = a_{11}B^{-2}$$

$$\sigma_{yy} = a_{22}B^{-2}$$

$$\sigma_{xy} = \frac{-|e| cn_A}{\Omega B} = -\sigma_{yx}$$

in the high field limit. Thus solving for Equation (28) for E

$$E_{y} = \frac{|e| cn_{A}}{\Omega a_{22}} E_{x}^{B}$$

The transverse Hall field  $E_y$  grows linearly with B and as  $B \rightarrow \infty$  the angle between the current  $J_x$  and the total electric field  $E_T = E_x + E_y$  approaches 90°. Thus the resistivity approaches saturation. In terms of Equation (27)

and

106

: 77

tie:

JE F

25

£.3

ira

ie; Pos

diz tro

sta

be s

$$J_{x} = (\frac{a_{11}}{B^{2}} - \frac{e^{2}c^{2}n_{A}^{2}}{\Omega^{2}a_{22}})E_{x}$$

and as  $B \to \infty$ ,  $\frac{a_{11}}{B^2} \to 0$  and  $\rho_{xx}$  which is given by

$$\rho_{\mathbf{x}\mathbf{x}} = \frac{\mathbf{E}_{\mathbf{x}}}{\mathbf{J}_{\mathbf{x}}} \tag{29}$$

goes to a constant independent of the field B.

For a compensated compound with no open orbits  $\sigma_{XX}$  and  $\sigma_{YY}$  have the same form but  $\sigma_{XY}$  is given by

$$\sigma_{xy} = a_{12}B^{-2}$$

Thus  $E_y$  tends to constant independent of B. In fact, since there are an equal number of electrons and holes,  $E_y$  will be very small if the mobilities of the carriers are similar and  $E_T = E_x + E_y$  will be nearly parallel to  $J_x$ . Now  $J_x$  decreases as  $B^{-2}$  as can be seen from Equation (27)

$$J_{x} = (\frac{a_{11}}{B^{2}} - \frac{a_{21}}{a_{22}B^{2}}) E_{x}$$

and  $\rho_{xx}$ , the MR, increases indefinitely as B<sup>2</sup>.

When open orbits are present, the situation changes drastically since the open orbit's current conduction is independent of the magnitude of B in the high field limit. Suppose that there is a band of open orbits running in the x direction in k-space. In the high field region, these electrons are restricted to motion in the y-z plane in real space. Since  $J_y = 0$  is still a boundary condition which must be satisfied, the electric field transverse to  $J_x$ ,  $E_y$ , must

tro

sib crs 2<sup>2</sup>

> ter sin

:0

300

iri

Œį.

tio

and Tea

i,

approach zero - if  $E_y \neq 0$ , the current carried by the electrons on the open orbits would have to be annulled by electrons undergoing closed orbits. Such an occurrence is impossible since electrons on closed orbits are very poor conductors in the high field region. Thus  $E_y \approx 0$  and the MR goes as  $B^2$  for both uncompensated and compensated materials.

When the open orbit direction in real space is parallel to the current  $J_x$ , the MR saturates. In an uncompensated material the transverse field  $E_y$  is not restricted to being zero since there are no open orbits parallel to it. Thus  $E_y \stackrel{z}{=} B$  and the MR saturates as it does when there are no open orbits. In a compensated compound since the open orbit electrons dominate the conductivity and they are independent of the magnitude of B,  $\rho_{xx}$  saturates. In terms of Equation (27) since  $\sigma_{xx}$  is independent of B

$$J_{x} = (a_{11}^{0} - \frac{a_{21}}{a_{22}B^{2}}) E_{x}$$

which immediately leads to  $\rho_{\mathbf{x}\mathbf{x}}$  going to saturation as B  $\rightarrow \infty$ .

If the current makes an angle  $\alpha$  with the open orbit direction in k-space, then

$$\rho_{xx} \approx B^2 \cos^2 \alpha$$

and if  $\theta$  is the angle between the open orbit direction in real space and the current direction,  $0 = 90 + \alpha$ , then

$$\rho_{xx} \approx B^2 \sin^2 \theta$$

in the high field limit.

#### IV. SAMPLE PREPARATION

## Crystal Growth

#### AuGa

High purity Cominco Au, either 69's or 59's, and 69's Alcoa Ga were used to make the AuGa samples. The Au was etched in warm agua regia, rinsed in distilled water and ethyl alcohol, and dried with a heat gun or at room temperature. The Ga was not etched but it was poured directly into a high purity alumina crucible from its plastic envelope after melting had been accomplished with the aid of a heat gun. empty crucible had been weighed before the Ga was poured into it and thus the amount of Ga could be determined. quired amount of Au was added, usually measured so that the compound was stoichiometric. A Mettler balance which could be read to 0.001 grams, was used. The phase diagram of Au-Ga is shown in Figure 6 and from this figure it is evident that AuGa is a congruently melting compound which can be grown from either the slightly rich Ga or Au side.

The alumina crucible was placed in a high purity graphite crucible. The graphite crucible and all other graphite crucibles and parts used in this research was then outgassed at about 1000°C and 10<sup>-4</sup> mmHg. The graphite served as a susceptor for induction heating by a Lepel furnace. A protective atmosphere of Ar was used to prevent evaporation. After melting

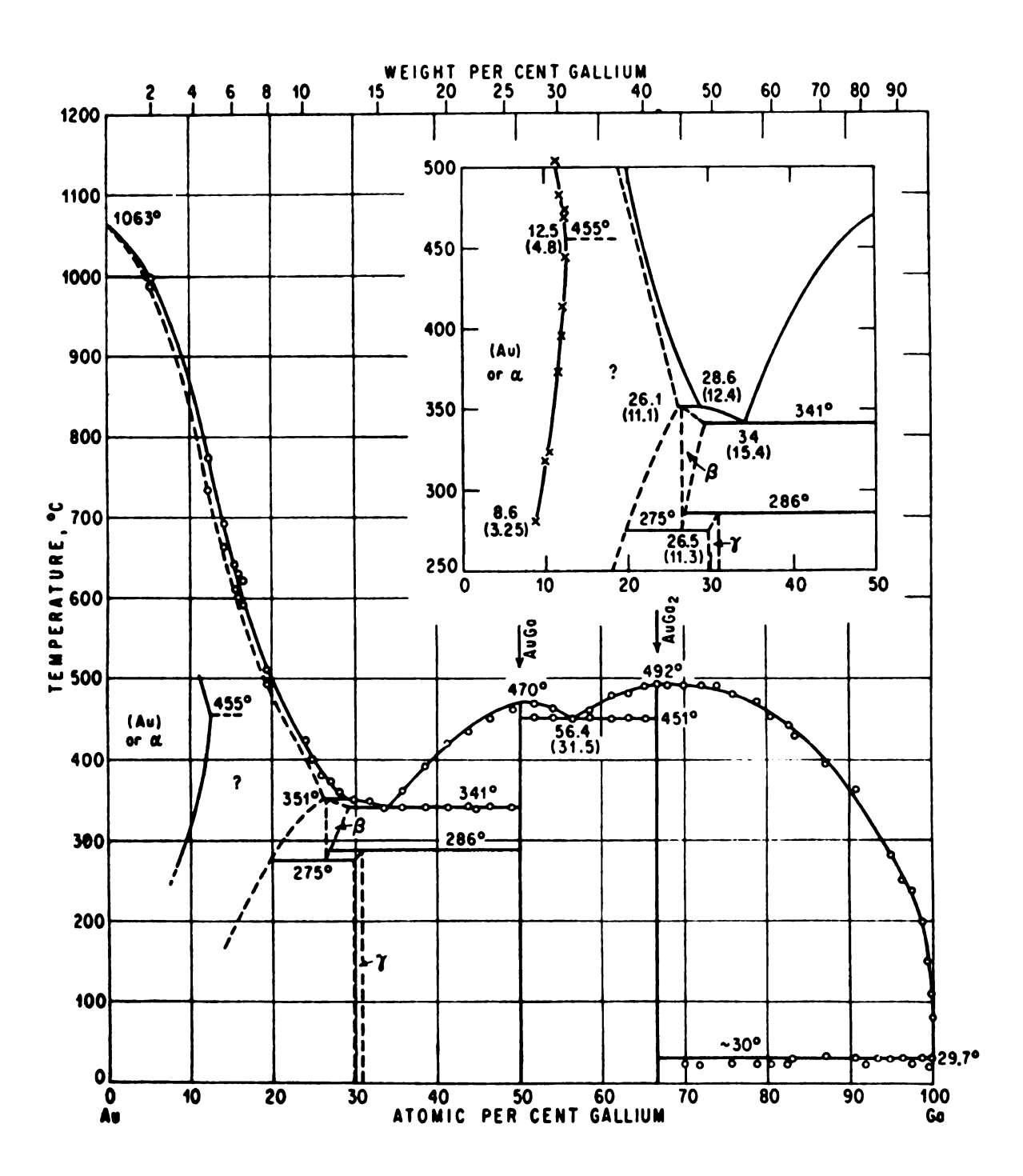


Figure 6. Phase diagram of Au-Ga (From Hansen, Ref. 31)

the metals and agitating the melt to ensure that it was thoroughly mixed, the crucible was cooled to room temperature, inverted, and placed on top of a split graphite crucible. The split crucible had three rectangular slots of 1/16 square inch by 4 inches. The crucibles were then placed in a clean quartz or Vycor tube which was then evacuated to 10<sup>-4</sup> mm Hq and filled with 1/3 atmosphere of Ar. The tube was sealed off and placed in an induction coil which could be raised slowly around the sample tube by a speed reducing system of two sets of worm and worm gears connected to a Heller variable speed motor. After melting the sample into the lower crucible the coils were raised at about 1 inch per hour. The temperature of the graphite was measured by an optical pyrometer. As the coils were raised the temperature at the bottom of the graphite crucible decreased since the coupling between the RF field and the lower part of the crucible decreased. tually solidication began when the bottom of the sample reached its freezing point. As the coil continued to be raised, more of the lower part of the crucible cooled below the freezing point of the sample thus allowing the crystal to grow from the bottom up. Since the temperature of the sample could not be measured directly, an estimate of the actual temperature was made by placing some aluminum in a graphite crucible of geometry similar to those used to grow AuGa. Thermo-couples were placed in the aluminum and measured the temperature of the sample while the optical pyrometer was used to measure the temperature of the graphite crucible. The aluminum sample

was found to be about 40°C lower in temperature than the graphite. Thus the temperature of the graphite was initially kept at least 50°C above the melting point of the sample.

The procedure just described produced two usable samples. Other attempts, using the same method, produced crystals with RRR < 30. In an effort to produce large diameter crystals from which crystals with desired orientations could be cut, a vitreous graphite crucible with 3/8" i.d. was tried. The metals were melted in the vitreous graphite crucible and then the crucible was sealed in a Vycor tube under 1/3 atmosphere of argon. The sample was then lowered slowly through a resistance furnace which had a sharp temperature gradient. The slug had a RRR = 250, but was polycrystalline. In another attempt a horizontal Bridgeman method produced samples with RRR as high as 470 but this sample was not single.

Jan et al (15) used samples grown by zone refining which had RRR=28 in their dHvA measurements.

# NiGe and Others

Ni reacts with carbon, the split graphite crucibles could not be used. The compound was grown in an alumina crucible of 7/16" i.d. which was placed in a graphite susceptor.

The sample was melted by induction heating and then a temperature gradient was moved along the enclosed sample by the coil raiser in a manner similar to that used in growing AuGa. The sample had a RRR = 30. A Vycor tube was then tried

as a crucible since a sample with a smaller diameter was desired. The compound was originally melted as in the first attempt. Then the slug was placed in a Vycor tube which was large enough at the top to accept the slug but which then narrowed to about 1/8" in diameter. The tube was sealed under 1/3 atmosphere of Ar and the slug melted down into the bottom part of the crucible. The sample was then melted by induction heating and the crystal grown as described previously. The RF field of the induction heater caused stirring of the melt which was easily observable. The sample produced in this manner had a RRR = 100 but was polycrystalline.

Due to the success in growing Au<sub>2</sub>Pb and AuPb<sub>2</sub>, the work on NiGe was discontinued. It seems that single crystals of NiGe with sufficient perfection can be grown. Placing the Vycor crucible inside a graphite susceptor to reduce the stirring of the melt might prevent the growth of stray crystals and should be tried in further growing attempts.

One other B31 type compound, PdSi, was grown during this research. A graphite crucible was used to melt the metals although carbon is known to be soluble in both liquid Si and Pd. Despite this, a single crystal of PdSi was grown but no RRR was taken because the crystal cracked while being spark planed.

Three other compounds, PtSn, CuAl<sub>2</sub>, and MgAg were grown during the course of this research. Since the dHvA work on PtSn <sup>(11)</sup> was complete and the results were inconclusive

regarding the number of electrons (8 or 10) per unit cell needed to explain the data, the HFMR might determine which number was correct. However, the crystals grown had RRR ~ 20 and were unsuitable for HFMR experiments. Four different attempts were made at growing PtSn before it was decided to try other compounds. The high cost of 59's Pt was a major consideration for termination of the work on PtSn.

CuAl<sub>2</sub>, which is the prototype for the Cl6 structures was also grown. The initial melting and solidification of the compound caused a vitreous graphite crucible to break. This breakage was probably due to the difference in thermal expansion coefficients for Al and C, that of Al being about three times greater than that of C at 700°C. An alumina crucible was also tried but the sample could not be removed after solidification. The alumina crucible also cracked but was prevented from shattering by the graphite susceptor surrounding it. These problems could be overcome by being more careful in heating and cooling the melt or using other types of crucibles. However, since the Au-Pb compounds were being tried at the same time, the work on CuAl<sub>2</sub> was discontinued when good samples of Au<sub>2</sub>Pb and AuPb<sub>2</sub> were grown.

MgAg, a B2(CsCl) structure compound whose phase diagram is given in Figure 1 was also grown. Triple distilled Mg generously provided by Dow Chemical and 59's Ag were used.

The Mg had a RRR of about 300. A graphite crucible was used to melt the metals and a single crystal of MgAg was grown with a RRR ≈ 10. Due to the rather poor RRR of the initial Mg,

the difficulty of preventing evaporation of the Mg, and the phase diagram, this compound would be difficult to grow with better RRR.

# Au<sub>2</sub>Pb and AuPb<sub>2</sub>

The phase diagram for the Au-Pb system is shown in Figure 7. Both Au<sub>2</sub>Pb and AuPb<sub>2</sub> are peritectically formed compounds. The solid of composition Au<sub>2</sub>Pb is not in equilibrium with liquid of the same composition as can be seen from the phase diagram. Therefore, a peritectic compound must be grown from a non-stoichiometric melt. The region between 45 - 70 at.% Pb will produce cyrstals of Au<sub>2</sub>Pb while the region between 72 - 84 at.% can be used to grow AuPb<sub>2</sub>.

The 69's Pb shot obtained from Cominco was etched in a l:1 mixture of acetic acid and H<sub>2</sub>O<sub>2</sub>. The Pb was then placed in a vitreous graphite crucible. No rinse was used since the bright appearance of the etched metal quickly tarnished if it was placed in water. The Pb was heated to its melting point under vacuum and the slug produced was weighed. The desired amount of 59 Cominco Au which had been prepared in the same manner as for AuGa was placed in the crucible with the Pb. The mixture was heated under a pressure of 2/3 atmosphere of Ar until all the Au had melted. The sample was cooled and then turned upside down and remelted to ensure that all the Au had melted.

In making Au<sub>2</sub>Pb either a split graphite crucible similar to those used in making AuGa or a Vycor tube was used as a

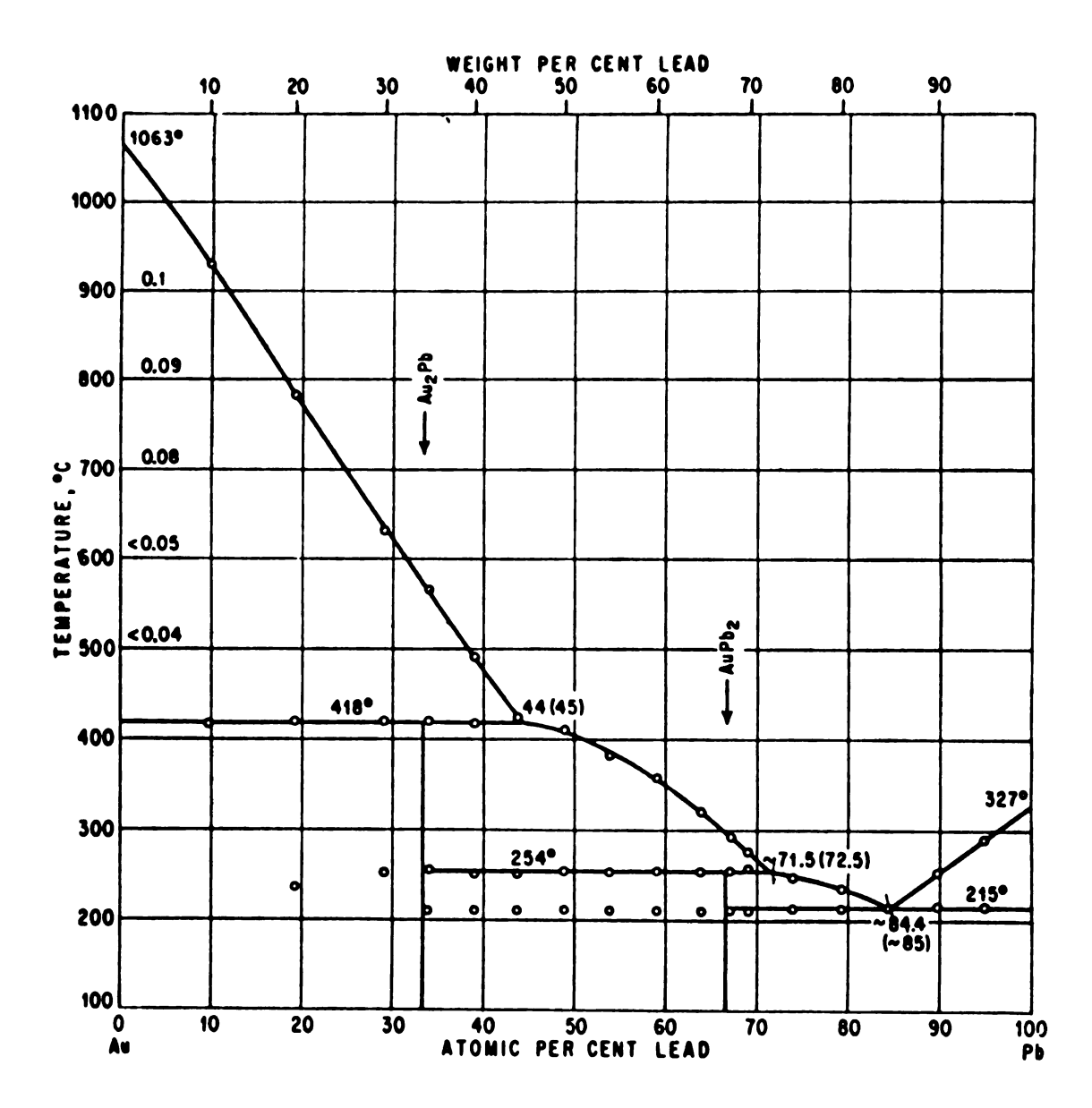


Figure 7. Phase diagram of Au-Pb (From Hansen, Ref. 31)

crucible. The slug of  $Au_2^{Pb}$  was placed in the split crucible and the crucible was put into a Vycor tube which was open at both ends. A brass water-cooled plug was inserted through the bottom end. This plug was used to make a larger temperature gradient along the graphite crucible and to lessen the effect of any radial temperature gradients. A vacuum seal was made by a rubber "0" ring quick coupling. The other end of the tube was connected to a vacuum pumping port. The Vycor tube was evacuated to  $10^{-4}$  mm Hg and then refilled with 1/3 atmosphere of Ar. The induction coils were raised along the sample by the coil raiser described previously. Samples made by this method had a maximum RRR  $\approx 170$ .

Another method of preparation was tried with the hope of producing cyrstals with higher RRR. Vycor tubing was used as the crucible and a resistance heater was used instead of the induction furnace. The sample was sealed in the tube under 1/3 atmosphere of Ar and then dropped through the furnace which had two heaters separated vertically. The upper furnace was held at a temperature slightly higher than the compound's melting point while the lower portion was held at 200°C. The temperature of the upper furnace was regulated to about 1°C. The actual temperature of the sample was not measured but the temperature of the upper half of the furnace was set so that when the sample was completely removed from the furnace, it solidified within \* 15 seconds. Once the upper furnace temperature was correctly set, the sample was lowered through the furnace at a rate of about 1/2" per hour.

This method produced a sample with RRR = 300.

The AuPb, samples were made by three different methods. All methods of preparation of the initial slug were the same as those for Au, Pb. The first method consisted of placing the slug in a split graphite crucible and then sealing the crucible in a Vycor tube. No chill plug was used. induction coils were then raised along the sample. method did not produce single crystals of AuPb2. The polycrystals were probably due to the rapid growth rate of the samples. Although the coils were moved slowly, the temperature of the graphite remained fairly constant with the temperature gradient being about 5°C/inch. Thus the amount of time between the solidification of the bottom end of the sample and the top end was probably much less than the time required for the coil to traverse the entire sample. The temperature was measured with an IR Tronics infrared pyrometer which could measure temperature in the range 200 - 600°C.

by using a Vycor tube as a crucible and lowering it through the two heater resistance furnace as described for Au<sub>2</sub>Pb.

This method produced a long single crystal with RRR ~ 320.

Another successful method consisted of using an optical zone refiner. (43) The AuPb<sub>2</sub> sample was placed in a Vycor boat, sealed in a Vycor tube under 1/3 atmosphere of Ar and heated until the entire sample was molten. The temperature was gradually reduced in such a way that one end solidified first and the crystal grew in one direction. This method

produced a large single crystal with RRR ~ 300 from which 4
samples were cut.

#### RRR Measurements

The RRR was determined by measuring the resistance at room temperature and at liquid He temperature. A Hewlett-Packard Harrison 6284A D.C. Power Supply was used as a constant current source and a Keithley 147 Nanovolt Null Detector was used to measure the voltage. The voltage and current leads were soldered to the samples with Rose's Alloy.

The Au<sub>2</sub>Pb and AuPb<sub>2</sub> samples were superconducting at 4.2°K. Roberts (29) reports a transition temperature of 4.42°K for AuPb<sub>2</sub> but does not report that Au<sub>2</sub>Pb is superconducting. The highest valued RRR sample, Au<sub>2</sub>PbIIb, does show very small voltage difference in zero field but this value is 5 times lower than the value obtained by extrapolating the magnetoresistance voltage to zero field.

The Au<sub>2</sub>Pb and AuPb<sub>2</sub> samples were placed in a dewar which was situated between the pole faces of a Harvey-Wells electromagnet. A Bell 660 Model gaussmeter was used to measure the field. Since many samples were attached to the RRR cryostat at the same time, the position of the individual samples in the magnetic field differed from sample to sample and the field read on the gaussmeter was not necessarily the field at the sample. The RRR cryostat consisted of a circuit board which had four sets of five voltage leads and four sets of current leads. The board was mounted on the

end of an epoxy rod. The positioning of the rod in the dewar and thus in the magnetic field was not very accurate, causing some additional error. The current was reversed in order to cancel out thermal voltages.

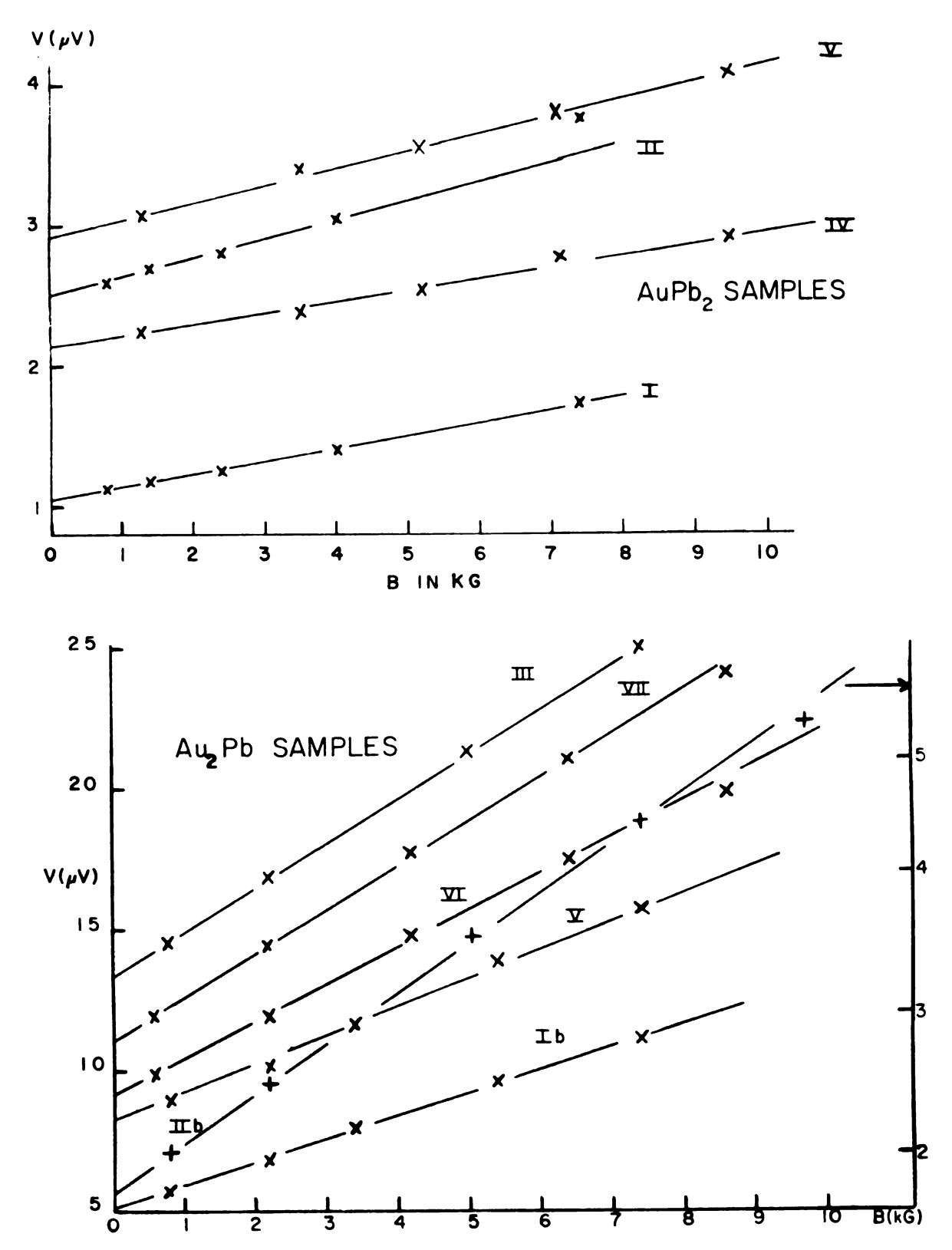
The resistance was measured at five or more fields and a linear extrapolation was made to get the zero field resistance as is shown in Figure 8. In the case of the Au<sub>2</sub>Pb and AuPb<sub>2</sub> samples, the RRR was taken of the initial slug as well as the individual samples cut from the larger slugs. The RRR increased with time and a similar effect occurred with the AuGa samples.

The initial RRR of AuGaI was 130 and the RRR measured six months later was 170. The initial RRR of the Au<sub>2</sub>Pb slug from which Au<sub>2</sub>PbIIb was cut was 240 and the RRR measured 300 nine months later. The increase in RRR is probably due to annealing of the samples at room temperature.

rent direction with respect to the major crystallographic axis. The RRR are accurate to about 10% and the error may be slightly higher for the Au<sub>2</sub>Pb samples due to the effect of alloying between the sample and the solder. This alloying effect is discussed in the section on voltage measurement.

# X-Ray Procedure

The samples were cut by a spark erosion machine which used a .002 inch diameter molybdenum wire. The AuGa and Au<sub>2</sub>Pb samples were also spark planed using a Servomet spark



Fi gure 8. V(B) vs. B for (a)  $AuPb_2$  samples and (b)  $Au_2^{Pb}$  samples.

Table IX. RRR and Orientation of Samples

	RRR	Curren θ	t Dire ø	ction* \( \psi \)
AuGaI	170	90	0	90
AuGaII	190	90	5 <b>7</b>	33
AuPb <sub>2</sub> I	480	86	54	27
AuPb <sub>2</sub> II	330	78	42	37
AuPb <sub>2</sub> IV	430	57	75	29
AuPb <sub>2</sub> V	400	81	77	18
AuPb <sub>2</sub> VI	600	32	81	61
Au <sub>2</sub> PbIb	165	31	60	86
Au <sub>2</sub> PbIIb	380	31	66	71
Au <sub>2</sub> PbIII	140	28	62	90
Au <sub>2</sub> PbV	130	31	61	83
Au <sub>2</sub> PbVI	175	23	78	71
Au <sub>2</sub> PbVII	175	14	79	79

<sup>\*</sup>  $\theta$  is the angle between [100] and current direction  $\overline{J}$ .

 $<sup>\</sup>phi$  is angle between [010] and  $\overline{J}.$ 

 $<sup>\</sup>psi$  is angle between [001] and  $\bar{J}$ .

cutter. The AuPb<sub>2</sub> samples could not be planed since even on the finest setting enough heat was generated to melt the surface layer making X-raying impossible.

Since the wire spark cutter produced uneven cuts, it was necessary to improve the surface of the AuPb<sub>2</sub> samples before X-ray pictures could be taken. The best method would have been to chemically etch the surface. However, it is very difficult to find etchants which will uniformly polish both constituents of a binary compound (especially Au compounds). There is a genuine need for references on chemical and electrochemical etchants which could be used for intermetallic compounds.

After failing to find an etchant, mechanical polishing was tried with success. Jeweler's rouge was used with a solvent like ethyl alcohol. The polish was applied with a cotton swave. About 10 to 15 minutes of polishing was necessary to produce a suitable surface for X-raying.

A Noreleo X-ray unit was used with a Polaroid camera and collimator. Initially only a Cu tube was available. The radiation from this tube was not sufficient at all wavelengths of interest and the X-ray pictures did not contain enough spots for easy identification. After a W tube was obtained, the Laue pictures improved greatly and the identification of symmetry axes was possible.

The voltage setting on the W tube was very important-especially in the case of the Au-Pb samples. The setting of
20 KV and 20 ma for about 45 minutes produced usable pictures

whereas higher KV settings produced fogged pictures which hid most of the Laue spots, even at shorter exposure times.

In order to check if the samples were single crystals, the following procedure was followed. One side of the sample was mechanically polished and then X-rayed at the top and bottom. If the two Laue photographs were identical, the opposite side was polished and X-rayed in the same manner. If all four photographs were consistent, then the sample was considered to be a single crystal.

A Laue X-ray photograph of the current axis of the samples was difficult to obtain. The small cross-sectional area of the samples was difficult to polish and thus the surface could not be prepared well enough for good quality Laue photographs. The current directions were determined by stereographic projections of the Laue photographs taken of the sides of the crystals as described above.

Since the crystal structures studied in this investigation were of a relatively complicated nature, it was necessary to check the crystal orientations with a GE diffractometer. The diffractometer was absolutely necessary in the case of AuGa where the lattice constant in the 100 direction differs by only 2% from that in the 001 direction.

In order to determine what the orientation of the two AuGa samples was, the fact that the Oll reflection is allowed while the 110 reflection is extinct in first order was used. The diffractometer was also very useful in confirming the orientation of the Au<sub>2</sub>Pb and AuPb<sub>2</sub> samples when a symmetry

axis was far from the normal to the polished side of the crystal.

#### V. EXPERIMENTAL PROCEDURE

# Cryostat and Sample Holder

The D.C. method was used to determine the field dependence of the magnetoresistance as well as its angular dependence. A constant d.c. current of 1 ampere is passed through the sample and the voltage across the sample is measured as a function of the magnitude of the magnetic field or its direction with respect to the crystal axis.

The constant current source was a Hewlett Packard 6263B DC Power Supply which is stable to 3 ma in the constant current mode. The voltage across the sample was measured by a Keithley 147 Nanovolt Null Detector. The output from the Keithley 147 was recorded on one axis of a Moseley 2D-2 X-Y Recorder as a function of the magnetic field or rotation angle which were plotted on the other axis. A Hewlett-Packard 7004B X-Y Recorder replaced the Moseley later in the research.

Figure 9 is a diagram of the sample holder which is a modification of the one described by D. J. Sellmyer (44).

The crystal could be rotated about two perpendicular axes thus allowing the magnetic field to be positioned in any desired direction with respect to the crystal axis. Rotation of the worm gear about the BB' axis is measured by the

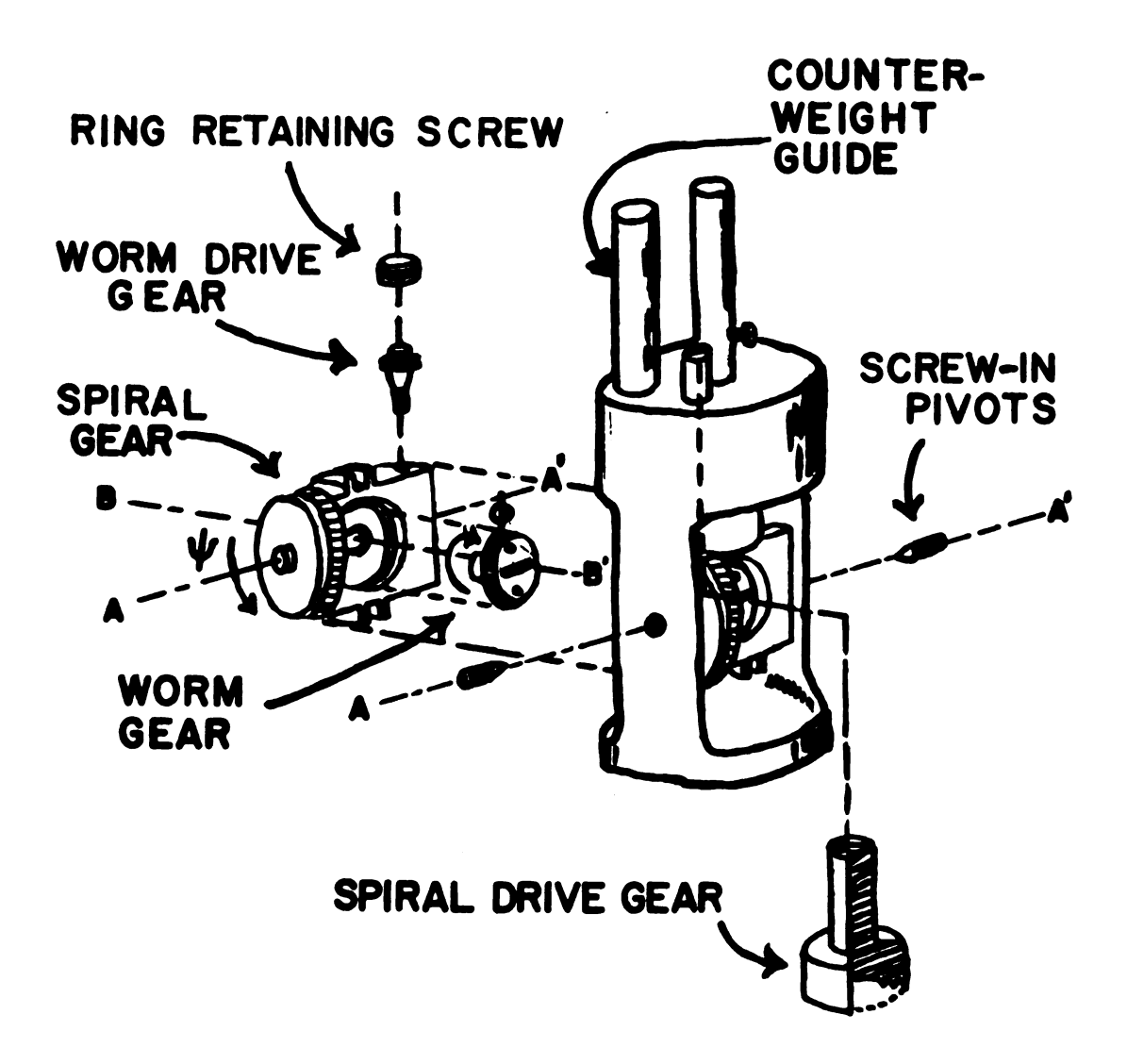


Figure 9. Sample holder.

tip angle  $\phi$  while rotation about the AA' axis is measured by the angle  $\psi$ . The sample holder was machined from standard Delrin 500 rod. This material is easily machinable, inexpensive and held up well under recycling between room and He temperatures.

The sample, of approximate dimensions 1/16" x 1/16" x 7/16" was glued to an insert with a mixture of Duco cement and acetone and the insert was then pressed into the worm gear. Two screws position the insert and prevent it from rotating. The worm gear was held in place by a brass screw and Delrin washer. These precautions are necessary since the worm gear has a tendency to leave the plane of rotation when rotated counter-clockwise. The worm was held in place by a stainless steel retaining ring which was screwed into the Delrin. The retaining ring was held in place by a small brass set screw.

The worm had a rectangular protrusion which could be engaged by a rod with a slotted end when the sample holder was in the  $\psi$  = 0 position only. Each revolution of the worm rotated the worm gear by 5.54° (360/65). The rod had to be withdrawn when a rotation plot was made.

A spiral gear arrangement provided continuous angular motion for the rotation plots. The gear had a slotted groove on top into which a rod with a screwdriver end was inserted. The rod was coupled by spur gears to a Hurst CA synchronous motor which was also coupled to a ten-turn Hellipot potentiometer with a linear tolerance of ±.50%. The voltage across

of rotation. Each revolution of the drive rod produced a rotation of 6°. One degree of rotation corresponds to 3.76 mV on the potentiometer. Due to backlash in the gears, the reproducibility of the angular rotation was about 4°. However, if data was taken with the tip angle reset each time, the reproducibility was better than 2°. A complete rotation of 180° was generally done in 5 minutes.

A brass cylinder was used as a counterweight in order to prevent the lead wires from getting tangled in the gears as the barrel was rewound. The brass cylinder was restricted from random motion by a stainless steel tube press fitted into the top of the sample holder.

## Voltage Measurements

Voltage and current leads were soldered to the samples using Stay Clean Flux and Rose's Alloy solder which is 50% Bi, 25% Pb and 25% Sn and melts at 96°C. The leads were made from \$40 Nyclad insulated copper wire. The leads were then soldered to pins on a circuit board which was mounted on the cryostat just above the magnet. During the experiment, these connections were always immersed in liquid He which prevented thermal voltages due to the soldering. The external voltage leads to the circuit board were carefully shielded and brought out to an aluminum mini-box where they were soldered to a Au plated low thermal switch with Kester Soldering Flux \$1544 and low thermal solder \$SW4337. The

input cable of the Keithley 147 was soldered to the switch with the same solder. The current leads from the circuit board were #24 Poly-thermalized insulated copper wire. The current leads were soldered to a banana plug inside a mini-box mounted on top of the cryostat.

The two voltage leads as well as the current leads soldered to the sample were tightly twisted together to minimize the pick up voltage generated as the sample holder rotated in the magnetic field. This voltage was measured by turning off the current and measuring the voltage across the sample as it rotated in a magnetic field of 98 kG. Four different samples were measured in this way and the pick up voltage varied in a monotonic way, the total variation being 1.5  $\mu V$  for the worst case. In one case spikes were observed which apparently were due to non-uniform motion of the spiral gear, that is, the gear was probably sticking between teeth. In any case, this voltage did not cause any problems since the magnetoresistance voltage was generally at least 20  $\mu V$  and the pick up voltage varied by only 1/2  $\mu V$  at the most in an interval of one revolution of the spiral gear.

The alloying effect of the Rose's Alloy solder used in connecting the probes was negligible for the AuGa samples. The solder could easily be removed with a razor blade leaving no observable alloying effect. However, the solder did alloy with the AuPb<sub>2</sub> and Au<sub>2</sub>Pb samples. The AuPb<sub>2</sub> samples did not show any measurable results due to alloying with the solder but the Au<sub>2</sub>Pb samples did.

The probe effect manifested itself when the magnetic field was swept up or down in a field interval containing 14.6 kG. Figure 10 shows the voltage across the sample as the magnetic field is swept. The abrupt change in voltage, and thus resistance, which occurs at 14.6 kG was observed in all Au<sub>2</sub>Pb samples. However, the change in resistance was much greater in those samples which had the lower RRR. In order to determine if this effect was caused by the solder, a sample which had shown the effect was spark planed until no trace of the solder remained. A pair of phospher-bronze clips were pressed onto the sample and served as voltage probes. No abrupt voltage change was observed as the field was swept from 6 to 20 kG. Thus the abrupt resistance change is due to alloying between the Au<sub>2</sub>Pb samples and the Rose's Alloy solder.

The alloy formed around the solder blobs is probably a superconducting alloy which alters the current flow through the crystal at low fields. Once a high enough field (>14.6 kG) is reached, the alloy goes normal and its effect ceases since a four probe system is used and the voltage leads draw a very small current. The Keithley 147 has an input resistance of 1x10<sup>6</sup> ohms while the sample resistance is on the order of 2x10<sup>-4</sup> ohms at 4.2°K. In the field region used to study the FS of Au<sub>2</sub>Pb (> 80 kG) the alloying effect should be oflittle consequence.

In order to eliminate unwanted voltages from the magnetoresistance probes which are caused by thermal voltages

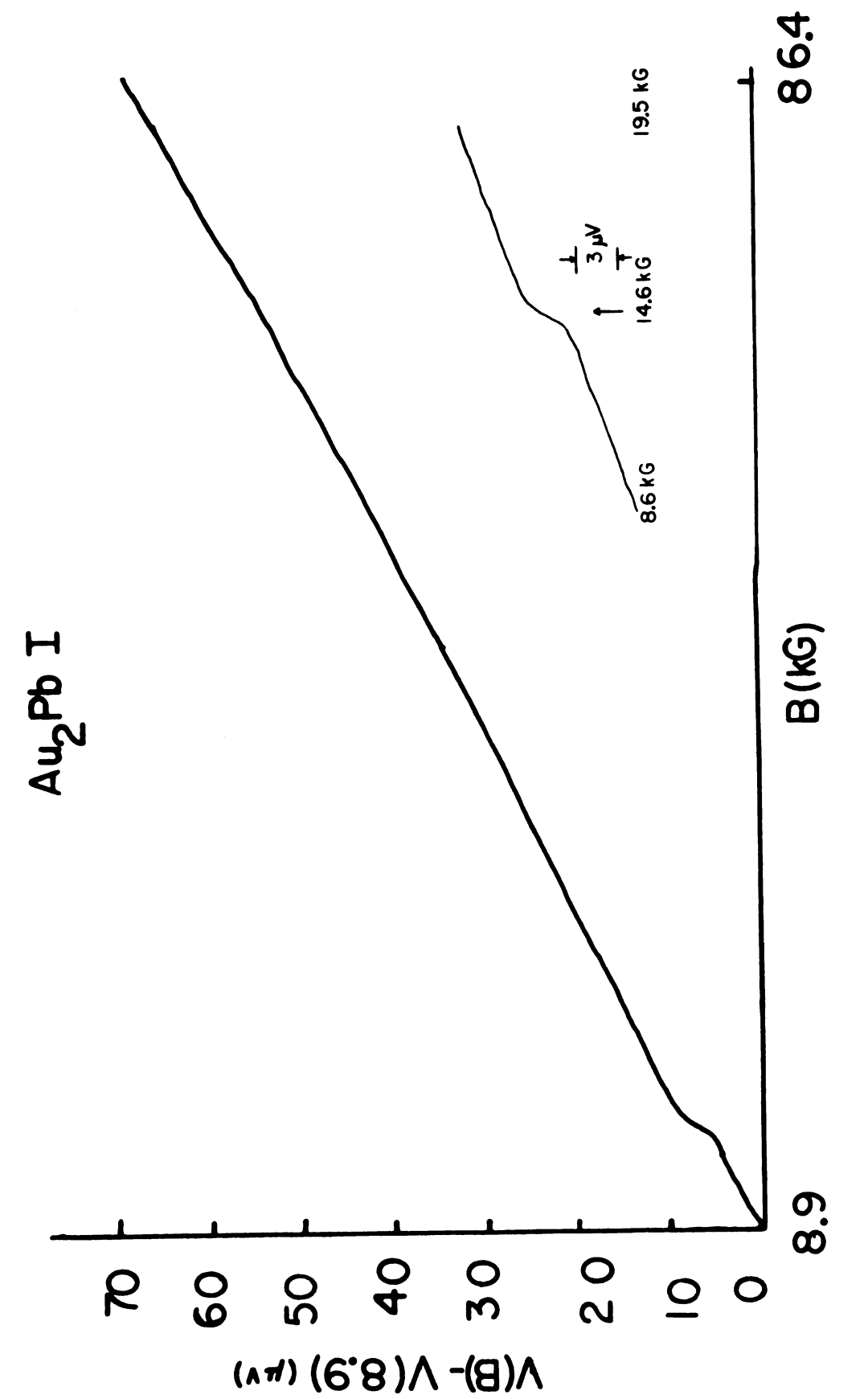


Figure 13. V(B) vs. 3 for Au<sub>2</sub>PbI.

and probe misalignment, the following sets of voltages should be taken<sup>(30)</sup>,

$$V_{MR} = \frac{1}{4} [V(+I,+B) + V(+I,-B) - V(-I,+B) - V(-I,+B)]$$

$$- V(-I,-B)]$$
(30)

The sample holder was designed to rotate a full 360° in order to allow the field to be positioned in both the +B and -B The current could also be reversed. The complete directions. procedure of measuring V<sub>MR</sub> was done on AuGa I, AuPb, VI, Au<sub>2</sub>Pb VI and Au<sub>2</sub>Pb IIb. The AuGa and AuPb<sub>2</sub> samples showed no unexpected results and a measurement of V(+I,+B) was taken to be equal to  $V_{MR}^{}$ . For  $Au_2^{}Pb$  IIb some anomalies occurred and these will be discussed in a later section.

The field dependence of the HFMR as expressed by the coefficient m is defined by

$$\Delta \rho / \rho_{O} = aB^{m}$$
 (31)

Since 
$$\Delta \rho / \rho_O = \frac{V(B) - V(0)}{V(0)}$$
 where  $V(B)$ 

is the value of the voltage at the field B; the voltage V(B) was taken at two different fields and m was calculated by

$$m = \frac{\log \frac{V(B_1) - V(0)}{V(B_2) - V(0)}}{\log \frac{B_1}{B_2}}$$
(32)

The V(B) was read from the X-Y recorder trace. When the Keithley 147 was on the 30  $\mu$ V range, the X-Y recorder signal could be read to ~ .08  $\mu V$ , on the 100  $\mu V$  it could be read to

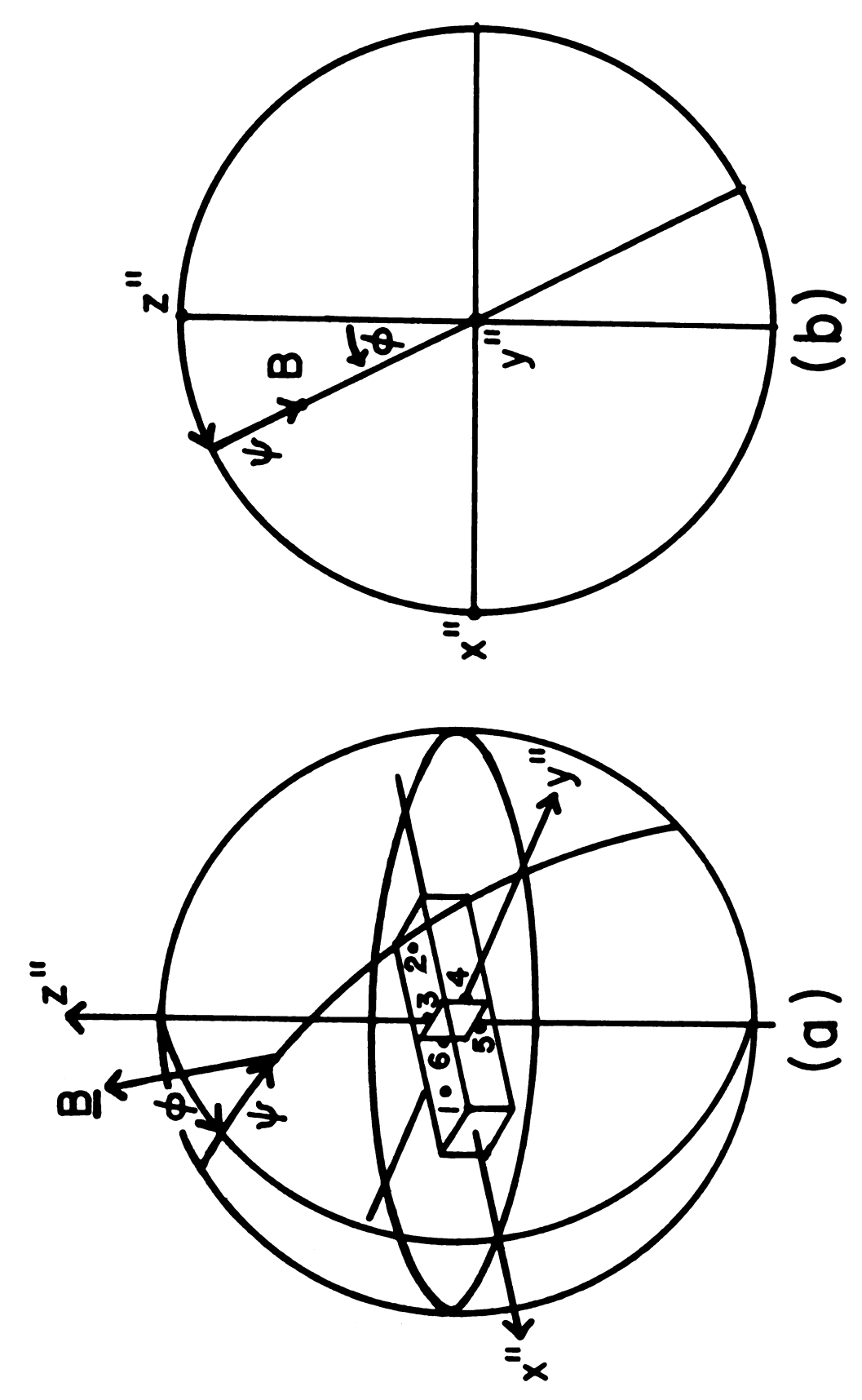
~ .25  $\mu$ V, and on the .3 mV range it could be read to ~ .8  $\mu$ V. Thus the error incurred by reading V(B) from the X-Y recorder trace was less than the fluctuations caused by the rotation of the sample holder.

Assuming that the magnitude of B is accurage to  $\pm 5\%$ , the value of m is probably accurate to ~ 20% when V(B) is between 15-30  $\mu$ V, ~ 13% when V(B) is 30-100  $\mu$ V, and ~ 11% when V(B) is 100-300  $\mu$ V. The higher error for the lower voltages is due to the pick up voltage generated as the sample rotates in the magnetic field.

# Analyses of Tipping Arrangement

Figure 11a shows the voltage probe positions and the direction of the magnetic field with respect to the crystal as the sample is rotated. The rotation of the crystal clockwise about the y" axis ( $\phi$ ) can also be represented by a rotation of the magnetic field counter-clockwise about y" with the crystal remaining fixed. The same interpretation can be applied to rotations about the x" axis ( $\psi$ ). The magnetoresistance probes are numbered 1 and 2 and are separated ~1/8" while the other four probes are used for Hall voltage measurements. Figure 11b shows a stereographic projection of the motion of the magnetic field with respect to the crystal.

The resistivity tensor is given by Equation (21) when there are no open orbits and is repeated below



Rotation and tipping geometry and (b) stereographic projection of motion of B. Figure 11(a).

$$\rho \text{ (closed)} = \begin{pmatrix} b_{11}^{c}B^{2} & b_{12}^{c}B^{2} & b_{13}^{c}B \\ b_{12}^{c}B^{2} & b_{22}^{c}B^{2} & b_{23}^{c}B \\ -b_{13}^{c}B & -b_{23}^{c}B & b_{33}^{c} \end{pmatrix}$$
(21)

When there are open orbits in the  $X_2$  direction in k-space and thus in the  $X_1$  direction in real space, the resistivity tensor is given by

$$\rho \text{ (open)} = \begin{pmatrix} b_{11}^{0} B^{0} & b_{12}^{0} B^{0} & b_{13}^{0} B \\ -b_{12}^{0} B^{0} & b_{22}^{0} B^{1} & b_{23}^{0} B \\ -b_{13}^{0} B & b_{23}^{0} B & b_{33}^{0} \end{pmatrix}$$
(33)

Now the effect on the resistivity tensor of tipping the crystal from the transverse  $(\bar{J}\perp \bar{B})$  geometry will be considered.

Figure 12 shows the non-transverse geometry, i.e., B is not  $\bot$   $\bar{J}$ . The coordinate systems shown are related in the following way. The  $S(X_1,X_2,X_3)$  system is the initial coordinate system. When  $\gamma$  and  $\beta=0$ , the current direction  $\bar{J}$  is along  $X_1$ . The  $S(X_1',X_2',X_3')$  coordinate system is obtained from  $S(X_1,X_2,X_3)$  by a rotation of  $\gamma$  about the  $X_3$  axis and  $S''(X_1',X_2',X_3')$ , which is fixed to the crystal, is obtained from  $S'(X_1',X_2',X_3')$  by a rotation of  $\beta$  about  $X_2'$ . The  $X_1''$  axis is the current direction which makes an angle  $\beta$  with the  $X_1$  axis and an angle  $\beta$  with the  $X_1'$  axis.

The rotation matrices for rotations about the  $\mathbf{X}_1$ ,  $\mathbf{X}_2$ , and  $\mathbf{X}_3$  axes are

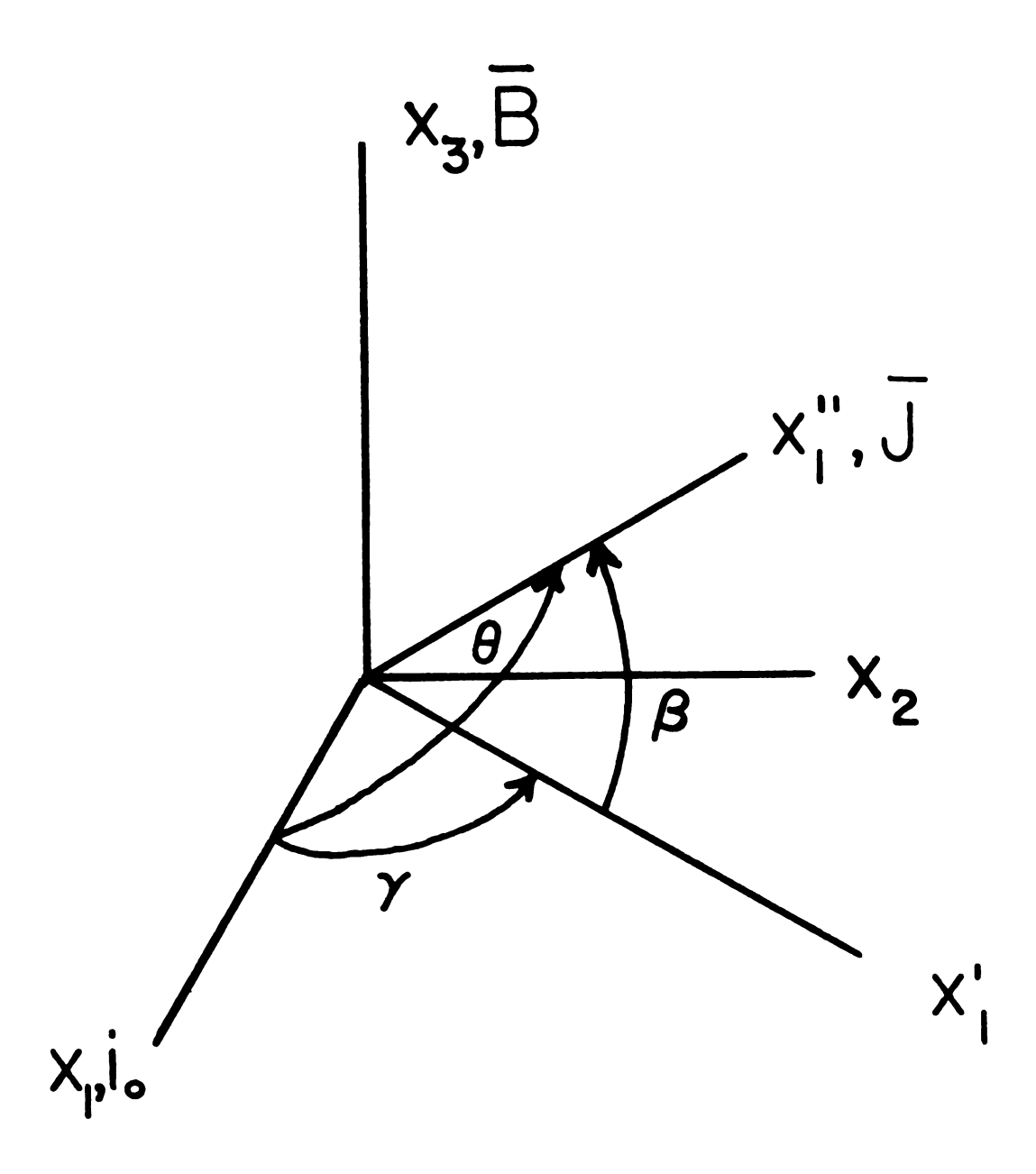


Figure 12. Non-transverse geometry.

$$R_{X_{1}} = \begin{pmatrix} 1 & 0 & 0 \\ 0 & \cos \varepsilon & \sin \varepsilon \\ 0 & -\sin \varepsilon & \cos \varepsilon \end{pmatrix} \quad R_{X_{2}} = \begin{pmatrix} \cos \varepsilon & 0 & -\sin \varepsilon \\ 0 & 1 & 0 \\ \sin \varepsilon & 0 & \cos \varepsilon \end{pmatrix}$$

$$R_{X_{3}} = \begin{pmatrix} \cos \varepsilon & \sin \varepsilon & 0 \\ -\sin \varepsilon & \cos \varepsilon & 0 \\ 0 & 0 & 1 \end{pmatrix}$$

where  $\varepsilon$  is the angle of rotation taken to be positive in the counter-clockwise direction.

The voltage is measured in the sample's coordinate system,  $S''(X_1'', X_2'', X_3'')$  and can be related to the resistivity tensors given for the  $S(X_1, X_2, X_3)$  system, Equations (21) and (33). The transformation is given by

$$\rho'' = R_{X_{2}^{1}}(\beta) R_{X_{3}}(\gamma) \rho R_{X_{3}^{1}}(\gamma) R_{X_{2}^{1}}(\beta)$$

The measured MR is given by the  $\rho_{11}^{\text{"}}$  component of the resistivity tensor

$$\rho_{11}^{"} = \rho_{11}\cos^{2}\beta\cos^{2}\gamma + \rho_{12}\cos^{2}\beta\cos\gamma\sin\gamma + \rho_{13}\cos\beta\sin\beta\cos\gamma$$

$$+ \rho_{21}\cos^{2}\beta\cos\gamma\sin\gamma + \rho_{22}\cos^{2}\beta\sin^{2}\gamma + \rho_{23}\cos\beta\sin\beta\sin\gamma$$

$$+ \rho_{31}\cos\beta\sin\beta\cos\gamma + \rho_{32}\cos\beta\sin\beta\sin\gamma + \rho_{33}\sin^{2}\beta.$$

If  $\overline{B}$  is tipped infinitesimally away from the  $X_3$  axis in any direction except in the  $X_2X_3$  plane, then the open orbit in the  $X_1$  direction is missed while  $\gamma$  and  $\beta$  remain the same to a first approximation. Thus as B goes from a direction which produces open orbits to a direction which does not, the

MR voltage as measured by  $\rho_{11}^{"}$  will change. The values of  $\rho_{11}^{"}$  for both cases, keeping terms in the highest power of B only are,

$$\rho_{11}^{"}(\text{closed}) = B^{2}\cos^{2}\beta \{b_{11}^{C}\cos^{2}\gamma + 2b_{12}^{C}\cos\gamma\sin\gamma + b_{22}^{C}\sin^{2}\gamma \}$$

$$\rho_{11}^{"}(\text{open}) = B^{2}b_{12}^{O}\cos^{2}\beta\sin^{2}\gamma$$

The ratio of the two values of  $\rho_{11}^{"}$  gives,

$$\frac{\rho_{11}^{"}(\text{open})}{\rho_{11}^{"}(\text{closed})} \approx \frac{b_{22}^{O} \sin^{2} \gamma}{b^{C} (\cos \gamma + \sin \gamma)^{2}}$$

if the magnitude of the  $b_{1j}^{C}$ , s, represented by the symbol  $b_{1j}^{C}$ , are approximately the same. By sweeping B through a region of open orbits, a dip in the MR is expected if  $b_{1j}^{C}\sin^{2}\gamma \cdot b^{C}(\cos \gamma + \sin \gamma)^{2}$  or a peak is expected if  $b_{1j}^{C}\sin^{2}\gamma \cdot b_{C}(\cos \gamma + \sin \gamma)^{2}$ .

We, as well as other investigators  $^{(13,45)}$ , have encountered both types of behavior. However, when  $\beta$  becomes large, the dip can be washed out due to the dominance of the longitudinal magnetoresistance which saturates in all cases.

The angles of rotation of the sample holder do not correspond exactly to  $\gamma$  or  $\beta$ . However, with the help of some geometry the relationship between the angles is seen to be

$$\cos\beta = (\cos^2\phi\cos^2\psi + \sin^2\psi)^{1/2}$$

 $sin\gamma = tan\phi sin\psi$ 

 $\cos\theta = \cos\beta\cos\delta$ 

The rotation plots are taken for different values of \$\phi\$. The position of the magnetic field corresponding to sharp minima and maxima are plotted on a stereogram as is the orientation of the crystallographic axes of the sample. Usually the sample axis (current axis) did not correspond to a major symmetry axis. The minima corresponding to a particular open orbit direction are connected and form a plane in k space. The direction of the normal to this plane is the open orbit direction in k or reciprocal space. For compensated compounds, several samples with different current directions are needed to ensure that all open orbit directions are obtained. If the angle between the open orbit direction in k-space and the current direction is small the open orbit can easily be missed.

The orientation of the samples with respect to the magnetic field direction could not be directly determined.

Usually the sample was X-rayed while mounted on the worm gear which was then placed on a goniometer. Thus errors of -5° in the orientation of the sample are likely. The exact orientation was determined by fitting the planes formed by the sharp minima with the approximate orientation obtained from the Laue X-ray photographs.

## VI. RESULTS

#### **AuGa**

AuGa has the B31 (MnP) structure which is orthorhombic with space group Pnma and 8 atoms per unit cell. The B31 structure is a derivative of the B8(NiAs) structure and Figure 13 shows how the two structures are related. The lattice constants (15) for AuGa are given in Table X. Note that the a and c axes differ by only 2%.

Figure 14 shows a plot of V(B) versus ψ for AuGaI at fixed magnetic field B = 82 kG. The letters designate specific field directions. Figure 15 shows curves for V(B) versus B for the specified values of ψ. The plots show the interval between 22 to 82 kG. Note that curve b in Figure 15 is a very slowly increasing function while curves a and c are beginning to show a quadratic field dependence at higher fields. Since the time required to sweep the field from 0 to 82 kG is about 40 minutes, this method of determining the field dependence of the HFMR was not used for economic reasons. Also, the positioning of the magnetic field with respect to some particular direction in the crystal was difficult and could only be determined to ~4°.

Figure 16 shows how the field dependence of the HFMR was determined. The rotation plots were taken at two different fields, 99 kG and 88 kG with tip angle  $\phi$  = 0. By assuming

Figure 13. Comparison of NiAs and AuGa structures. The lower diagrams are projections taken along the c axis in NiAs while the upper diagrams are taken along the a axis. The height of the atoms above the projection plane is given by the numbers beside the atoms. Dark spheres represent Ni(Au) atoms while light spheres represent As(Ga) atoms.

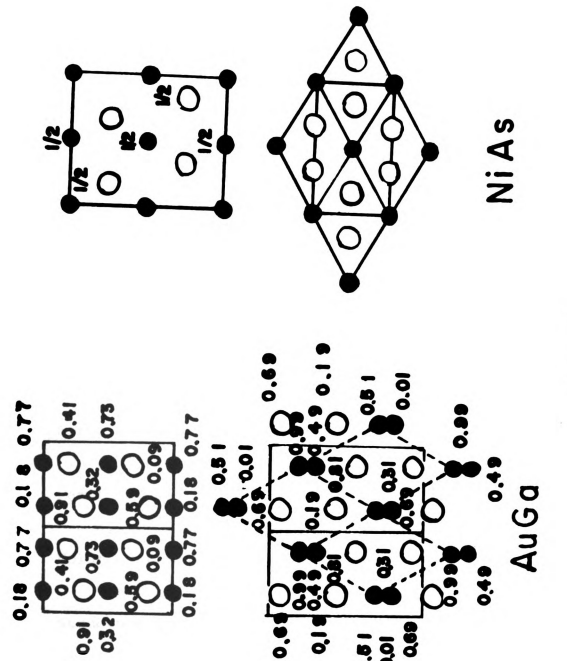


Figure 13.

Table X. AuGa Lattice Constants (from Jan et al (15))

R	oom Temperature	Liquid He Temperature (4.2°K)		
a	6.260 Å	6.196 Å		
b	3.464	3.488		
С	6.396	6.354		

Table XI. FS Parameters for AuGa

Reciprocal lattice vectors

 $a* = 1.014 \text{ Å}^{-1}$ 

 $b* = 1.801 \text{ Å}^{-1}$ 

 $c* = 0.9889 \text{ Å}^{-1}$ 

Fermi Energy

 $\epsilon_{\mathbf{F}} = 8.698 \text{ eV}$ 

Fermi Radius

 $k_f = 1.511 \text{ Å}^{-1}$ 

Volume Brillouin Zone

 $V = 1.806 \text{ Å}^{-3}$ 

Structure factors of zero value

h00: h = 2n+1

0k0: k = k=2n+1

00 l: l = 2n+1

0kl: k+l = 2n+1

hk0: h = 2n+1

# AuGa I

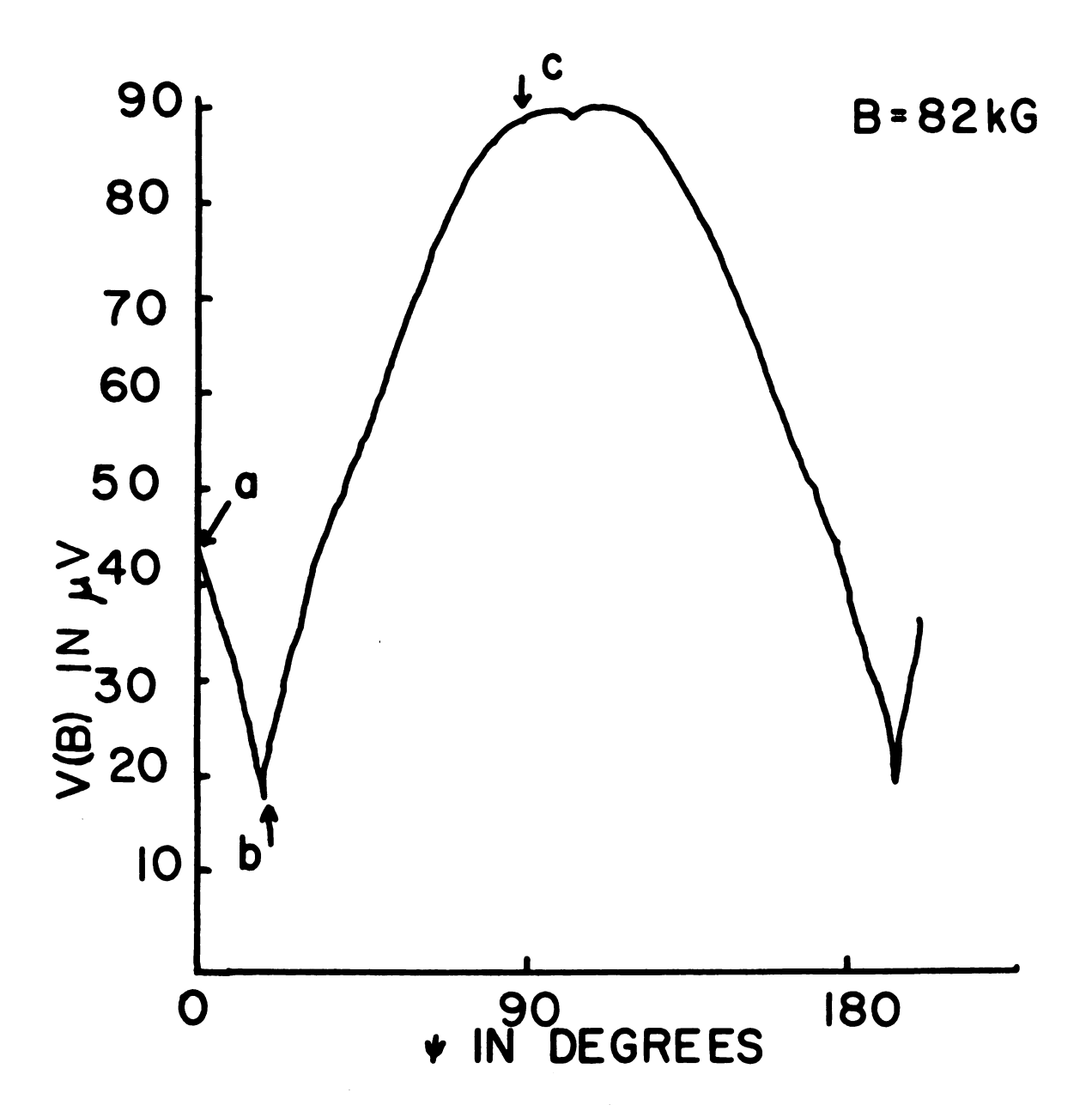


Figure 14. V(B) vs.  $\psi$  for AuGaI.

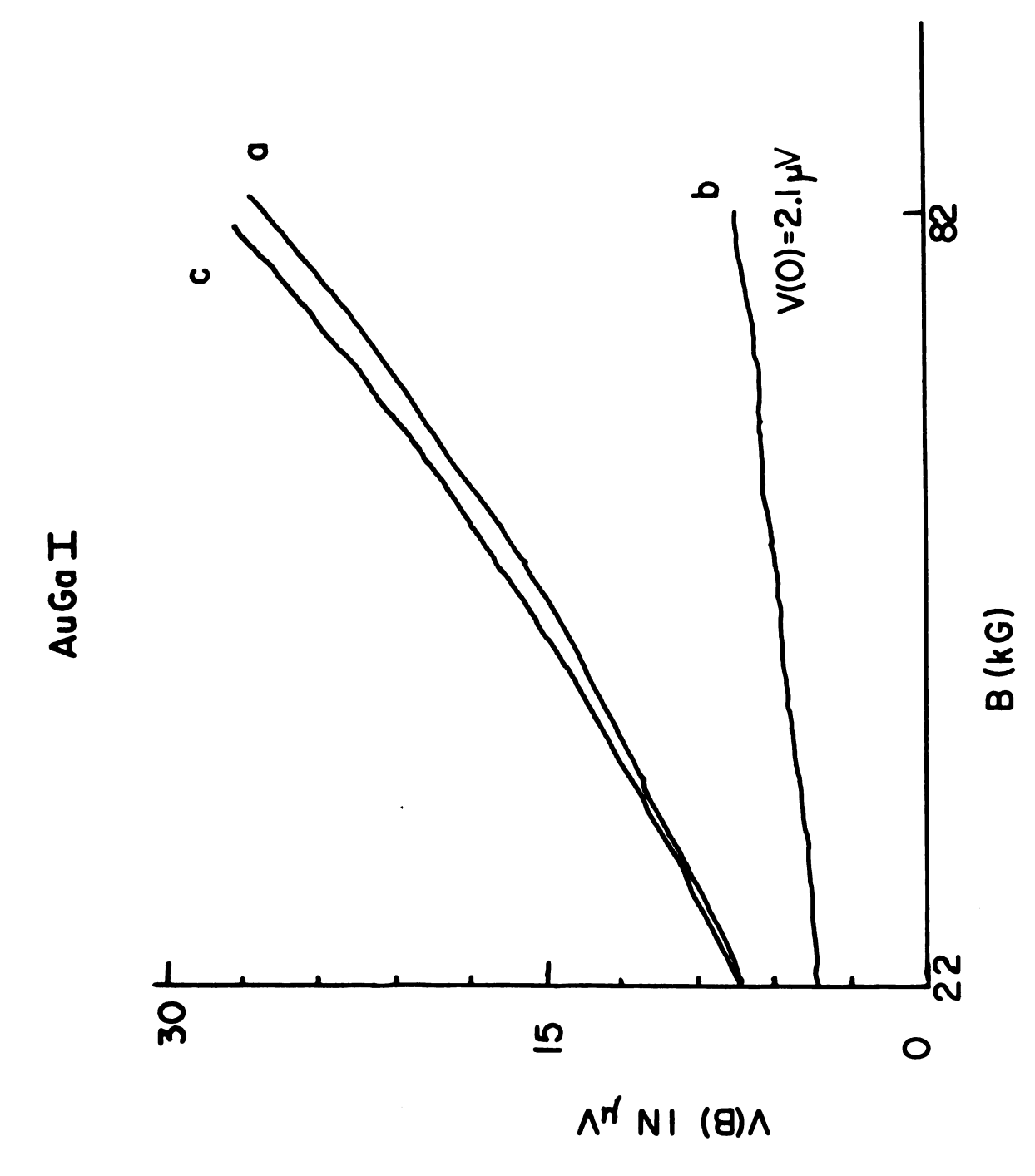


Figure 15. V(B) vs. B for AuGaI.

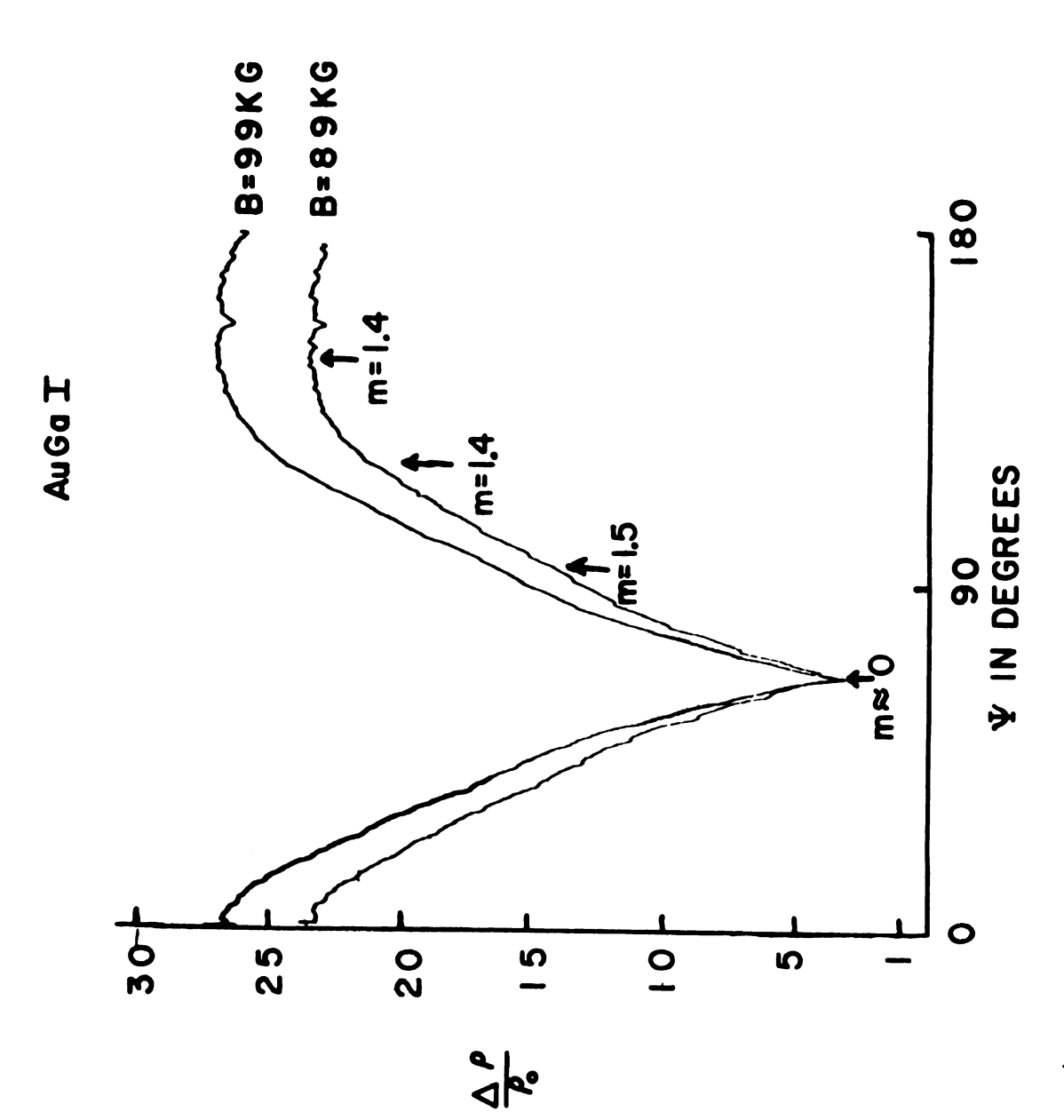


Figure 16.  $\Delta\rho/\rho_{o}$  vs.  $\psi$  for AuGaI.

that  $\frac{\Delta \rho}{\rho_0}$  = aB<sup>m</sup>, the exponent m was determined at various values of  $\psi$ . The value of m > 1 for all field directions except when B is in the [001] where  $\frac{\Delta \rho}{\rho_0}$  saturates. By tipping the crystal, i.e.,  $\phi \neq 0$ , the position of the sharp minimum could be followed and it occurred when B was in the (001). Figure 17 is a stereographic projection of AuGaI showing the major crystallographic planes and directions. The data shown in Figure 16 was taken with the sample rotated by 90° from its position in Figure 14.

Assuming that Au contributes one electron per atom and Ga 3 electrons per atom, then AuGa has 16 nearly free electrons per unit cell and AuGa should behave like a compensated compound. This is seen to be the case since m > 1 for most directions of the magnetic field. The saturation of the magnetoresistance when B is in the (001) is due to open orbits in the [001] since  $\frac{\Delta \rho}{\rho_0} \simeq aB^2 cos^2 \alpha$  when open orbits occur and  $\alpha$ , the angle between the current direction [010] and open orbit direction in k-space, is 90°. The small dip when B is in (100) will be discussed after data for AuGaII is given.

Figure 19 shows two rotation plots at different fields, 99 kG and 88 kG, for AuGaII which has current direction ~33° from [001]. The value of m is greater than 1 for all field directions with maximum value of 1.8. The interesting features of this data are the small peak when B is in (001) and the small dip when B is in (100).

Figure 20 shows rotation plots of AuGaII for various tip angles with the magnitude of B remaining constant. A

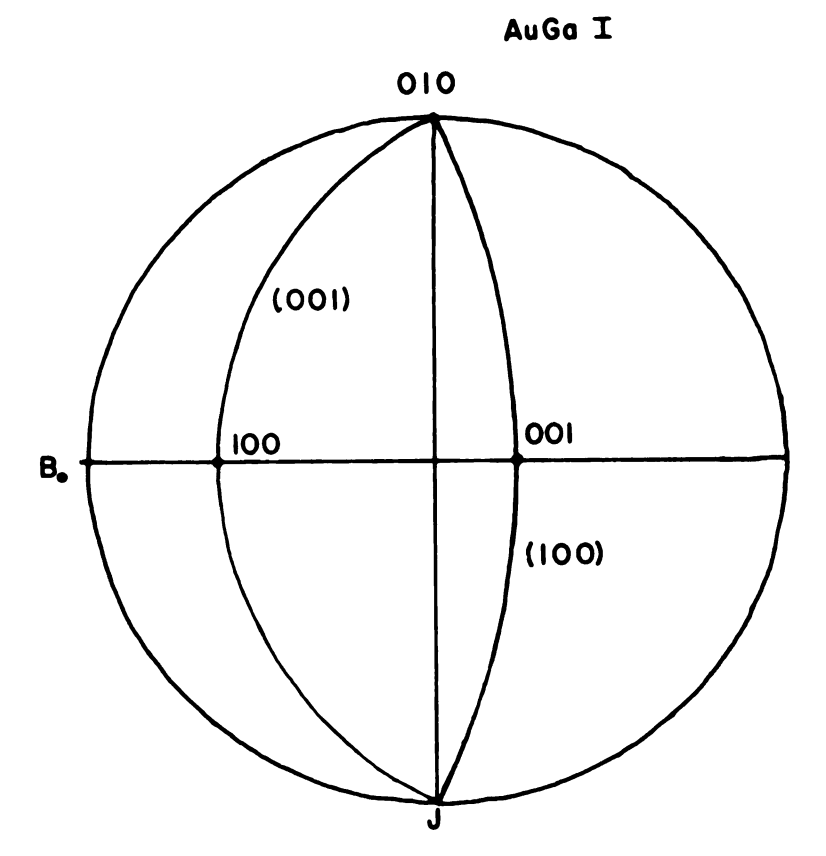


Figure 17. Stereographic projection of AuGaI.

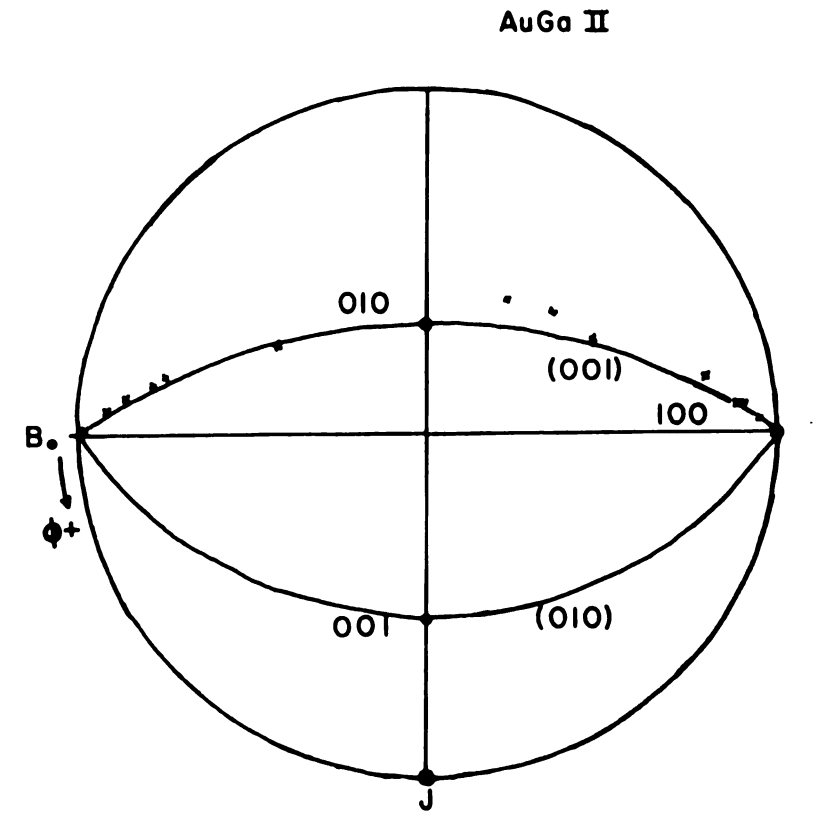


Figure 18. Stereographic projection of AuGaII. X's designate position of sharp peaks.

# AuGa 🎞

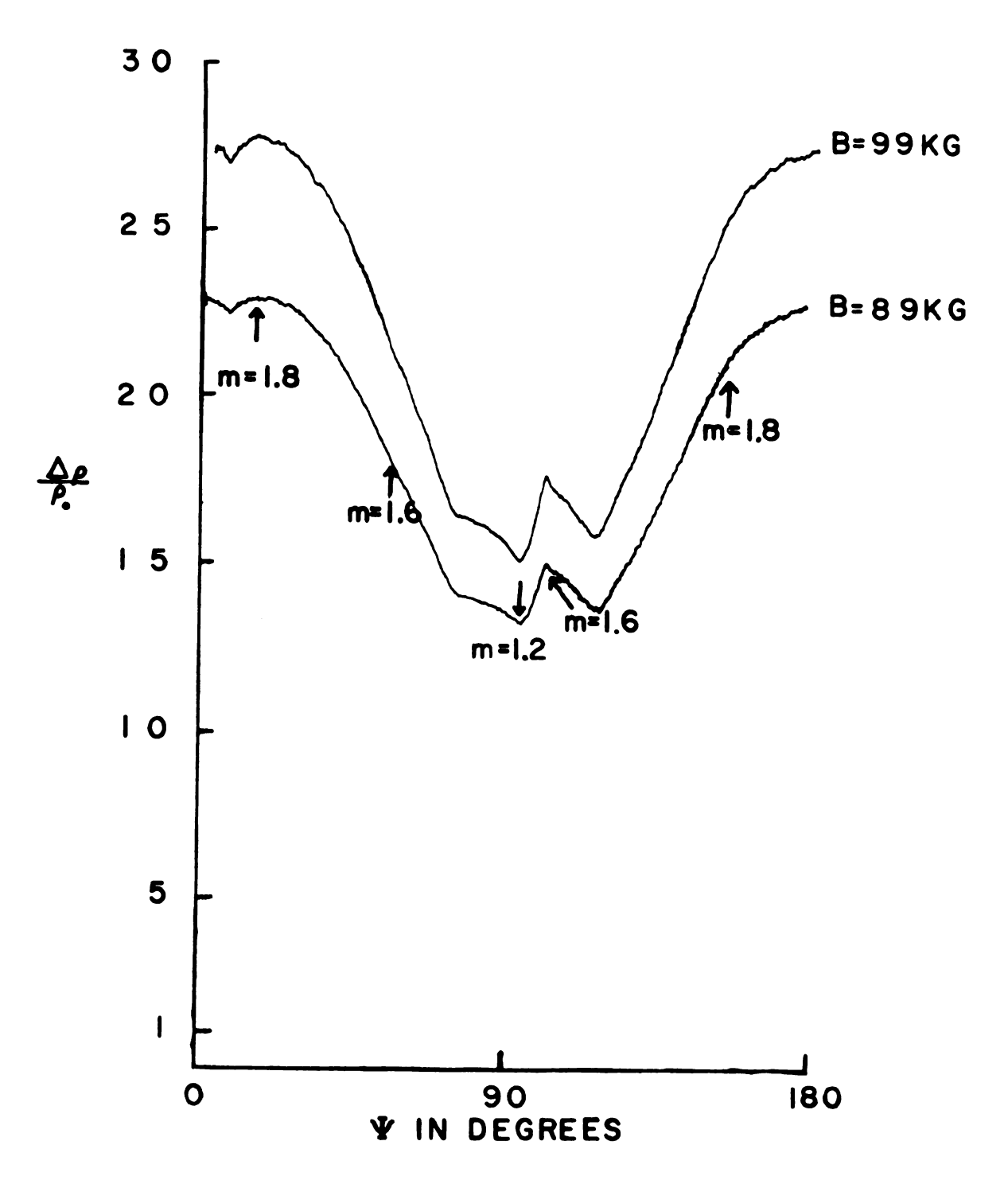


Figure 19.  $\Delta \rho / \rho_0$  vs.  $\psi$  for AuGaII.

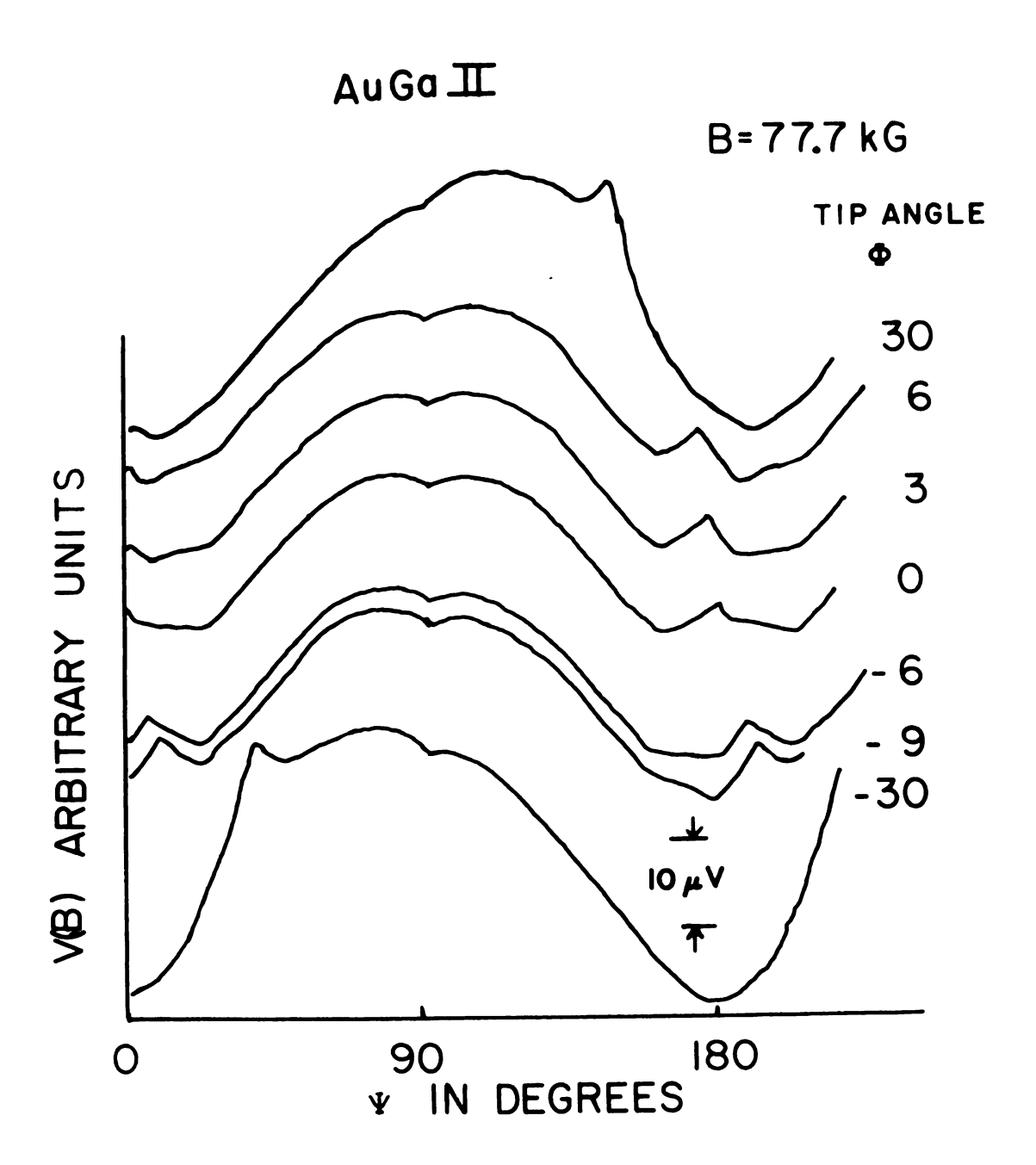


Figure 20. V(B) vs.  $\psi$  for different values of  $\phi$  for AuGaII.

stereographic projection which shows the positions of the small (x's) peaks for rotation plots at different tip angles is given in Figure 18. The peaks occur when B is in the (001) and they are due to open orbits in the [001]. Referring back to page 72 where a discussion of the tipping arrangement is given, when  $b_{01}^{O} \sin^2 \gamma > b_{C} (\cos \gamma + \sin \gamma)^2$  such a peak can occur.

The slight dip which occurs when B is in (100) for both AuGaI and II is probably due to a small number of electrons making open orbits due to magnetic breakdown. In both samples, the current direction makes an angle of 90° with respect to the [100] direction and thus the magnetoresistance should saturate if there are a significant number of open orbits. Since no saturation occurs, there are not a large number of open orbits excited. In addition, the dip is not observed until high fields are reached and the depth increases as the field increases; both effects suggest magnetic breakdown leading to a small number of open orbits.

AuGa is thus seen to be a compensated compound whose FS supports open orbits in the [001]. The open orbits extend for a complete 180° angular region. Other high symmetry directions such as [100], [110], and [101] do not support open orbits and the [010] direction could not be checked for open orbits because  $\alpha = 0$  for AuGaI and  $\alpha = 57^{\circ}$  for AuGaII. A sample with current direction of about 90° from [010] would be needed to check for open orbits in the [010].

A Harrison construction was done to determine if the NFE model agreed with the observed topology of the FS. A

computer program (46) written by J. Longo for Cl(CaF<sub>2</sub>) structures was adapted for AuGa. The program plots the intersection of the Fermi spheres which are centered on reciprocal lattice points with planes perpendicular to some specified field direction. By varying the height and direction of the planes, the FS can be determined.

A NFE model was used with 16 electron per unit cell which gave a  $k_f$  of 1.5 110 Å<sup>-1</sup>. The lattice parameters used were those determined by Jan<sup>(15)</sup> at liquid He temperature. Planes perpendicular to [100] and [001] were taken at .1 Å<sup>-1</sup> intervals. The height of the unit cell in these directions is about 1.00 Å<sup>-1</sup>. Table XI contains some important FS parameters for AuGa.

The FS in both directions is quite similar since the lattice constants differ by only 2%. The first three bands are completely occupied in these directions and there is FS in the 4th through 12th bands. The 4th, 5th, and 6th bands are comprised of small hole-like regions while the 7th band has large hole-like orbits. The 10th and 11th are electron-like and there is a very small electron-like region for the 12th band. The 8th and 9th bands are electron sheets and contain the open orbit regions. For B||[001] and B||[100] open orbits run in the [100] and [001] respectively for at least half of the Brillouin zone volume. Thus, the open orbits in the [001] are consistent with the experimental topology but the [100] directed open orbits are not.

The Harrison construction just discussed was done assuming

a single zone scheme. However, the B31 structure has glide planes and screw axes which introduce structure factors of zero value. The structure factor in x-ray diffraction is a geometric factor which depends on the positions of the atoms in the unit cell of the crystal. The structure factor S is given by

$$S(hkl) = \sum_{j} f_{j} \exp[-2\pi i (u_{j}h + v_{j}k + w_{j}l)]$$
 (34)

where  $f_j$  corresponds to the scattering power of the jth atom which is located at position [uvw] in the unit cell and hk $\ell$  are the Miller indices. The amplitude of the scattered x-rays is proportional to S\*S. Thus, if S=0, there is no reflection from the (hk $\ell$ ) plane. This is a very common occurrence in x-ray diffraction.

The potential energy of an electron in a periodic crystal can be written

$$V(\bar{r}) = \sum_{\ell} V_{a}(\bar{r} - \bar{\ell})$$

where  $\bar{\ell}$  is a lattice vector and  $V_a(\bar{r}-\bar{\ell})$  is the potential about an individual atomic site. Since

$$V(\bar{r}+\bar{\ell}) = V(\bar{r})$$

 $V(\bar{r})$  can be written as a Fourier series

$$V(\bar{r}) = \sum_{\bar{r}} Ve^{i\bar{G}\cdot\bar{r}}$$

where

$$V_G = \frac{1}{\Omega} \int V(\bar{r}) e^{-i\bar{G}\cdot\bar{r}} d\bar{r}$$

G is a reciprocal lattice vector.

In the case of a lattice with a basis

$$V(\bar{r}) = \sum_{\ell} \sum_{a} (\bar{r} - \bar{\ell} - \bar{b})$$
 (35)

where  $\bar{\mathbf{b}}$  is a vector from the origin of a unit cell to the atomic positions. The Fourier component  $V_G$  is obtained by inverting Equation (35)

$$V_{G} = \frac{1}{\Omega} \sum_{\ell} \sum_{b} V_{a}(\bar{r} - \bar{\ell} - \bar{b}) e^{-i\bar{G} \cdot \bar{r}} d\bar{r}$$

$$V_{G} = N \int V_{a}(\bar{r}) e^{-i\bar{G} \cdot \bar{r}} dr S_{G}$$
(36)

where  $S_G$  is the structure factor and is given by

$$S_{G} = \sum_{\bar{b}} e^{-i\bar{G}\cdot\bar{b}}$$
 (37)

This structure factor is proportional to the structure factor for x-ray diffraction and both terms result from the atomic positions within the unit cell.

As an electron approaches a Bragg plane in the reciprocal lattice it will be reflected if there is an energy gap across the plane. The energy gap is proportional to  $V_G$ . Thus, if  $S_G$  is zero,  $V_G$  is also zero and the electron doesn't undergo Bragg reflection. Such a condition leads to multiple zone schemes if the structure factor is equal to zero across an entire plane comprising a boundary of a Brillouin zone. The electrons cross the boundary as though it wasn't there since the energy difference across the plane is zero.

Structure factors of zero value do not ensure that the energy gap across a Bragg plane is zero since spin-orbit coupling and other relativistic effects can break the degeneracy in energy, especiably in the case of heavy metals. The most notable example of this is the work of Falicov and Cohen (47) who were able to explain the magnetoresistance data taken on Mg and Zn by calculating the energy gap across the (0001) plane of the Brillouin zone due to spin-orbit coupling.

Advanced group theory can give some information in the case of spin-orbit coupling. One can in principle determine whether or not a degeneracy is broken by spin-orbit coupling. However, the magnitude of the energy difference, if there is a difference, between bands cannot be calculated by group theoretical methods. Double groups are used and in the case of non-symmorphic space groups the application of the theory is not trivial.

Magnetic breakdown (MB) can cause a Brillouin zone to go from a single zone at low fields to a double zone at high fields since the electrons may have a high probability of crossing the Bragg plane if the gap is small and the magnetic field is large. The probability of an electron making such an interband transition is

$$P = e^{-B}c/B$$

where  $\mathbf{B}_{\mathbf{C}}$  is the critical field for magnetic breakdown and is given by

$$B_{c} = \frac{K \epsilon_{g}^{2} m_{H}^{2} c}{e \hbar \epsilon_{f}}$$

whe

gap

a f

dow

COI

hav

tu

(0)

tie [1

th pl

٧a

to th

CC

r;

đ

g;

Ŋ

where K is a numerical factor of order unity,  $\epsilon_g$  is the band gap,  $m_H$  is the cyclotron mass and  $\epsilon_f$  is the Fermi energy. In a field of B  $\approx$  100 kG there is appreciable magnetic breakdown if  $\epsilon_g$   $\approx$  0.1 eV (assuming  $\epsilon_f$   $\approx$  10 eV). Thus MB is a complicating factor.

In the case of AuGa there are seven wavevectors which have zero structure factor in the first octant and magnitude less than or nearly equal to 2 k<sub>f</sub>. They are [100], [010], [001], [110], [012], [300], and [003]. A Harrison construction was made assuming a double zone scheme in either the [100] or [010] direction. The open orbits remained for both the [100] and [001]. Thus a double zone scheme does not explain the data. It is possible that some combination of zero value structure factors gives a FS which has the correct topology but such a combination is very difficult to hypothesize and the Brillouin zone in such a case would be quite complicated.

To summarize, the FS of AuGa as constructed by the Harrison method assuming a NFE model with 16 electrons per unit cell does not give the correct topology of the experimentally determined FS. A double zone scheme assuming that the energy gap across the (010) or (001) is zero, also does not conform to the topology. Thus, the NFE model does not seem to work.

Jan et al<sup>(15)</sup> were also not able to fit their dHvA data to a NFE model.

## AuPb<sub>2</sub>

AuPb<sub>2</sub> has the Cl6 (CuAl<sub>2</sub>) structure which is body centered tetragonal with space group  $D_{4h}^{18}$  -I 4/mmm. The unit cell contains 6 atoms and Figure 21 shows the conventional cell of AuPb<sub>2</sub> which contains 12 atoms. The lattice constants (29) at room temperature are a = 7.325 Å and c = 5.655 Å which makes c/a = 0.772.

Figure 22 shows how the magnitude and definition of the transverse magnetoresistance voltage across the sample changes with the strength of the magnetic field. The upper most curve was taken with the Keithley 147 on the 10  $\mu$ V range while the remaining curves were taken on the 30  $\mu$ V range. As the field increases and more of the electrons enter the high field region, the sharpness of the dips increases as does the height of the maxima. The signals are much easier to interpret in the high field (-80 - 100 kG) range and these graphs show the advantage of using such fields.

Figure 23 to Figure 27 show the field dependence of the transverse ( $\phi$  = 0) MR at various values of  $\psi$ . The quantity m is calculated from  $\frac{\Delta \rho}{\rho_0}$  =  $aB^m$ . The value of m is seen to be greater than 1 for most field directions and these directions are general directions, i.e., not parallel to a major crystal axis or direction and not in a major crystallographic plane. Also, the sharp dips, as will be explained later, occur when B is in a major crystallographic plane. Such behavior of the MR means that AuPb<sub>2</sub> is a compensated compound

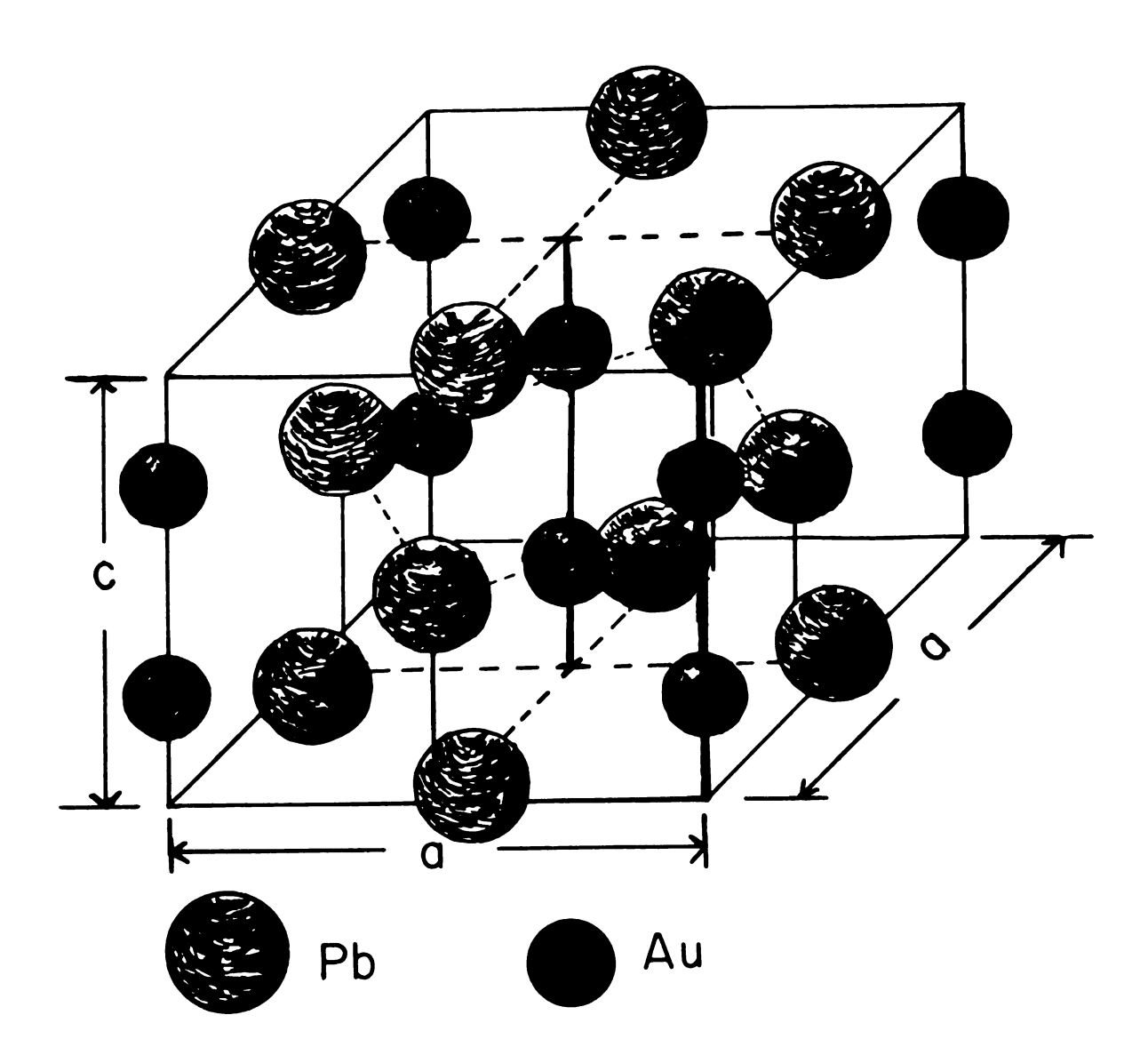


Figure 21. Conventional cell of AuPb<sub>2</sub>.

## STINU YAAATIBAA (8)V

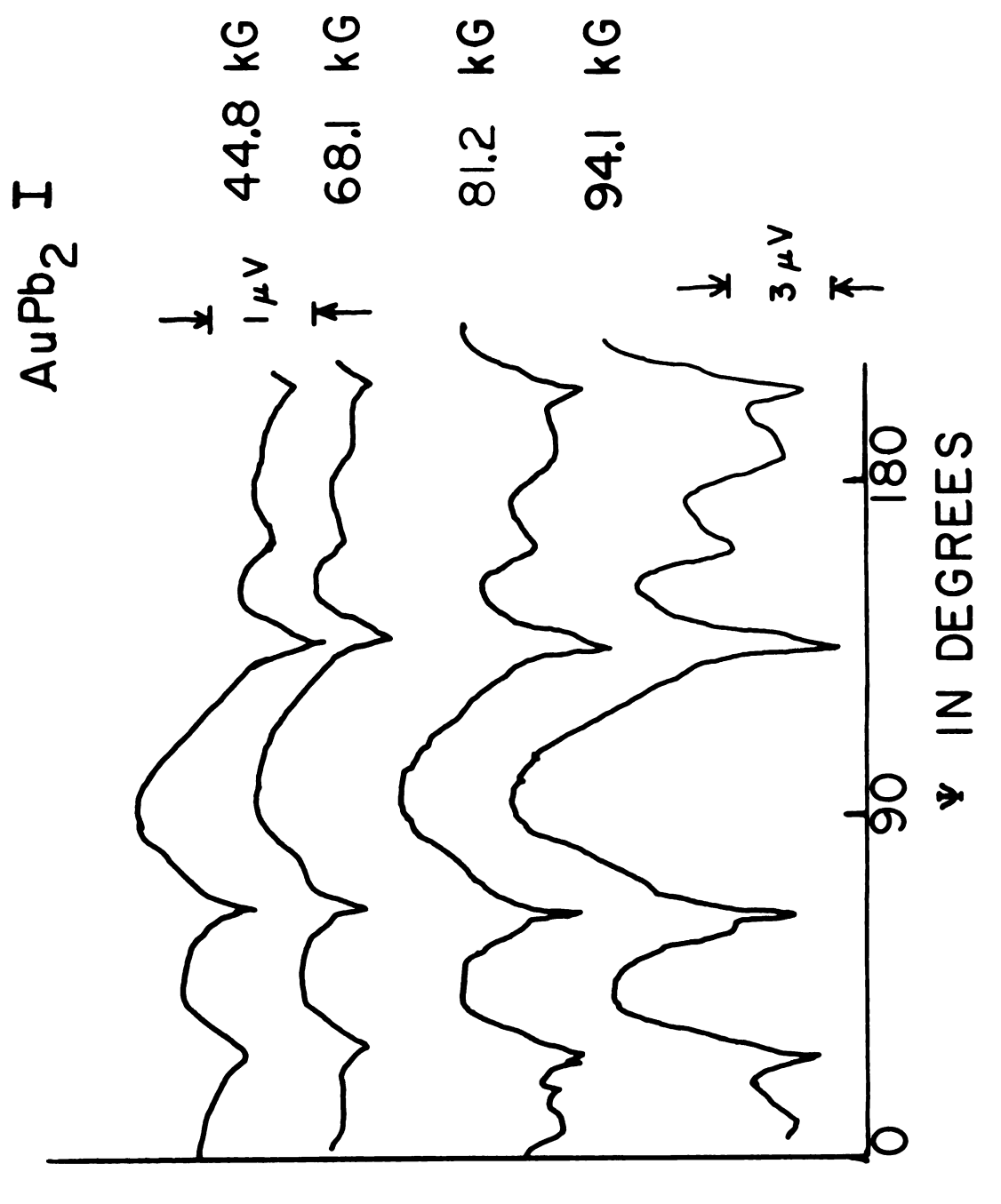


Figure 22. V(B) vs.  $\psi$  for various values of B for AuPb $_2$ I.

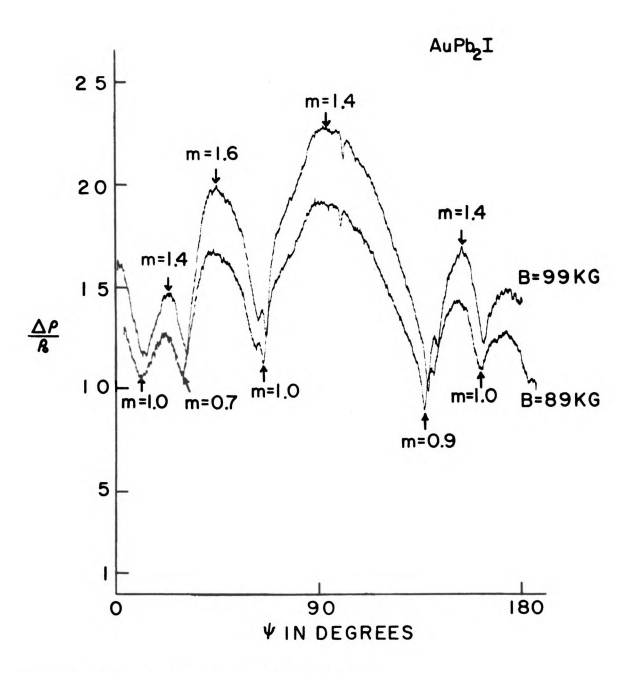


Figure 23.  $\Delta \rho / \rho_0$  vs.  $\psi$  for  $AuPb_2I$ .

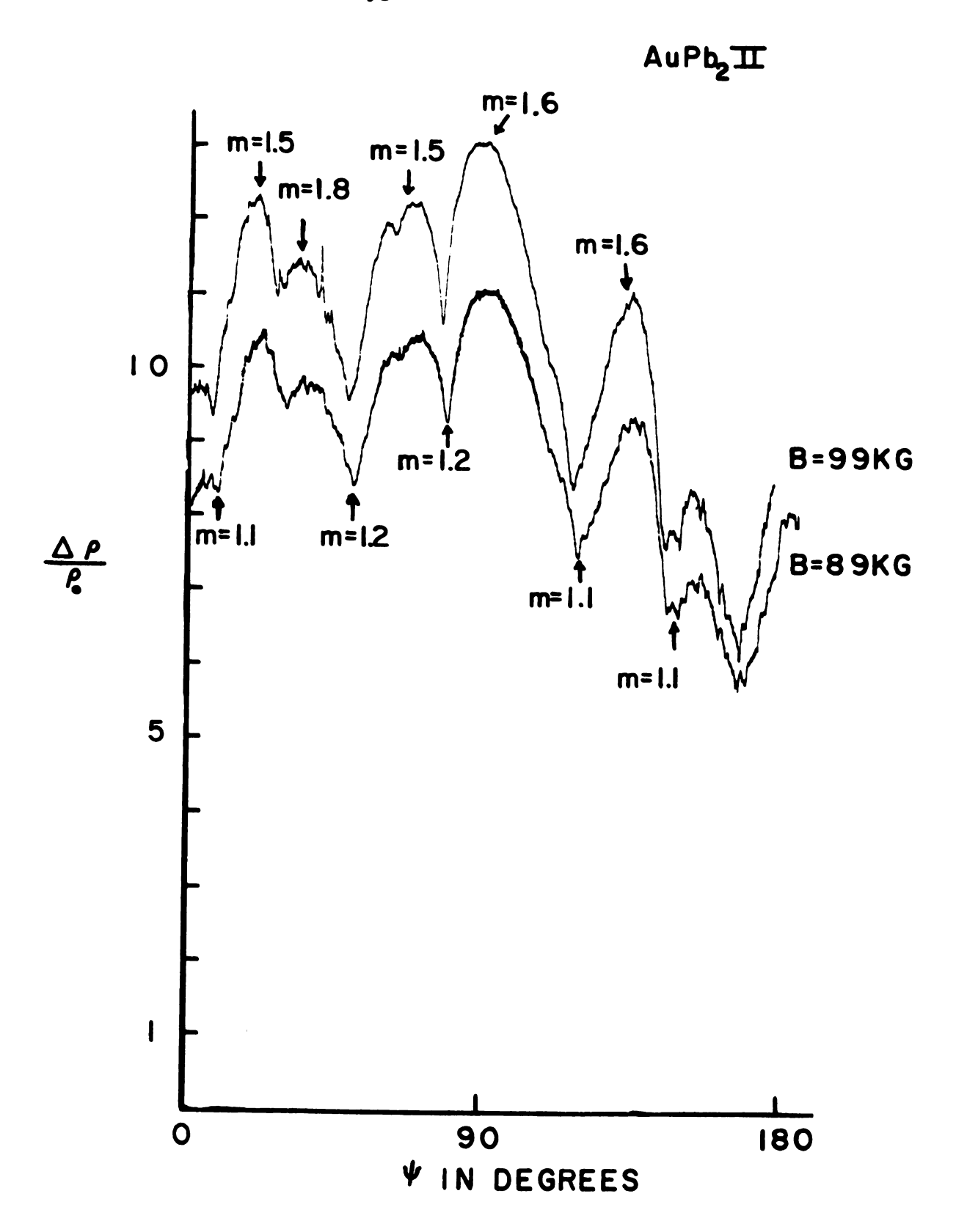


Figure 24.  $\Delta \rho / \rho_0$  vs.  $\psi$  for  $AuPb_2II$ .

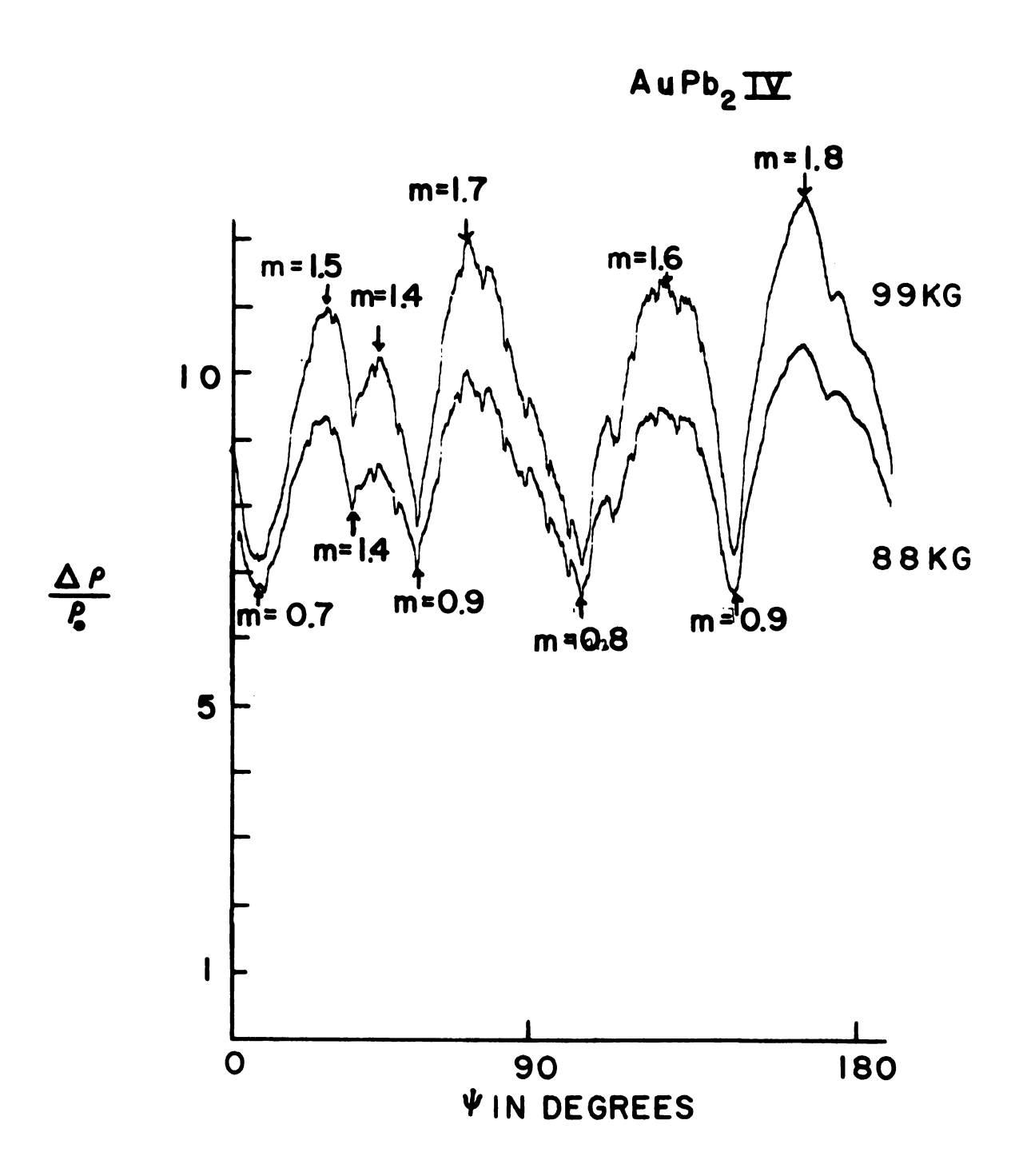


Figure 25.  $\Delta \rho / \rho_0$  vs.  $\psi$  for AuPb<sub>2</sub>IV.

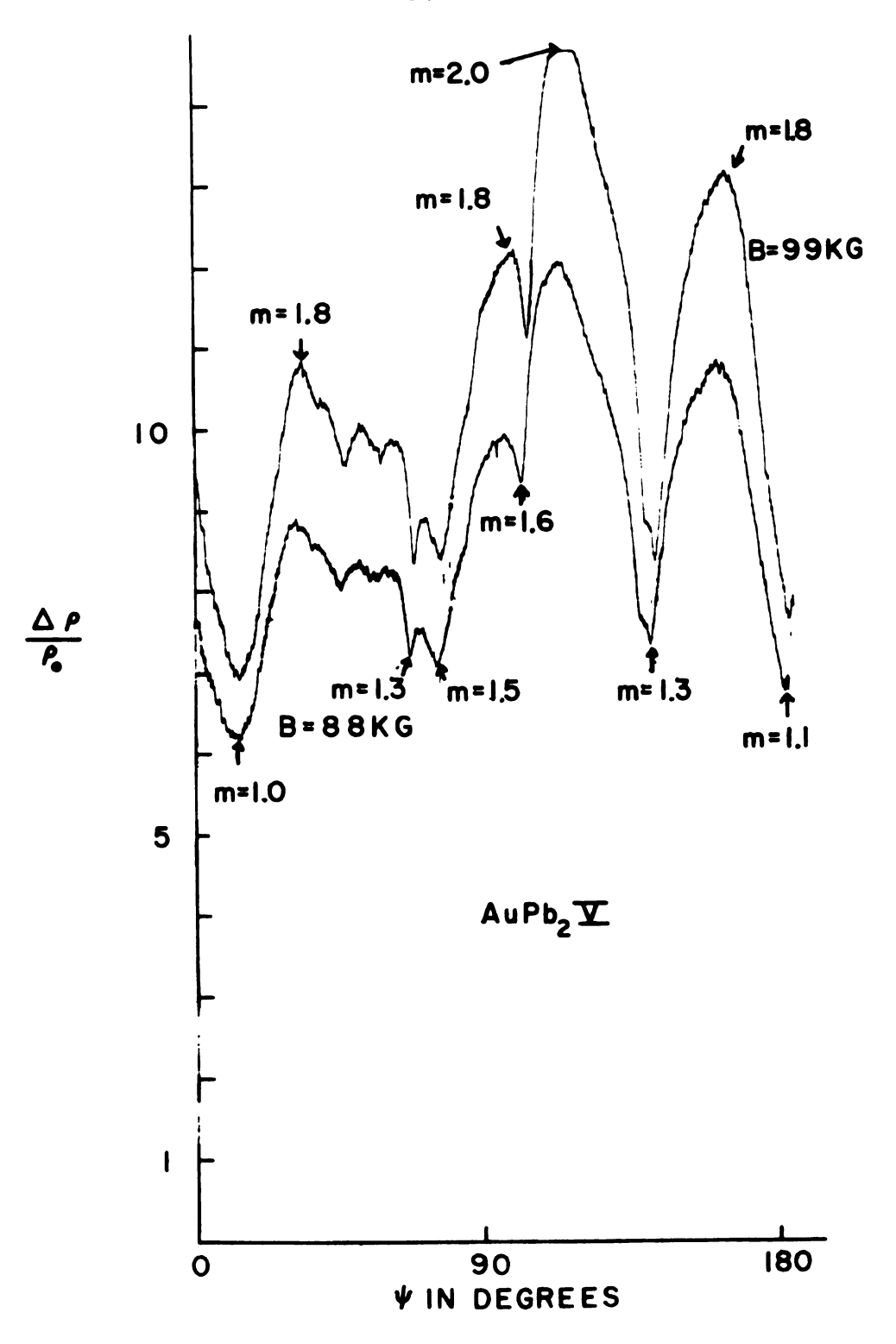


Figure 26.  $\Lambda \rho / \rho_0$  vs.  $\psi$  for  $\Lambda u Pb_2^V$ .



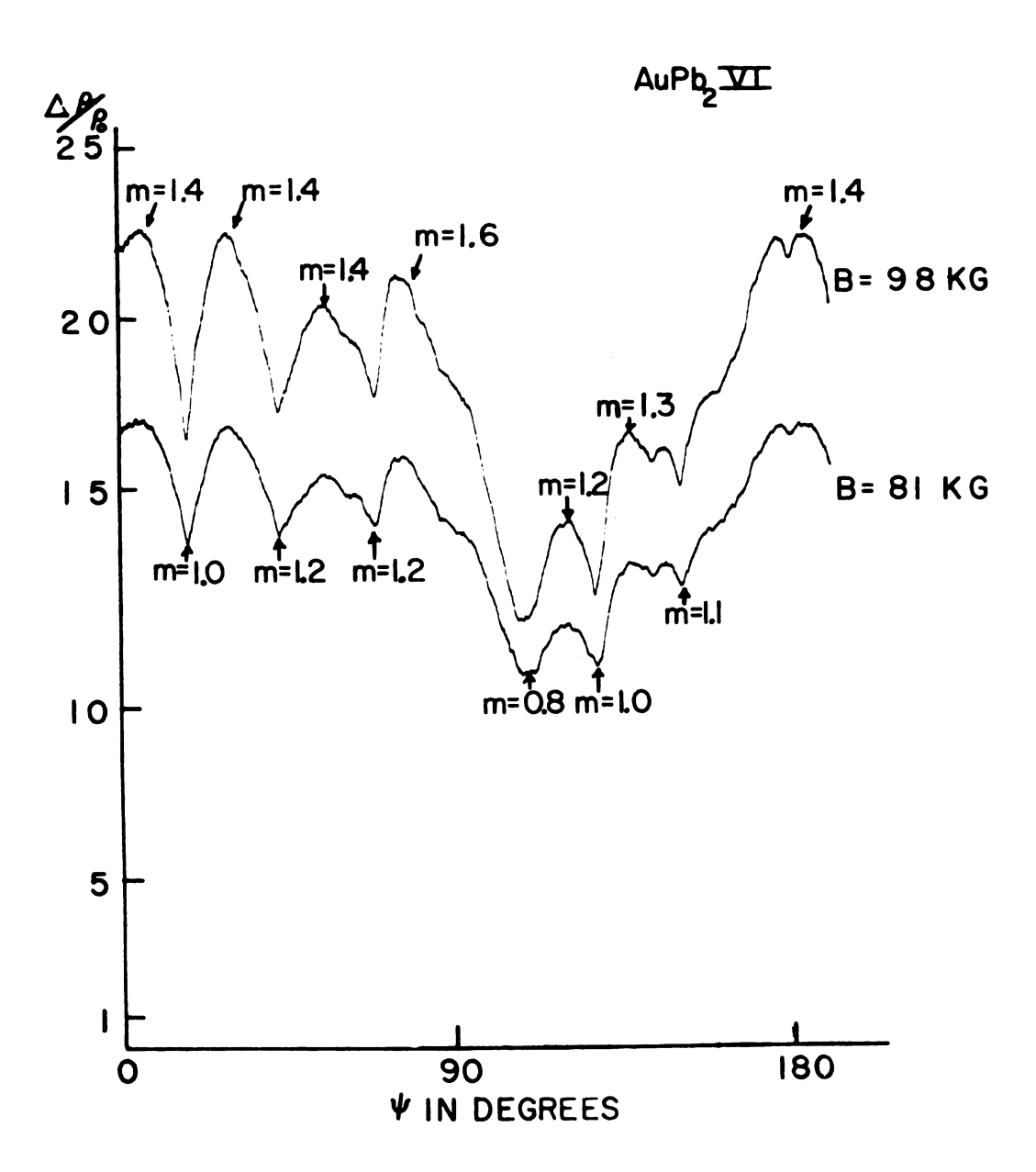


Figure 27.  $\Delta \rho / \rho_0$  vs.  $\psi$  for  $AuPb_2^{VI}$ .

which has a FS which supports open orbits.

In order to determine the directions of the open orbits, the samples were tipped with respect to their initial transverse positions through various angles ( $\phi$ ) as was explained previously. A stereographic projection was used to plot the position of the minima as the sample was tipped and then rotated through 180°.

Figure 28 shows the MR data for various tip angles. The negative sign for the tip angle  $_{\phi}$  means that the magnetic field moves clockwise with respect to the sample. Figure 29 is a stereographic projection of all the minima observed for AuPb<sub>2</sub>I. The dash lines show the motion of the magnetic field with respect to the crystal axis. The small x's are the position of the minima. The appropriate minima are connected together to form a plane and the direction of the open Orbit in k-space is found normal to that plane.

Figures 30 and 31 show the stereographic projections for the other four crystals. The dashed lines have been omitted except for the  $\phi = 0^{\circ}$  and 90° lines. The position of the dips in the Figures 23 to 27 can be followed in these stereographic Projections with the following changes: for  $AuPb_2II$ ,  $AuPb_2IV$  and  $AuPb_2V$  start at the right hand side of the figure,  $180^{\circ}$  from  $B_0$  and go toward  $B_0$  along the  $\phi = 0$  line. For  $AuPb_2I$  and  $AuPb_2VI$  the starting point is  $B_0$ , which is the usual manner of Plotting the data. The reasons for the exception is that the data shown in Figures 24, 25, 26 was taken with the samples mounted  $180^{\circ}$  from the position used in taking data for the stereographic projections, Figures 28 and 29.

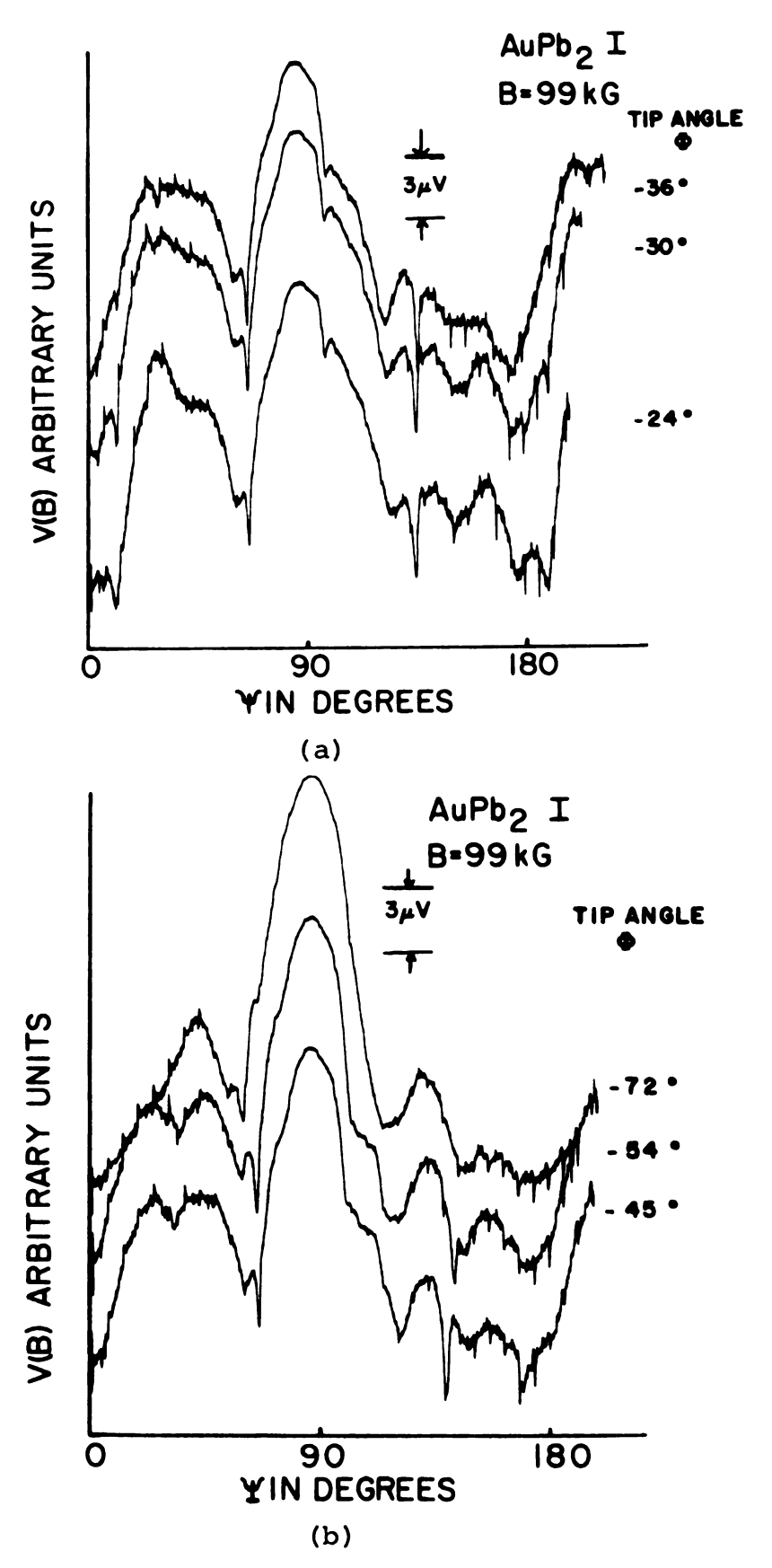


Figure 28. V(B) vs.  $\psi$  for various values of  $\phi$  for  $AuPb_2I$ .

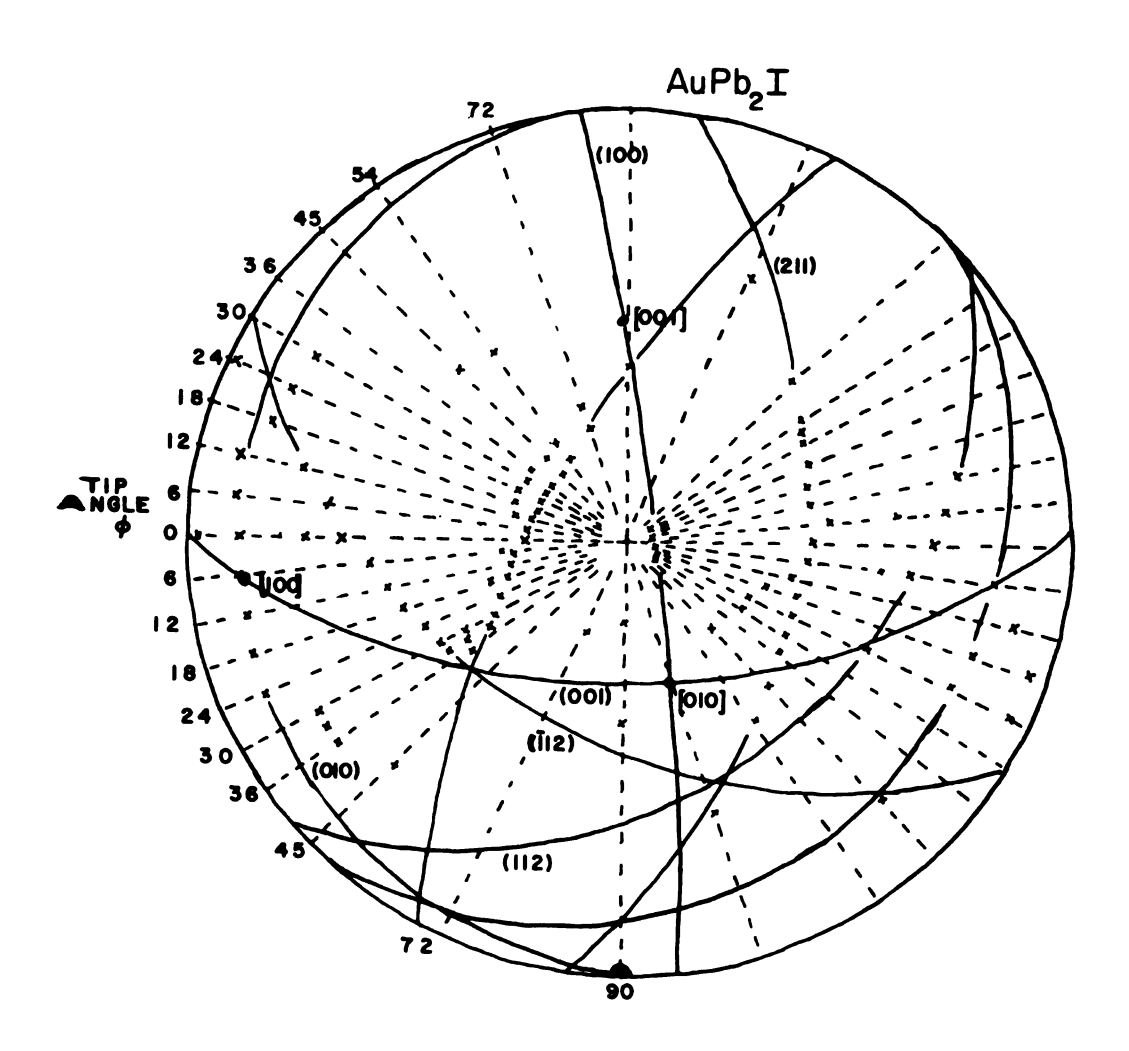


Figure 29. Stereographic projection showing minima for  $\texttt{LuPb}_2 \mathbf{I}$ .

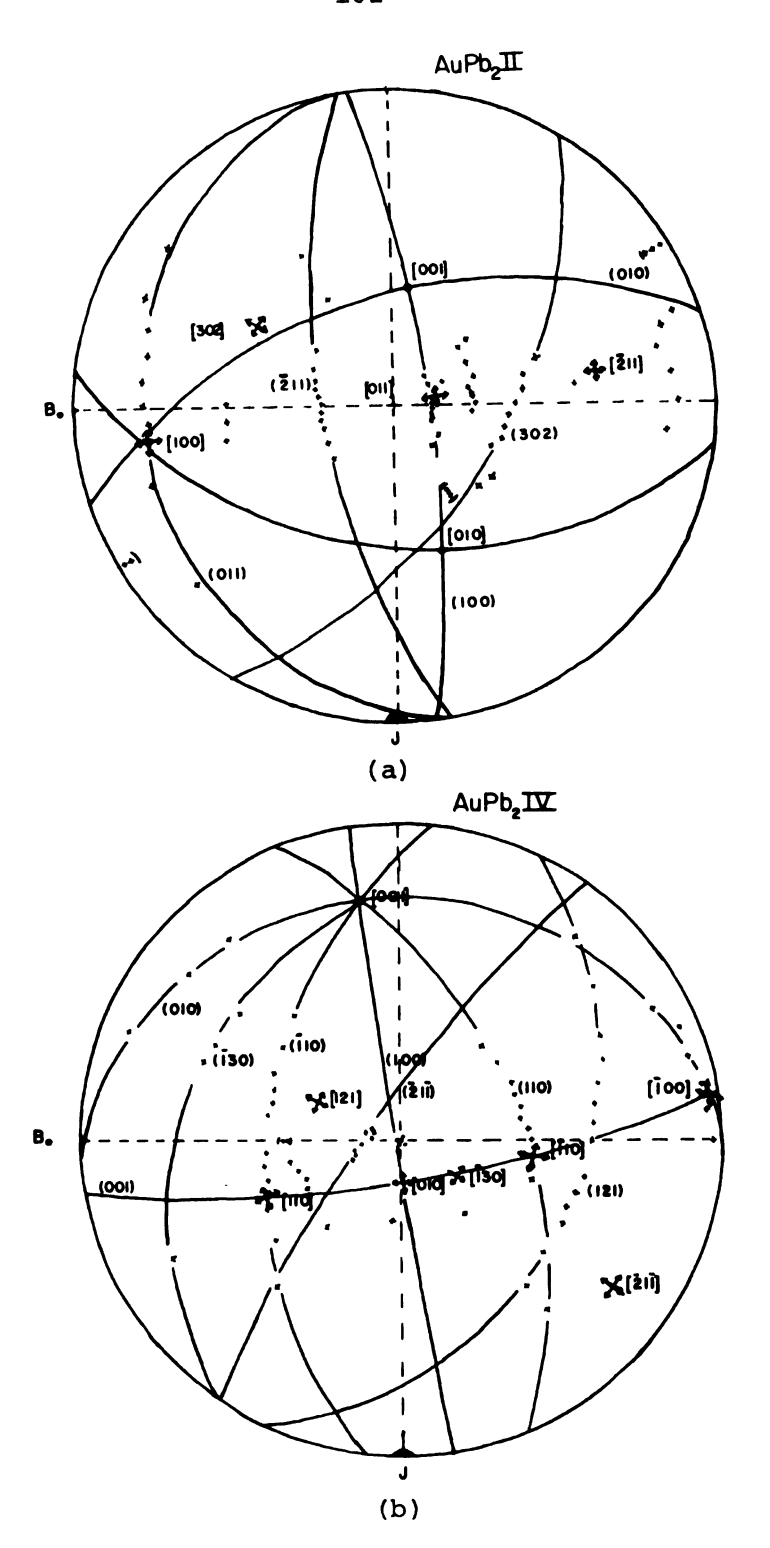


Figure 30. Stereographic projection of HFMR results for (a) AuPb<sub>2</sub>II and (b) AuPb<sub>2</sub>IV.



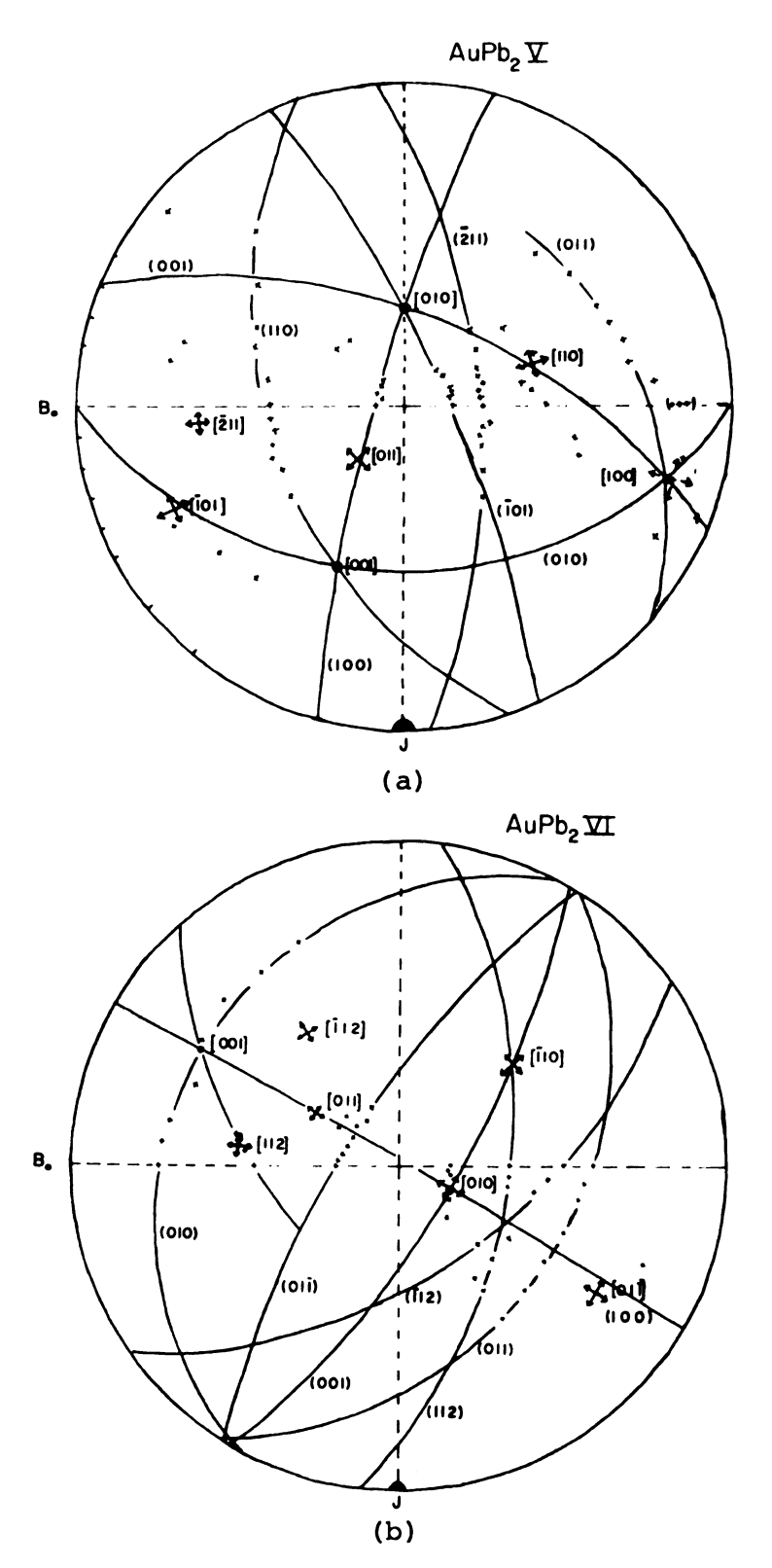


Figure 31. Stereographic projection of HFMR results for (a) AuPb<sub>2</sub>V and (b) AuPb<sub>2</sub>VI.

The directions of the open orbits are indicated by  $\upolinimal{N}$  on the stereograms. The symbol (xxx) indicates a broad minimum. Table XII summarizes the directions of the open orbits found in the five samples. Note that there are many open orbit directions and that some open orbits are seen in some samples but not others. The reason for this is the  $\cos^2\alpha$  factor in the HFMR which may obscure open orbits in compensated materials unless  $\alpha$  is close to 90°. However, some open orbits still show up when  $\alpha$  is as small as 45°, see column 2 of Table XII.

The major directions supporting open orbits are the <100>, <101>, <110>, <112> and <211>. The [001] could not be adequately tested for open orbits since a was generally too small, the largest value being 60° for AuPb2VI. A stereographic projection showing the major open orbit directions, their corresponding planes, and the current directions of the samples tested is shown in Figure 32. The <100>, <112>, <211>, and <101> open orbits occur whenever B is anywhere in the corresponding planes. The <110> open orbits could not be entirely tested to see if the open orbits result when B was at any position in the {110}. There was a dip in the MR for B in the {110} up until 20° from [001] but experimental limitation prohibited investigation of the remaining 20°.

The Bravais lattice of AuPb<sub>2</sub> is body centered tetragonal and a primitive cell can be generated by the following vectors,

Table XII. Open Orbit Direction in AuPb<sub>2</sub>

Direction*	Angle Between Open Orbit	Current and Direction	Sample
[100]	80		I
[112]	54		
[112]	63		
[211]	88		
[021]	84		
[441]	65		
[100]	78		II
[011]	87		
[211]	83		
[302]	57		
[010]	<b>7</b> 5		IV
[100]	81		
[110]	73		
[110]	86		
[121]	78		
[211]	56		
[130]	77		
[100]	<b>7</b> 5		V
[110]	77		
[011]	73		
[101]	66		
[211]	86		

Table XII (cont'd.)

Direction*	Angle Between Open Orbit	Sample
[010]	83	VI
[110]	60	
[011]	73	
[01]]	59	
[112]	86	
[112]	45	

<sup>\*</sup>Direction in reciprocal or k-space.

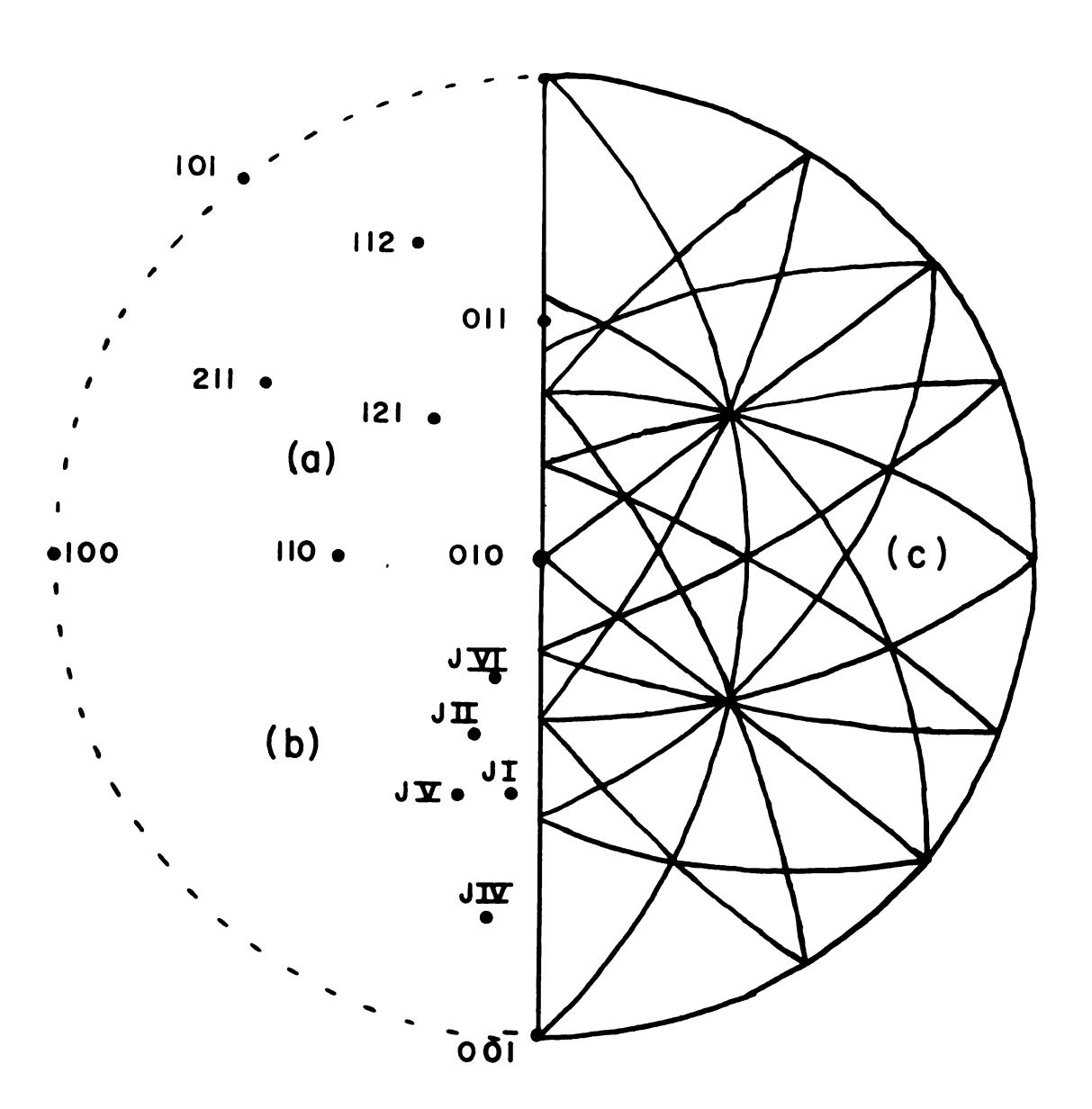


Figure 32. Stereogram showing (a) open orbit directions, (b) current directions, J, of samples and (c) planes corresponding to open orbit directions.

$$\bar{t}_{1} = \frac{a}{2} (\hat{i} + \hat{j}) + \frac{c}{2} \hat{k}$$

$$\bar{t}_{2} = \frac{a}{2} (\hat{i} + \hat{j}) - \frac{c}{2} \hat{k}$$

$$\bar{t}_{3} = \frac{a}{2} (\hat{i} - \hat{j}) - \frac{c}{2} \hat{k}$$

The reciprocal lattice vectors are

$$\bar{R}_1 = -2\pi \left(\frac{\hat{i}}{a} + \frac{\hat{k}}{c}\right)$$

$$\bar{R}_2 = 2\pi \left(\frac{-\hat{j}}{a} + \frac{\hat{k}}{c}\right)$$

$$\bar{R}_3 = \frac{2\pi}{a} \left(-\hat{i} + \hat{j}\right)$$

The reciprocal lattice is also body centered tetragonal but the square base of the reciprocal lattice is rotated by 45° about the c axis; Figure 33 shows the situation.

The Brillouin zone is constructed by taking the reciprocal lattice vectors and bisecting them with planes. The faces of the zone are formed by the planes which are closest to the origin in the direction under consideration. Figure 34 shows the Brillouin zone for  $\text{AuPb}_2$ . Note that the <110> and <101> in the reciprocal lattice are perpendicular to the zone faces but the <100> and <001> are not. The maximum height of the zone in the [001] is .887Å<sup>-1</sup> as compared to 1.111 Å<sup>-1</sup> which is  $\frac{\text{C}^*}{2}$  and thus reciprocal space is filled by placing the zones next to each other in the <110> in the  $\text{K}_{_{Z}}$  direction.

In constructing a topological model for the open orbits using cylinders which have their axes along the open orbit

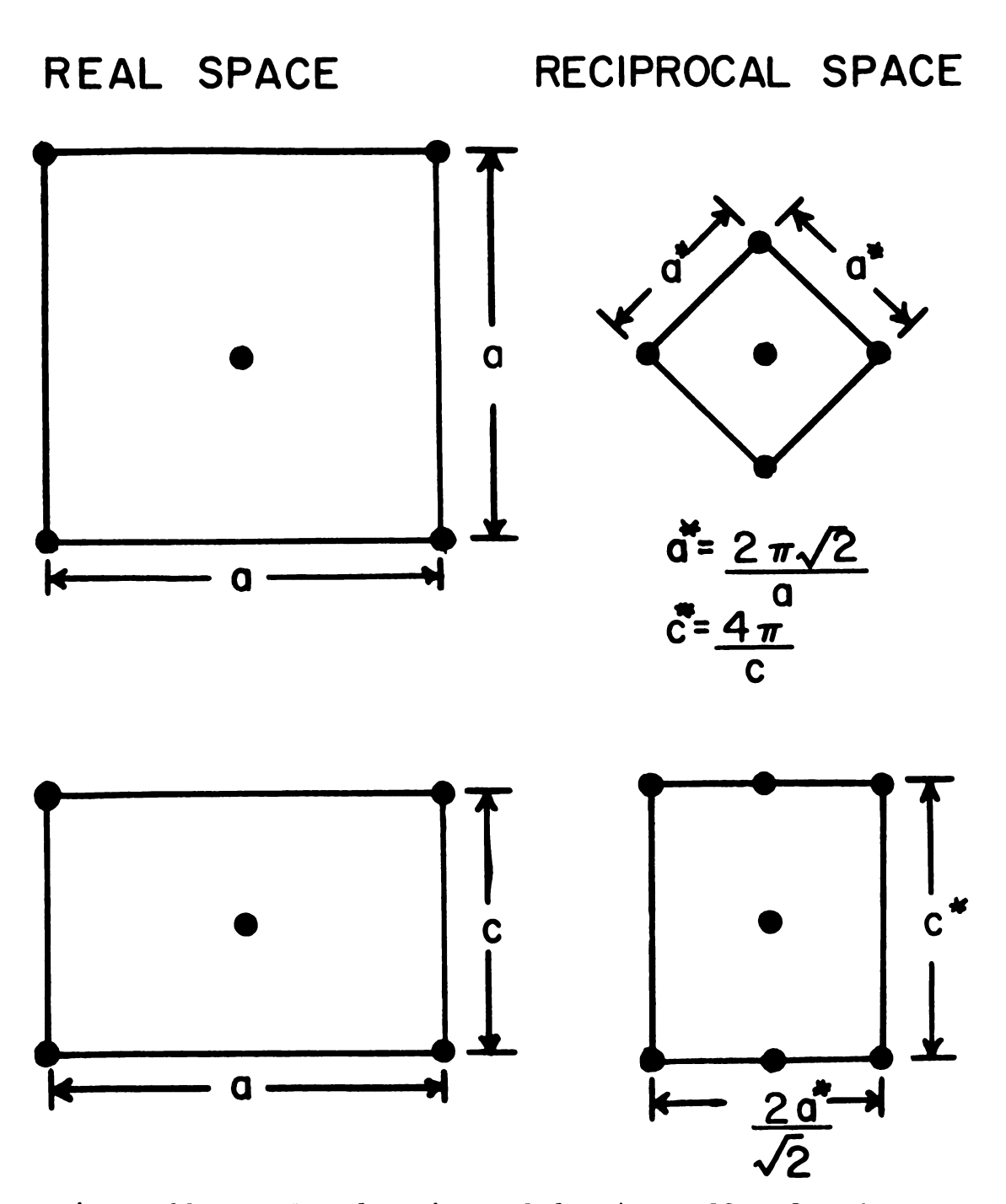


Figure 33. Real and reciprocal lattice cells of AuPb2.

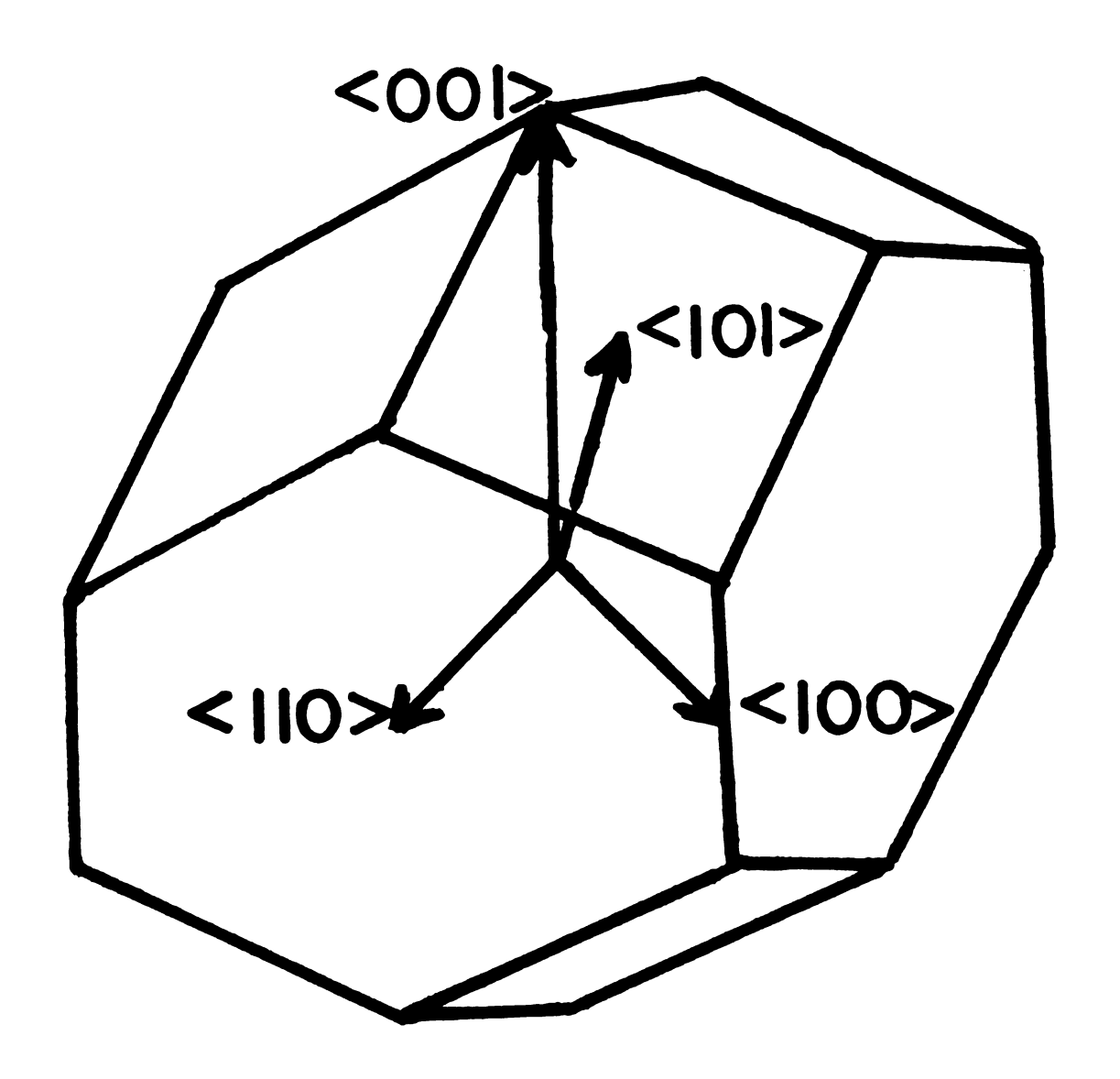


Figure 34. Brillouin zone of  $AuPb_2$ . Vectors correspond to directions in k-space.

direction, it is evident that the cylinder axes should be perpendicular to the Brillouin zone faces. This ensures that the open orbits are periodic and continue uninterrupted indefinitely when viewed in the periodically repeated zone scheme. The obvious choice of cylinder directions consistent with the experimentally determined FS topology are the <110> and <101>. There can be no cylinders in other directions which are perpendicular to zone faces.

The maximum possible diameter of the cylinder was calculated to be .97 Å<sup>-1</sup> for the <110> cylinders. The <100> open orbits can be generated by the <110> cylinders. If B is taken to be in the (100), the planes ⊥B cut the <110> cylinder making an angle of 45° with the <110>. If the diameter of the cylinders is large enough, there will be no gap of unfilled space as one goes from the intersection of one cylinder with the plane ⊥B to the other intersection and thus a band of open orbits is generated in the [100], see Figure 35. The <112> open orbits can be generated by the <101> cylinders. If the electron first moves along the [101] cylinder and then changes to a [011] cylinder in the next zone and then back to the [101] cylinder and so on, the net motion is in the [112]. The <211> open orbits can be produced by alternate use of the <110> and <101> cylinders.

A check was made to see if the NFE model gave results consistent with the experimentally determined FS topology. The Harrison construction program mentioned previously was worked out for AuPb, using the room temperature lattice

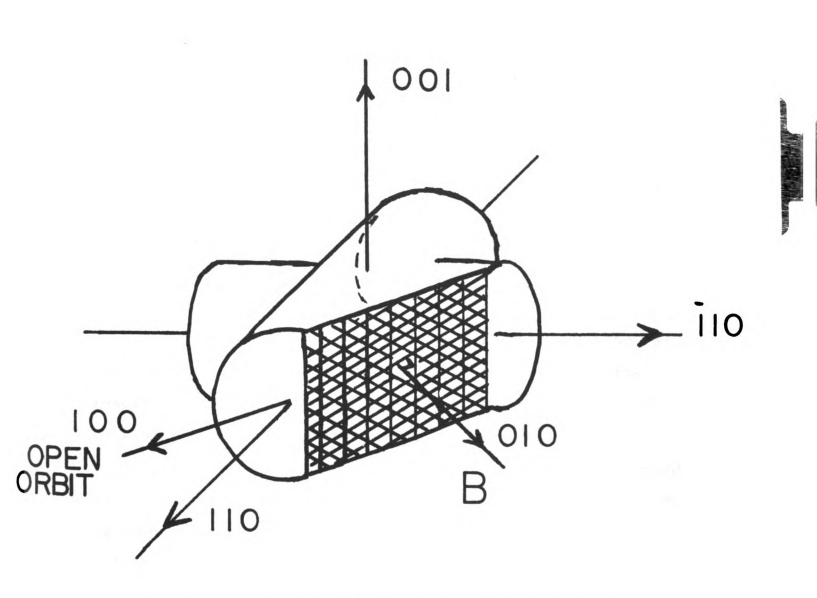


Figure 35. <110> cylinders generating <100> open orbits.

parameters and assuming 18 electrons per unit cell. A single zone scheme was used although there are glide planes and screw axes for this structure which mean many zero valued structure factors.

The results obtained by the construction were consistent with the experimental data. For B parallel to [ $\overline{1}10$ ] open orbits running in the [110] were found in the tenth band for Z = 0 to  $Z \approx .15 \text{ Å}^{-1}$ . Also, for B 55° from [ $\overline{1}10$ ] but still in the (110), open orbits were found in the tenth band running in the [110]. For B in (010) and perpendicular to the [101], open orbits were found in the ninth band from Z = .3 to  $Z \approx .45 \text{ Å}^{-1}$ .

AuPb<sub>2</sub> cannot yet be said to be NFE-like since these results were only for a few field directions. However, the results are encouraging and once the dHvA measurements are obtained, the NFE model can be tested thoroughly.

To summarize: AuPb<sub>2</sub> is a compensated compound in accordance with its even number of electrons per unit cell. The FS is open, supporting open orbits in the <100>, <110>, <101>, <112>, <211> and other higher order planes. The Brillouin zone geometry allows cylinders of open orbits in the <110> and <101> and these cylinders seem capable of explaining the occurrence of all the major open orbits observed. The NFE model constructed in a few high symmetry directions is consistent with the <110> and <101> directed open orbits.

## Au,Pb

Au<sub>2</sub>Pb has the C15 (MgCu<sub>2</sub>) structure which is face centered cubic with space group 0<sup>7</sup><sub>h</sub> - Fd3m. There are 6 atoms per unit cell. Figure 36 shows the conventional cell with 24 atoms. The lattice constant is ~7.93 Å as reported by Hansen. (31) There has been some controversy about the stability and crystal structure of Au<sub>2</sub>Pb. Hansen (31) states that data concerning the cold working of Au<sub>2</sub>Pb "indicates that Au<sub>2</sub>Pb is unstable below some unknown temperature." Our Laue x-ray photographs taken after the crystals have been cycled between room temperature and 4.2°K are identical. Also, photographs of the same samples taken many months apart are identical although the surface of the samples tarnish after a couple of days and must be repolished in order to obtain good photographs.

Figures 37 and 38 show how the MR signal increases with the magnitude of the magnetic field B for two of the samples tested. The top curve in Figure 37 (B = 21.7 kG) was taken with the Keithley 147 on the 30  $\mu$ V range while the other data was taken on the 100  $\mu$ V range. Figures 39 to 43 show plots of the HFMR for the remaining samples tested and give the value of the coefficient m at various points. The data, especially the data for Au<sub>2</sub>PbIIb which has the highest RRR, indicate that the FS of Au<sub>2</sub>Pb supports open orbits.

The fact that the FS supports open orbits is most clearly demonstrated by Figure 40. The field dependence of the

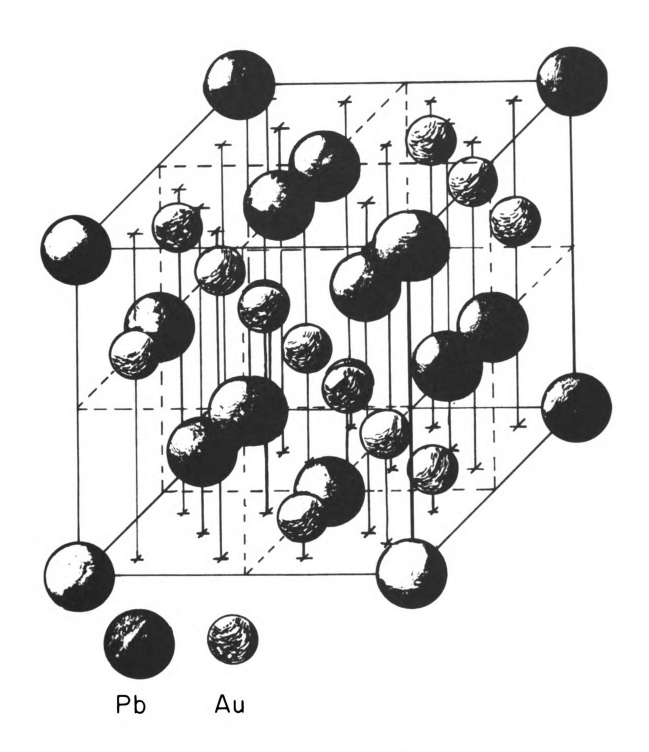


Figure 36. Conventional cell of  $\mathrm{Au_2^{Pb}}$ .

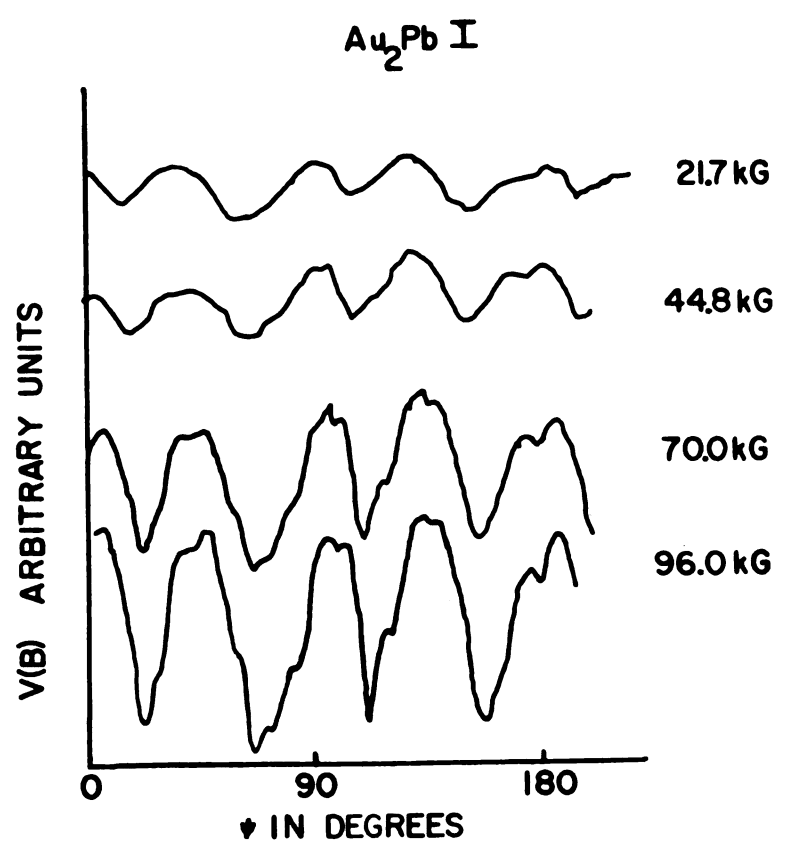


Figure 37. V(B) vs.  $\psi$  for various values of B for Au<sub>2</sub>PbI



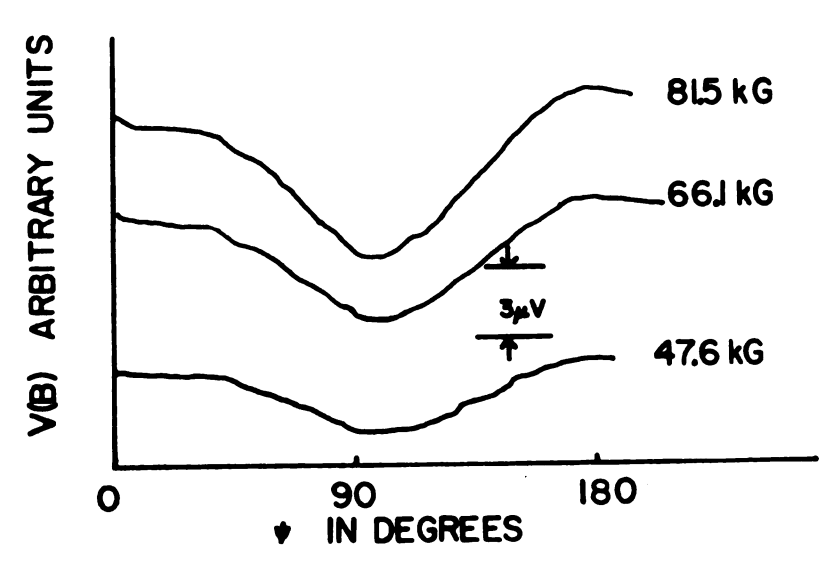


Figure 38. V(B) vs.  $\psi$  for various values of B for Au<sub>2</sub>PbII.

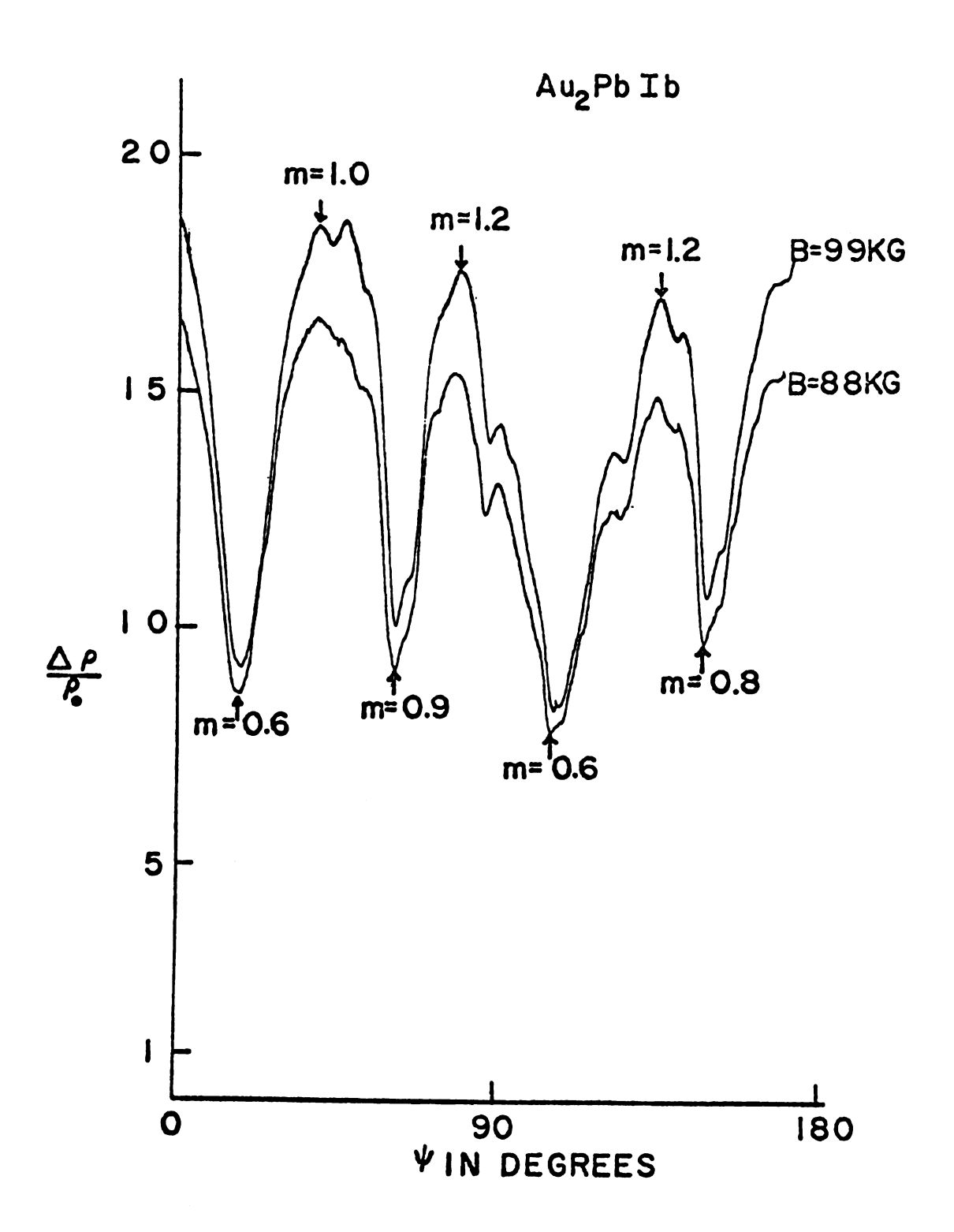


Figure 39.  $\Delta \rho / \rho_0$  vs.  $\psi$  for  $Au_2$ PbI.

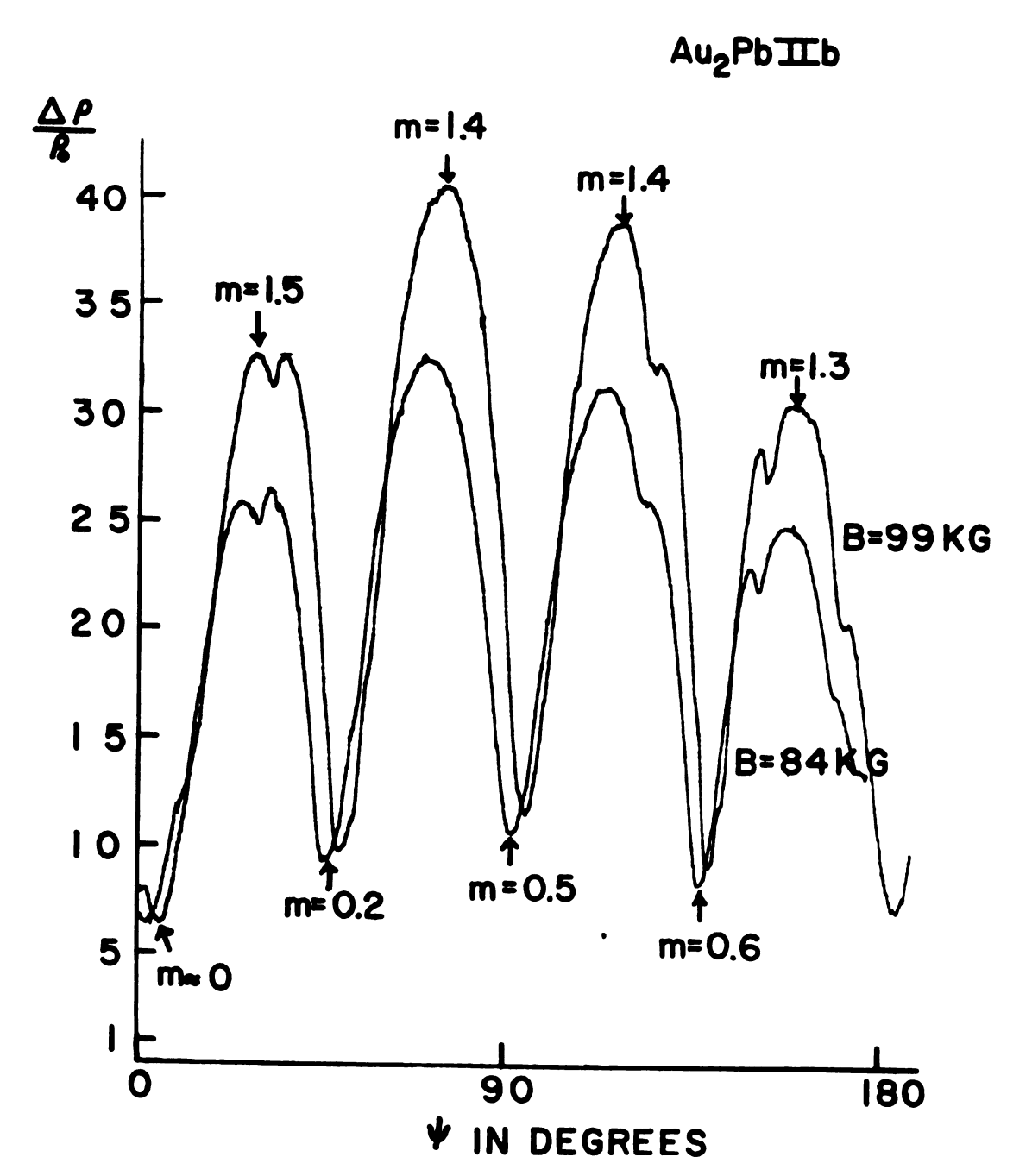


Figure 40.  $\Delta \rho / \rho_0$  vs.  $\psi$  for  $Au_2$ PbIIb.

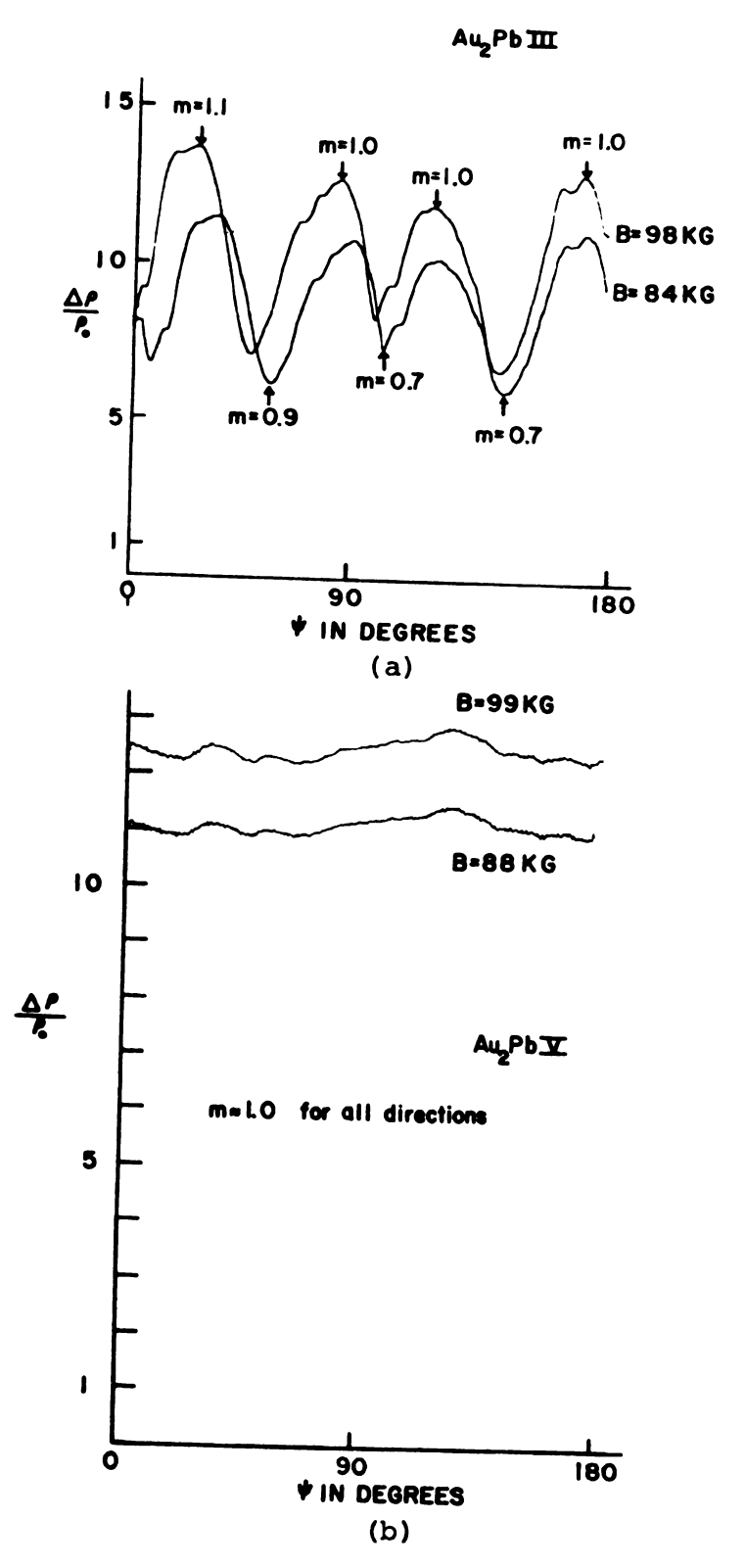


Figure 41.  $\Delta \rho / \rho_0$  vs.  $\psi$  for (a)  $\Delta u_2 PbIII$  and (b)  $\Delta u_2 PbV$ .

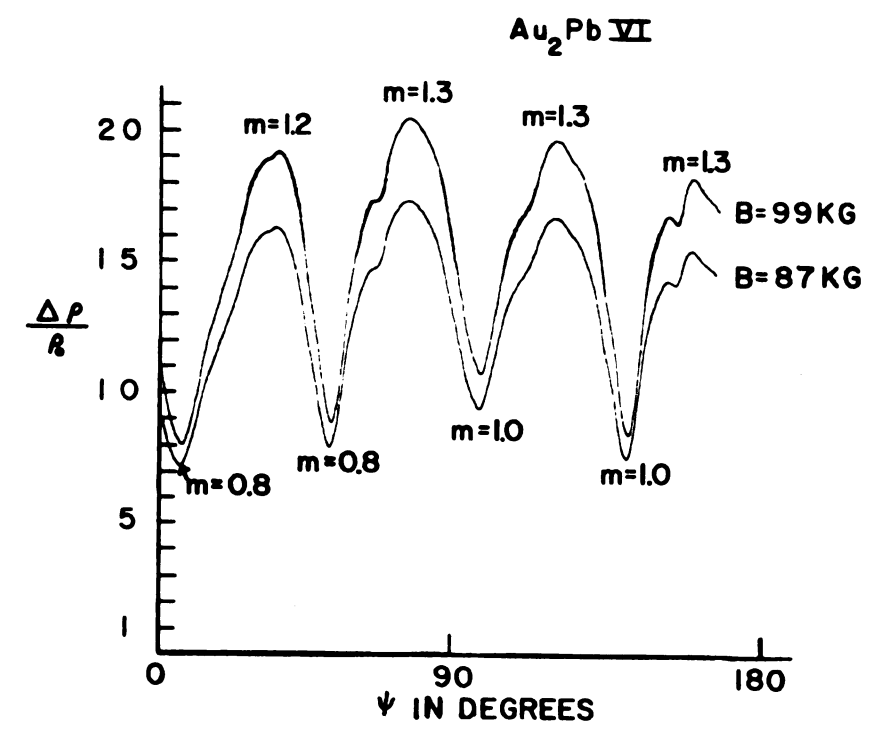


Figure 42.  $\Delta \rho / \rho_O$  vs.  $\psi$  for  $Au_2PbVI$ .  $Au_2Pb\overline{VII}$ 

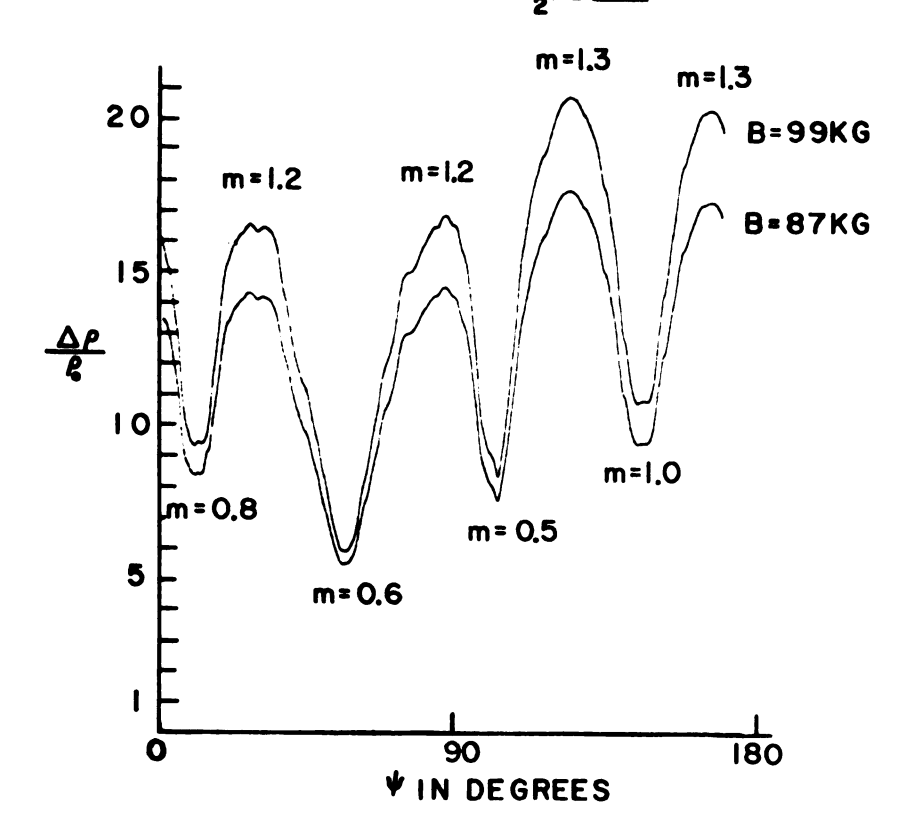


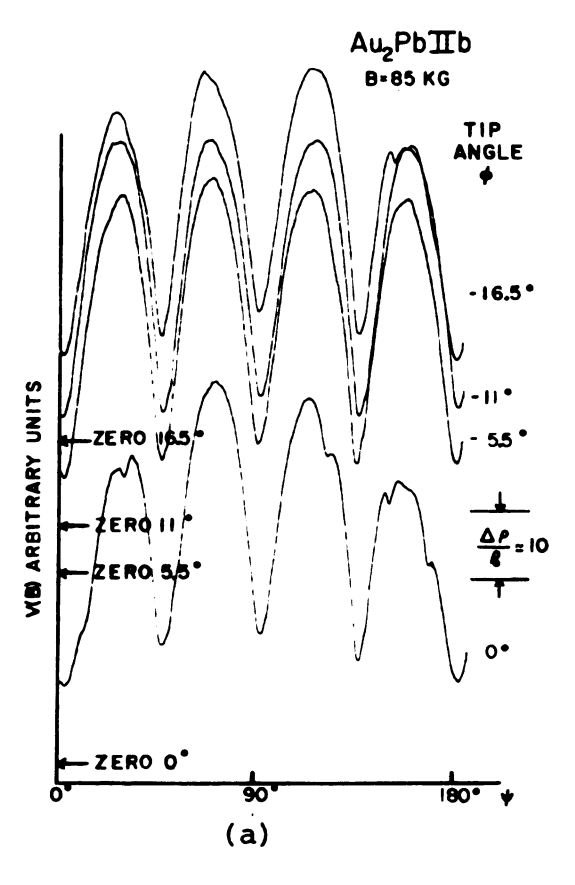
Figure 43.  $\Delta \rho / \rho_0$  vs.  $\psi$  for  $Au_2$ PbVII.

HFMR has values ranging from m  $\approx$  1.5 to m  $\approx$  0. Such an occurrence can only be explained by the presence of open orbits. If the compound is compensated, the field dependence of the HFMR should approach 2 and m will  $\approx$  0 only if there are open orbits present. On the other hand, if  $\mathrm{Au_2Pb}$  is uncompensated, m should saturate for a general field direction and approach the value 2 when B is in a direction producing open orbits. Thus, whatever the state of compensation,  $\mathrm{Au_2Pb}$  has a FS which supports open orbits.

In order to determine the directions of the open orbits, the crystals were tipped through various angles  $\phi$  and the positions of the minima plotted on a stereographic projection. Figures 44 to 46 show the data for the Au<sub>2</sub>PbIIb sample and Figure 47 shows some data for Au<sub>2</sub>PbIb and Au<sub>2</sub>PbIII while Figures 48 and 49 show the stereographic projections.

The symbols used in the stereographic projections are similar to those used for the AuPb<sub>2</sub> samples. The X's designate mate minima, designates an open orbit direction, and the planes which connect the minima are drawn with dash lines. The principle directions and planes are drawn with solid lines and are taken from the Laue x-ray photographs. There was no way of aligning the Laue photographs with some characteristic minima as was done for the AuPb<sub>2</sub> samples.

Looking at the stereographic projections, it is evident that the minima lie on planes but the planes do not correspond to the major crystallographic planes, {100}, {110},



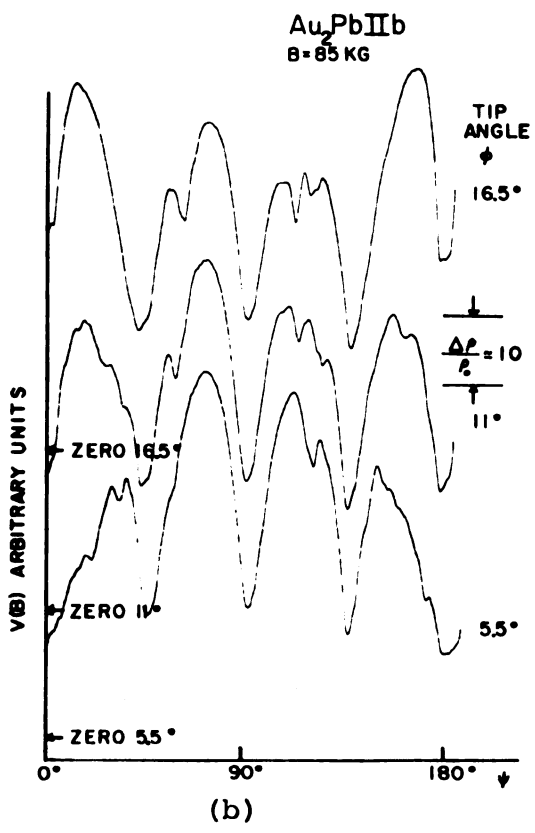
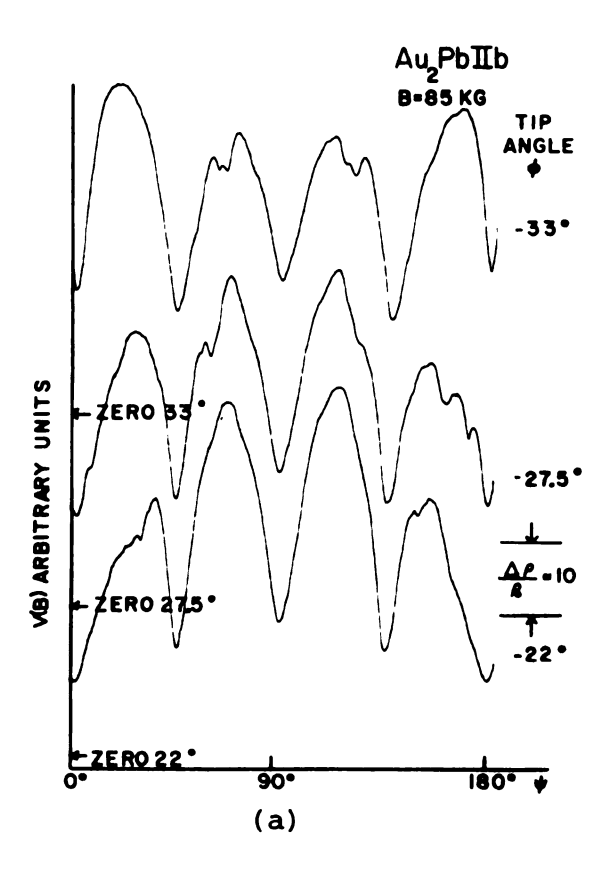


Figure 44. V(B) vs.  $\psi$  for tip angles  $\phi \le |16.5^{\circ}|$ .



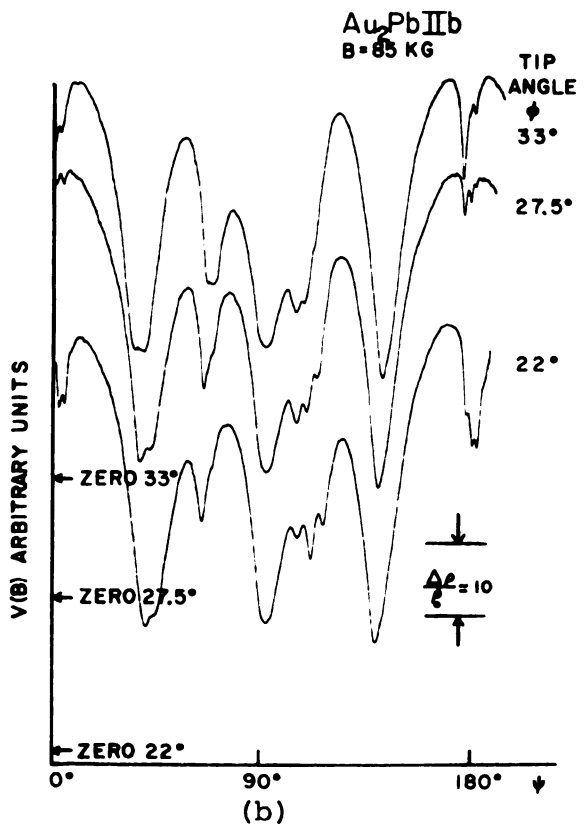
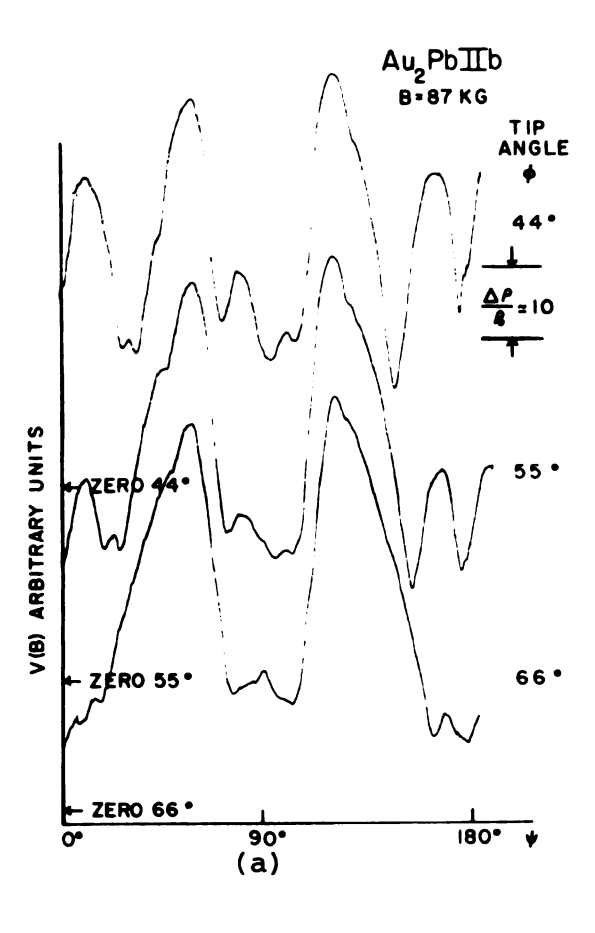


Figure 45. V(B) vs.  $\psi$  for tip angles  $\phi^{\leq}|33^{\circ}|$ .



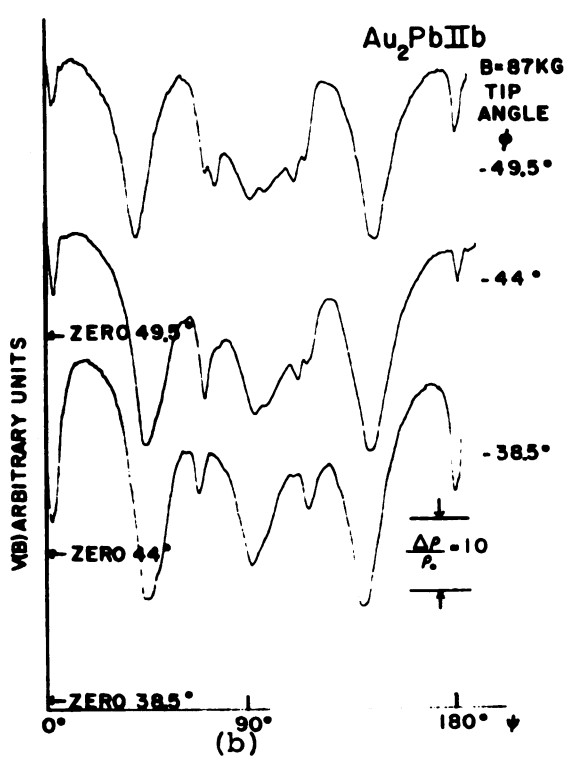


Figure 46. V(B) vs.  $\psi$  for tip angles  $\phi \le |66^{\circ}|$ .

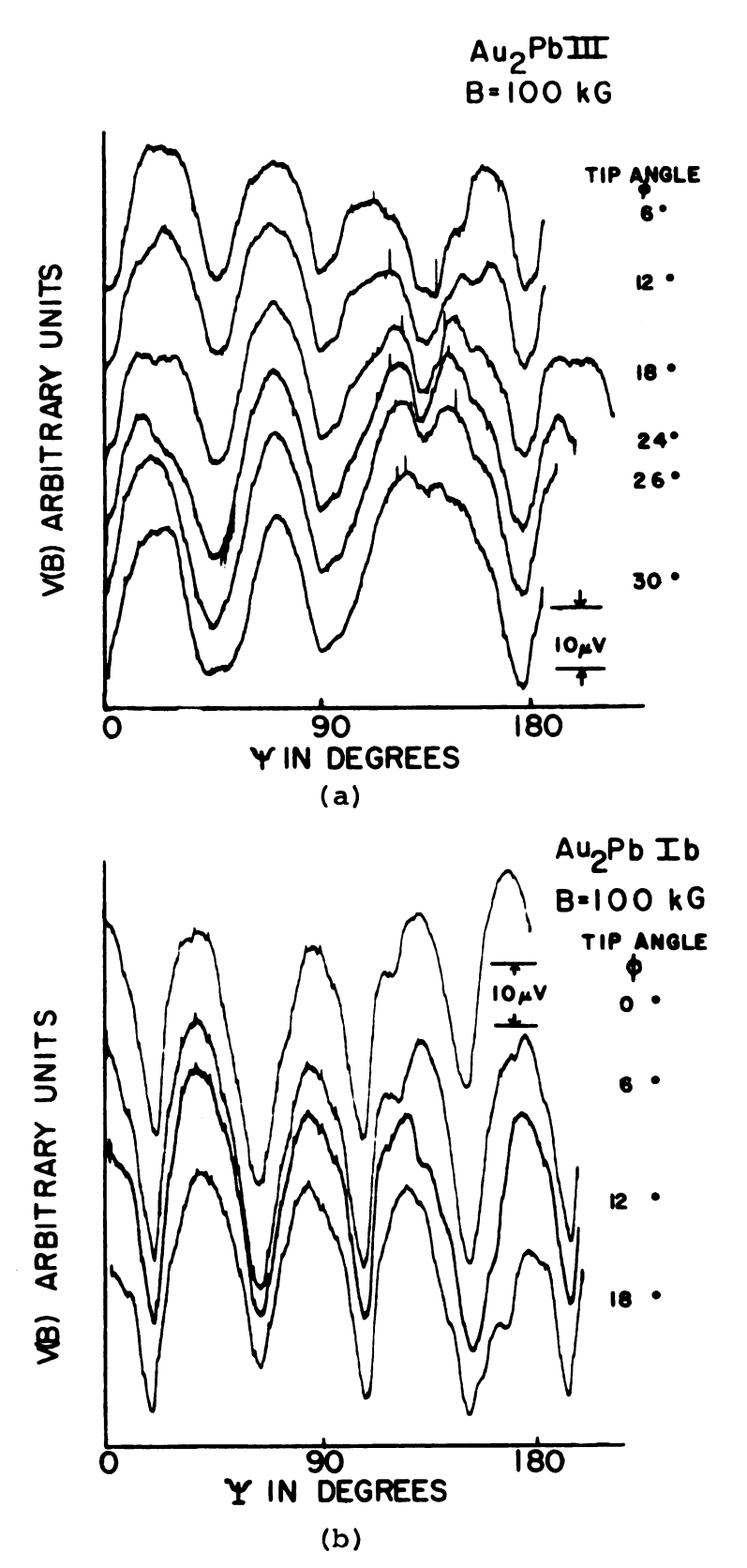
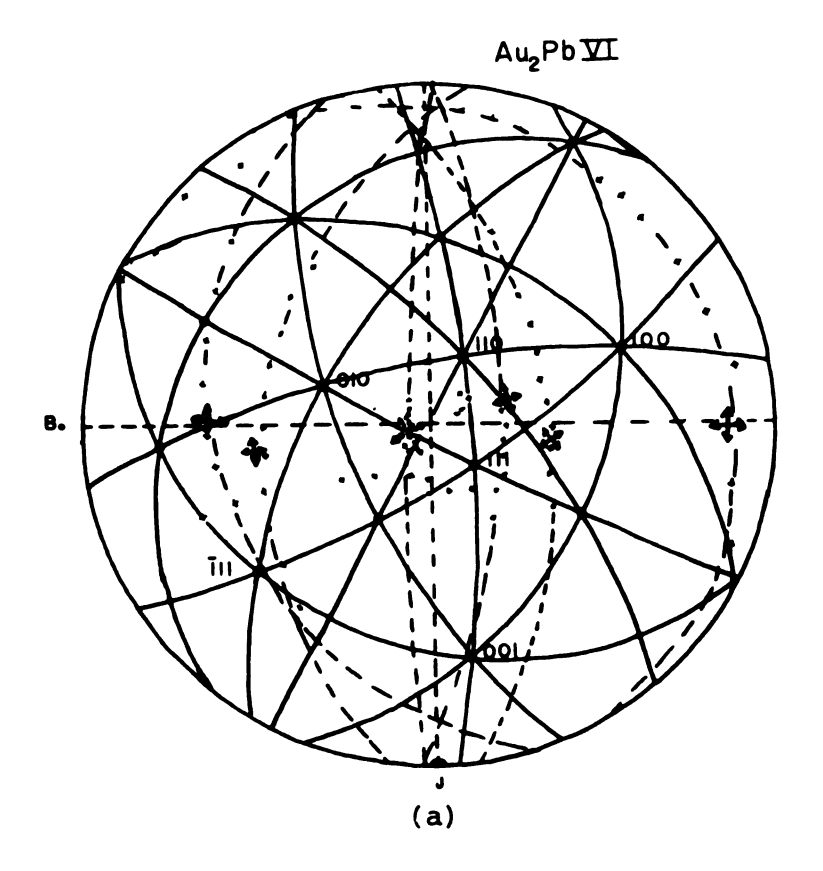


Figure 47. V(B) vs.  $\psi$  for various values of  $\phi$  for (a) Au<sub>2</sub>PbIII and (b) Au<sub>2</sub>PbIb.



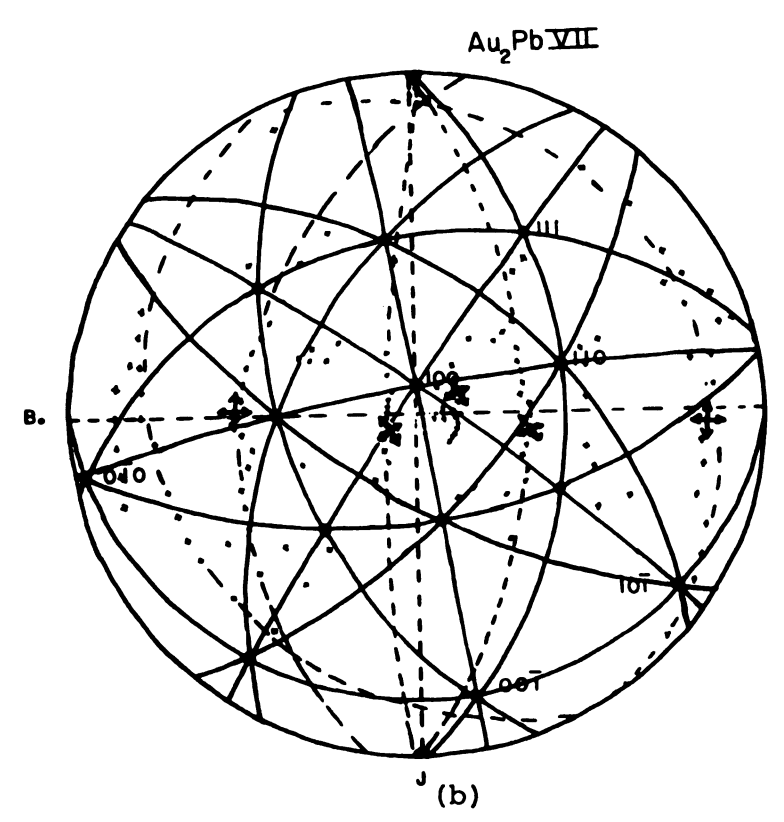


Figure 49. Stereographic projections of HFMR results for (a) Au<sub>2</sub>PbVI and (b) Au<sub>2</sub>PbVII.

<111>, and <112>. Thus the open orbit directions do not lie along the symmetry axes in the crystal as would be expected.
Faced with such a development, the positions of the maxima were plotted since if the compound was uncompensated the open orbits would be manifested by maxima rather than minima. Two such attempts, for Au<sub>2</sub>PbIIb and Au<sub>2</sub>PbVII gave worse results than plotting the minima.

The data obtained by tipping the crystal is thus hard to understand. However, the sharpness of the dips observed in the Au<sub>2</sub>PbIIb sample strongly indicates that Au<sub>2</sub>Pb is a compensated compound. Sharp dips can only be observed in an uncompensated compound when B is in a singular field direction. Such directions are the <100>, <111>, and possibly <110> for a cubic structure. The sharp dips are observed in directions other than those just given and Au<sub>2</sub>Pb must be compensated.

The stereographic projections do show some consistent patterns. The direction of the open orbit lies on a plane which is formed by minima associated with another open orbit. Most of the open orbit directions lie close to 90° from the current direction but their directions seem to be random although Au<sub>2</sub>PbIIb seems to have an open orbit in the <111> and <100>.

One systematic trend not shown on the stereographic projections can be seen from the raw data. Figure 47a which shows the MR signal for  $Au_2PbIII$  at various  $\phi$ , shows the disappearance of a minima as the tip angle increases. Figure 45b and Figure 46b also show minima which get rather shallow

compared to the minima at tip angles on either side. Such behavior, one or more deep minima which gets very shallow for certain tip angles but is relatively deep for other tip angles, has been observed for all of the crystals which have been studied by the tip method (Au<sub>2</sub>PbV was not studied) except for Au<sub>2</sub>PbII - not to be confused with Au<sub>2</sub>PbIIb which is a different sample. However, the position of this shallow dip varies from sample to sample.

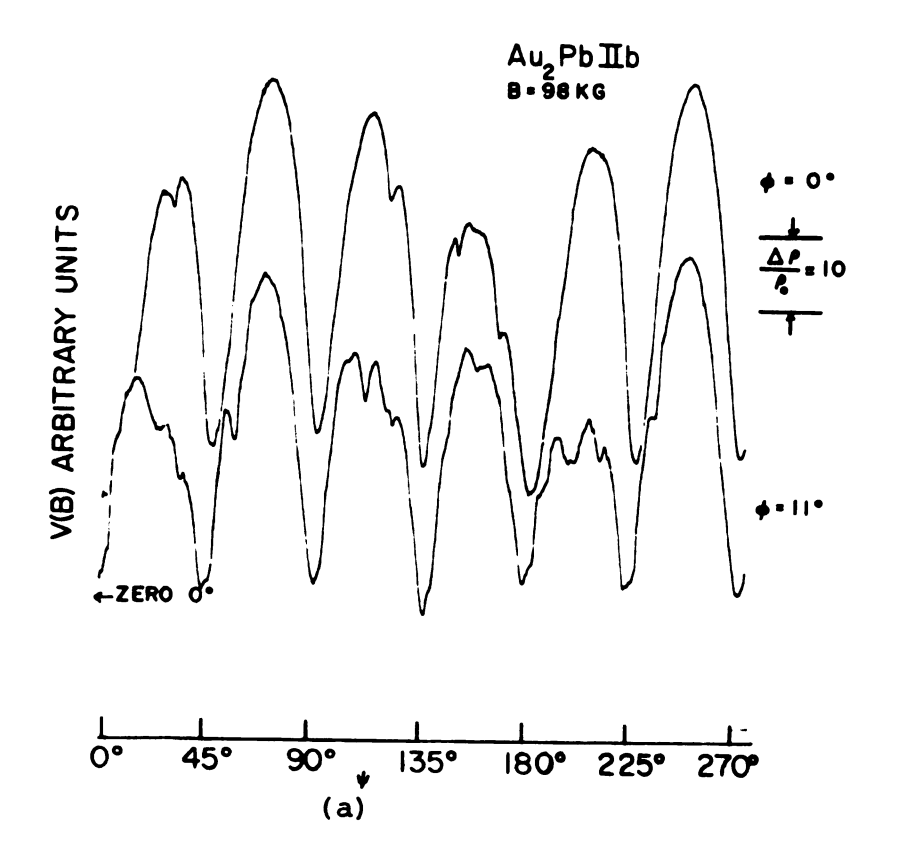
There are some very puzzling anomalies aside from the open orbit directions. The HFMR of Au<sub>2</sub>PbII is shown in Figure 38 for  $\phi$  = 0. This sample was also measured for various other angles of  $\phi$ , although the data is not shown. data for all tip angles was lacking in the characteristic four minima pattern of the other samples. This crystal, Au, PbII, and Au, PbIIb were cut from the same sample. The initial sample was approximately 1/8" in diameter and 4" in length. Both samples were cut with the current axis approximately parallel to the sample axis. The difference between the current directions of the two samples should not be more than 5°. However, the HFMR is drastically different. A small difference in current directions can produce results which differ markedly (Sn<sup>(45)</sup> is an example), yet it is difficult to understand why this type of behavior occurs in Au,Pb.

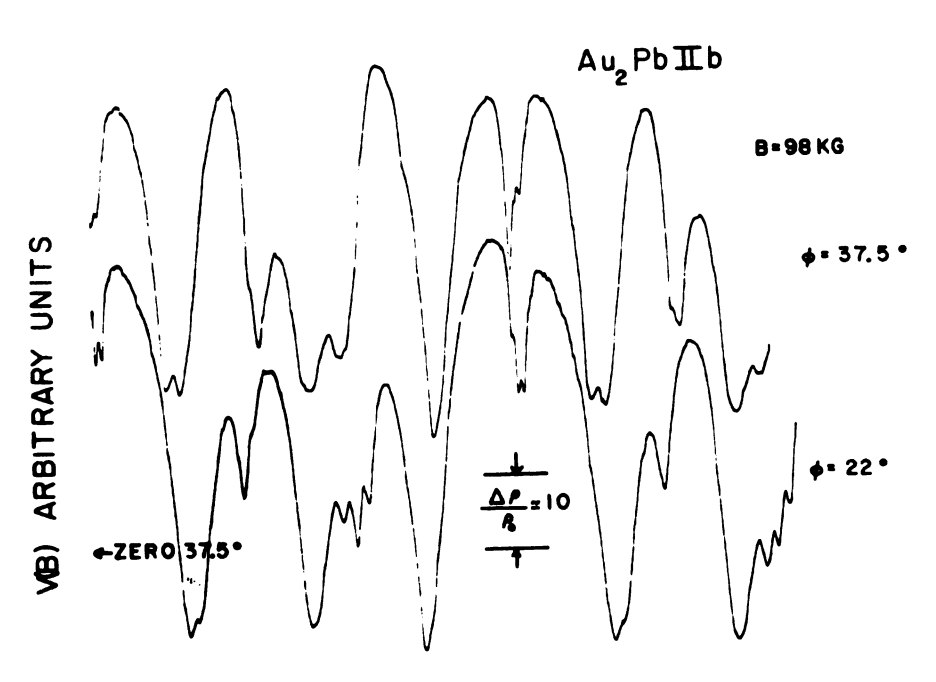
Another sample showing anomalous behavior is  $Au_2PbV$ . Figure 4lb shows the HFMR for  $\phi=0$ . This data also shows little anisotropy. The RRR of  $Au_2PbV$  is not much different

from that of  $\mathrm{Au_2PbIII}$ , yet  $\mathrm{Au_2PbIII}$  shows characteristics of the other samples. No data was taken for  $\mathrm{Au_2PbV}$  at other values of  $\phi$ .

In order to check that the sample holder was operating properly and that the voltage probes were aligned properly, rotation plots were taken with  $\psi$  going from 0 to ~270°. Such plots were taken on all three compounds studied. The data for the AuGa and AuPb<sub>2</sub> (not shown) samples had the following characteristics. The dips were observed to be separated by 180°  $\pm$  2° as is expected. The magnitude of the signal sometimes was observed to vary by about 10% for two positions separated by 180°. This behavior indicates that the sample holder rotates about its AA' axis (see Figure 9)  $\bot$  B. The difference in magnitude of the voltage signal is probably due to a slight difference in the magnitude of the field at the two positions or to probe misalignment.

For the Au<sub>2</sub>PbIIb sample, Figures 50a and 50b show features which are unique. For  $\phi = 0$ , the small dip seen in the first maximum is not repeated when  $\psi$  is 180° away. For  $\phi = 11^\circ$ , the entire appearance of the first peak is quite different from its appearance 180° away. For  $\phi = 37.5^\circ$ , the dips and peaks are periodic in 180°. For  $\phi = 22^\circ$ , the first dip is fairly well reproduced 180° away, while the three dips at  $\psi = 115^\circ$  are slightly distorted at  $\psi = 290^\circ$ . The data for the sample indicates that Au<sub>2</sub>Pb is extraordinarily sensitive to the position of B, more so than either the AuGa or AuPb<sub>2</sub> samples.





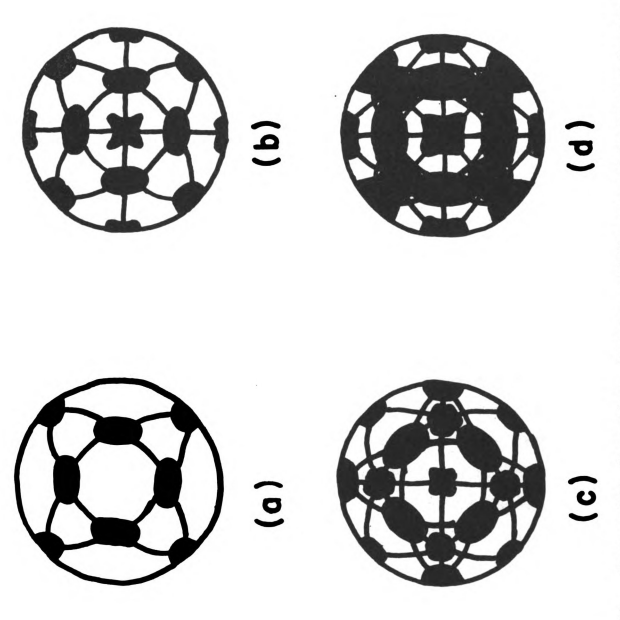
O° 45° 90° 135° 180° 225° 270°  $\psi$  (b) Figure 50. V(B) vs.  $\psi$  for Au<sub>2</sub>PbIIb for (a)  $\phi$  = 0°, 11° and (b)  $\phi$  = 22°, 37.5°.

The cause of such anomalous behavior can only be of a speculative nature at this time. The validation of the following explanation requires additional data on samples with current directions of high symmetry.

1. In Figures 51a to 51d, the stereograms showing open orbit directions for four different cubic FS topologies are given. The darkened regions are field directions giving rise to aperiodic open orbits and the planes connecting these regions are field directions which produce periodic open orbits. The undarkened areas are thus regions which support no open orbits, the so-called general field directions. These diagrams are taken from the paper by Lifshitz and Peschanski . Although J. T. Longo (46) has pointed out that the analyses underlying these diagrams is not of general validity, the diagrams do illustrate points which are of general validity and these points are the ones which will be discussed.

First, open orbits are produced when B lies in a high symmetry plane or when B is near a high symmetry axis. However, if the diameter of the cylinders which serve as the model for calculating the open orbit directions is varied, the area of the darkened regions will vary. Figure 5ld shows a diagram where almost 3/4 of the field directions produce open orbits. By varying the diameters of the cylinders, the other diagrams could also be made to have greater open orbit producing regions.

Now, in a compensated material  $\Delta \rho/\rho_{_{\rm O}}$  ~  $B^2$   $\cos^2\alpha$  where  $\alpha$ 



Open orbit directions for four different cubic FS topologies. (From Lifshitz and Peschanski, Ref. 40). Figure 51.

is the angle between the open orbit direction in k-space and the current direction. In a region where there are aperiodic open orbits, the direction of the open orbit is determined by the line of intersection of the plane  $\bot$  B with the plane perpendicular to the symmetry direction about which the aperiodic region is formed. Since  $\alpha$  will not in general be equal to 90°, the open orbit may be difficult to pick out in a compensated compound since both open and closed orbits will have a B<sup>2</sup> dependence. As the regions supporting open orbits increase, as in Figure 51d, the difficulty of identifying two dimensional open orbit areas increases.

It is not generally difficult to identify periodic open orbit directions, the lines or planes in Figure 50, but as the two dimensional regions increase in area, the one dimensional regions decrease and extend over a smaller angular region. If there are no aperiodic open orbit regions, the periodic open orbits will generally exist for the entire 180° angular region. However, when aperiodic open orbits exist, the angular region for periodic open orbits which connect two aperiodic regions can be as small as 10° as in Figure 50d. Thus even periodic open orbits can be difficult to identify when the extent of the aperiodic open orbit region is large.

Thus, a possible explanation of the data on Au<sub>2</sub>Pb is that the FS of Au<sub>2</sub>Pb is such that there are very large areas of aperiodic open orbits formed which make the identification of the open orbit directions difficult.

2. A second possibility is the charge wave theory of

Overhauser which was proposed to explain anomalies in the HFMR of potassium.  $^{(48)}$  This theory has evoked mixed reactions and it is still on relatively uncertain ground. Briefly, the theory assumes that a charge density wave of wave vector  $\bar{\mathbb{Q}}$ ,  $(|\mathbb{Q}| > 2k_f)$  exists and that  $\bar{\mathbb{Q}}$  can be oriented by an external magnetic field. Since  $|\mathbb{Q}| > 2k_f$ , the charge density periodicity does not change the connectivity of the FS. However, additional energy gaps appear due to beat or heterodyne periods arising from the interaction of the charge-density and lattice periods. These additional energy gaps are produced primarily at k vectors which satisfy the equation

$$\vec{K} = 2\pi \vec{G}_{hkl} \pm \vec{Q}$$

where  $\overline{G}_{hkl}$  is a reciprocal lattice vector. Since these additional energy gaps depend on the orientation of  $\overline{Q}$ , which in turn depends on the external magnetic field direction, the trajectories which the electrons follow will not only depend on the FS but will also depend on the orientation of the magnetic field.

The charge density wave theory could thus explain the non-symmetry direction for the open orbits as well as the fact that no two experimentally determined open orbit directions coincided with each other.

3. Magnetic breakdown (MB) can produce many strange effects. Electrons undergoing closed orbits can form open trajectories because of MB and vice versa. The quantity which is usually most affected by MB is the field dependence of the HFMR. No dramatic changes of field dependence have

been observed, but magnetic breakdown manifests itself in so many subtle ways that it cannot be ruled out as a contributing factor to the present problems. The prediction of what effects MB may produce when the Fermi surface is unknown is extremely difficult.

4. It is possible that the HFMR depends drastically on the composition of the samples. Since Au<sub>2</sub>Pb is a peritectic alloy, the composition of the initial samples varied over a region of ~10 at.%. Also, as the crystals were being grown, concentration gradients were undoubtedly produced along the length of the samples. Thus, if the width of the line at composition Au<sub>2</sub>Pb in the phase diagram is of finite size, say 1 or 2 at.%, and varies with temperature, the concentrations of the various samples used could have been different. Now, one must show how this difference in composition can alter the HFMR.

One possible effect is the following. Suppose that the FS of Au<sub>2</sub>Pb just misses making contact with a Brillouin zone face. If, by altering the composition of the compound, more electrons per atom can be introduced, as would happen if Pb atoms replaced some Au atoms, then the FS could be made to touch the zone face and thus produce open orbits. Thus, the FS would be either open or closed depending on the concentration of the samples. However, such an argument does not explain the non-symmetry directions for the open orbits since the Brillouin zone faces are perpendicular to symmetry axes and thus the open orbit directions should be in symmetry

All lander receive and the land

directions.

5. There is a finite possibility that the crystal structure of Au<sub>2</sub>Pb is not cubic at 4.2°K. A martensitic transformation could occur at low temperature and the resulting crystal structure could be a non-cubic structure. The HFMR data depends on the geometry of the lattice and thus the data would not show cubic symmetry.

There are two facts which seem to indicate that a martensitic transformation does not occur. First, the Au<sub>2</sub>Pb samples have a relatively high RRR indicative of high crystalline perfection. A phase change would probably produce polycrystals and grain boundaries in the sample and these imperfections would lower the RRR appreciably.

Secondly, since the Laue photographs are identical after recycling between room and liquid He temperature, the phase change would also have to produce crystals which have the same orientation as the initial samples. Such occurrences seem unlikely.

6. There is a possibility that the data is an artifact of the measurement procedure. Since the solder used to attach the voltage leads does alloy with the sample, the HFMR data may be an indication of probe effects. The possibility cannot be entirely ruled out, but the similarities in the data for different samples would seem to make it an unlikely explanation.

To summarize, Au<sub>2</sub>Pb is a compensated compound and its FS supports open orbits. The direction of the open orbit do not

The state of the s

seem to run in symmetry directions which is at variance from the expected behavior. There are some consistencies in the data but there are also anomalies. Some possible explanations have been proposed and evaluated, but the verification of these ideas requires more experimental work.

### VII. CONCLUSIONS

The FS topology of three compounds, AuGa, AuPb<sub>2</sub> and Au<sub>2</sub>Pb, has been studied by HFMR. Each compound represents a crystal structure which has previously not been investigated by HFMR. Since most intermetallic compounds have an even number of atoms per unit cell, the compounds will most likely be compensated. The three compounds studied in this research were found to be compensated and the experimental procedures and techniques used in this research should serve as a guide to further study of compensated compounds.

The FS topology of AuGa cannot be explained by a NFE model assuming Au contributes 1 electron/atom and Ga 3 electrons/atom. There are open orbits in the [001] but no open orbits in the [100], even though the lattice constant differs by only 2% for the two directions. The NFE model gives open orbits in both directions which is at variance with the experimentally determined directions. A double zone scheme was also tried but again the NFE model did not give results consistent with the experimental findings.

The FS of AuGa is thus not NFE-like. It is possible that the FS touches the Brillouin zone face in the [001] but not in the [100]. The necks in the [001] direction could produce the open orbits observed while their absence in the [100] would explain the fact that there are no open orbits in the

[100]. The distortion of the FS from the NFE sphere would be similar to the <111> neck distortion observed in the noble metals Au, Ag, and Cu. Another explanation for the non-NFE like behavior is that there is chemical binding effects not taken into account by the NFE model.

The FS topology of AuPb<sub>2</sub> has been investigated in some depth with the [001] being the only major crystallographic direction not able to be tested for open orbits. Open orbits were found in the <100>, <110>, <101>, <112>, and <211> in k-space as well as some other higher order directions.

A model of the AuPb<sub>2</sub> open FS is proposed which consists of cylinders running in the <110> and <101> in k-space. This model seems capable of explaining all the major open orbit directions. The Harrison construction was performed for a few magnetic field directions; 18 electrons per unit cell were assumed. The results of the construction are in agreement with the experimentally observed <110> and <101> open orbits. Thus the FS of AuPb<sub>2</sub> may be explained in terms of the NFE model, however, more work is needed before the NFE model can be verified.

The Au<sub>2</sub>Pb results are difficult to interpret. The open orbit directions appear to be along non-symmetry directions which is different from the expected behavior. Possible explanations for these peculiar results are proposed.

The high degree of crystalline perfection attained in the  ${\rm Au_2Pb}$  and  ${\rm AuPb_2}$  samples makes them attractive candidates for study by the dHvA method. The results of the dHvA

measurements would determine whether  $\mathrm{AuPb}_2$  is NFE like. Also, these measurements could clear up the anomalous behavior observed in  $\mathrm{Au}_2\mathrm{Pb}$ .

LIST OF REFERENCES

#### LIST OF REFERENCES

- 1. A. C. Thorsen and T. G. Berlincourt, Nature, London 192, 959 (1961).
- J.-P. Jan, W. B. Pearson, and M. Springford, Can. J. Phys. 42, 2357 (1964).
- 3. D. J. Sellmyer, J. Ahn, and J.-P. Jan, Phys. Rev. <u>161</u>, 618 (1967).
- J.-P. Jan, W. B. Pearson, and Y. Saito, Proc. Roy. Soc. A297, 275 (1967).
- 5. J.-P. Jan, W. B. Pearson, Y. Saito, M. Srpingford, and I. M. Templeton, Phil. Magn. 12, 1271 (1965).
- J. T. Longo, P. A. Schroeder, and D. J. Sellmyer, Phys. Rev. 182, 658 (1969).
- 7. J. Ahn and D. J. Sellmyer, Phys. Rev. B 1, 1273 (1970).
- 8. S. M. Marcus and D. C. Donohue, Phys. Rev. <u>183</u>, 668 (1969).
- 9. D. L. Wagner, Ph.D. thesis, Case Western Reserve University (1970), unpublished.
- 10. B. W. Neal and J. A. Rayne, Phys. Letters 6, 12 (1963).
- W. N. Cathey, P. T. Coleridge, and J.-P. Jan, Can. J. Phys. <u>48</u> 1151 (1970).
- 12. G. J. Edwards, M. Springford, and Y. Saito, J. Phys. Chem. Solids, 30, 2527 (1969).
- 13. D. J. Sellmyer, J. Phys. Chem. Solids, 30, 2371 (1969).
- 14. J.-P. Jan, W. B. Pearson, and M. Springford, Can. J. Phys. 42, 2357 (1964).
- 15. J.-P. Jan, C. M. Perrott, Roger Taylor, J. Low Temp. Phys. 3, 639 (1971).
- 16. W. A. Harrison, "Pseudopotential in the Theory of Metals", W. A. Benjamin, New York, 1966.
- 17. K. H. Johnson and H. Amar, Phys. Rev. 139, A760 (1965).

- F. J. Arlinghaus, Phys. Rev. 186, 609 (1969).
- 19. R. Taylor, Proc. Roy. Soc. A321, 495 (1969).
- 20. S. J. Cho, Phys. Status Solidi 41, 179 (1971).
- 21. K. H. Johnson and J. W. D. Connally, Inter. J. of Quantum Chem. IIIS, 813 (1970).
- 22. A. C. Switendick and A. Narath, Phys. Rev. Letters <u>22</u>, 1423 (1969).
- 23. Work in Progress, reported by D. J. Sellmyer.
- 24. P. Rennert and M. Taut, Phys. Status Solidi 41, 703 (1970).
- 25. L. F. Mattheiss, Phys. Rev. 138, Al12 (1965).
- 26. J. H. Westbrook, ed. "Intermetallic Compounds", John Wiley & Sons, New York, p. 166 (1967).
- 27. W. B. Pearson and A. Kjekshus, Prog. in Solid State Chem. 1, 83, (1964).
- 28. P. A. Beck, ed. "Electronic Structure and Alloy Chemistrof the Transition Elements", Wiley, New York, (1963).
- 29. L. F. Westbrook, op. cit., p. 581.
- 30. D. J. Sellmyer, Ph.D. thesis, Michigan State University (1965), unpublished.
- 31. M. Hansen, ed. "Constitution of Binary Alloys", McGraw-Hill, New York (1958).
- 32. Present work.
- 33. J. H. Westbrook, op. cit., p. 332.
- 34. J.-P. Jan, W. B. Pearson, Can. J. Phys. 42, 220 (1964).
- 35. E. Justi and H. Scheffers, Metallwirtschaft 17, 1359 (1938).
- 36. M. Kohler, Ann. Physik 5, 99 (1949).
- 37. R. G. Chambers, Proc. Roy. Soc., A238, 344 (1956).
- 38. I. M. Lifshitz, M. I. Azbel and M. I. Kaganow, J.E.T.P. 4, 41 (1957).
- 39. I. M. Lifshitz and V. G. Peschanski, J.E.T.P. <u>8</u>, 875 (1959).

- 40. I. M. Lifshitz and V. G. Peschanski, J.E.T.P. <u>11</u>, 137 (1960).
- 41. E. Fawcett, Advances in Phys., 13, 50 (1964).
- 42. W. A. Harrison, "Solid State Theory", McGraw-Hill, New York, p. 252 (1970).
- 43. J. C. Abele, Ph.D. thesis, Michigan State University (1968), unpublished.
- 44. D. J. Sellmyer, Rev. Sci. Inst., 38, 434 (1967).
- 45. N. E. Alekseevskii, Yu. P. Gaidukov, I. M. Lifshitz, and V. G. Peschanski, J.E.T.P. 12, 837 (1960).
- 46. J. T. Longo, Ph.D. thesis, Michigan State University (1968), unpublished.
- 47. L. M. Falicov and M. H. Cohen, Phys. Rev. Letters 5, 544 (1960).
- 48. A. W. Overhauser and John R. Reitz, Phys. Rev. <u>171</u>, 749 (1968).

PRESENT OF STREET LEADING AND LEADING TO STREET STREET

**APPENDICES** 

## APPENDIX A

## The Relaxation Approximation

In the relaxation approximation the collision term is given by

$$(\frac{\partial f}{\partial t})$$
 | Coll =  $-\frac{(f-f_0)}{\tau(\epsilon)}$ 

where  $\tau(\epsilon)$  is the relaxation time which can depend on the energy and on the wavevector k.

In using this approximation it is assumed that if the distribution function f differs from the equilibrium Fermi function  $f_0$ , then it will decay exponentially in time to  $f_0$ .

The Boltzman equation can then be solved for  $\bar{\psi}$  and the solution is given by

$$\overline{\psi}(\mu) = \alpha e^{-\alpha \mu} \int_{-\infty}^{\mu} e^{\alpha \mu'} \overline{v}(\mu') d\mu'$$

where

$$\alpha = \frac{1}{|\mathbf{e}| \mathbf{B} \tau} = \frac{1}{\omega_{\mathbf{c}}^{\tau \mathbf{m}} \mathbf{H}}$$

The conductivity tensor becomes

$$\sigma_{ij} = \frac{1}{4\pi^3} \frac{e^2}{6^2} \int \frac{m_H}{\omega_C} \{ \int_{0}^{2\pi} \int_{0}^{\infty} v_i(\mu, k_z) v_j(\mu - \mu') e^{-\mu' \tau/\omega_C} d\mu d\mu' \} dk_z$$

which is the Shockley tube integral. This integral is applicable in both high and low fields. In high fields where

 $\omega_{\mathbf{C}^{\mathsf{T}}}$  >> 1 and the periodicity of the electron orbits allows for simplication, the coefficients of the conductivity tensor can be calculated if the velocity of the electrons in k-space as well as the variation of the relaxation  $\tau(\varepsilon)$  is known at each point on the electron orbits.

#### APPENDIX B

# The Superconducting Magnet

A RCA Type SM2830 superconducting magnet which is capable of reaching 103 kG was used to produce the magnetic field. The magnet is made from Nb<sub>3</sub>Sn superconducting ribbons and the magnet has a usable bore of slightly greater than 1.5". The magnet could be swept at a rate of 2A/min up to 72A and then at a rate of 1A/min up to 89A, the maximum current rating.

The magnetic field was measured by a magneto-resistive coil which is permanently wound on the bore in the center of the magnet. The magnetoresistor was calibrated by Dr. G. J. Edwards and Dr. P. A. Schroeder using NMR measurements on H<sup>1</sup>, F<sup>19</sup> and Al<sup>27</sup>. DHvA measurements on potassium provided field profiles. The position of the maximum magnetic field was found to be within 0.1" from the geometric center of the magnet at 98 kG.

All measurements indicate that the field at the center of the magnet is axial. The symmetry of the field in the radial direction was also checked by C. K. Chiang and found to be symmetric to within experimental error. As a final check, the HFMR cryostat was rotated by 120°, and 240°, about the axis of the magnet. The HFMR of the AuPb<sub>2</sub>I sample was

taken with  $\psi$  varying from 0° to 200° for all three directions. The three plots were identical, showing sharp dips at exactly the same value of  $\psi$ . Thus the magnetic field has very little asymmetry at the center of the magnet.

